

Jordan Journal of Mechanical and Industrial Engineering (JJMIE)

JJMIE is a high-quality scientific journal devoted to fields of Mechanical and Industrial Engineering. It is published by Hashemite University in cooperation with the Jordanian Scientific Research and Innovation Support Fund, Ministry of Higher Education and Scientific Research.

EDITORIAL BOARD

Editor-in-Chief

Prof. Moh'd Sami Ashhab

Assistant Editors

Dr. Ahmad AlMigdady

Dr. Mohammad Jreissat

Editorial Board

Prof. Tariq A. ALAzab

Al Balqa Applied University

Prof. Jamal Jaber

Al- Balqa Applied University

Prof. Mohamad Al-Widyan

Jordan University of Science and Technology

Prof. Mohammed Taiseer Hayajneh

Jordan University of Science and Technology

Prof. Mohammad Al-Tahat

The University of Jordan

Prof. Ali M. Jawarneh

The Hashemite University

THE INTERNATIONAL ADVISORY BOARD

Abu-Qudais, Mohammad

Jordan University of Science & Technology, Jordan

Tzou, Gow-Yi

Yung-Ta Institute of Technology and Commerce, Taiwan

Abu-Mulaweh, Hosni

Purdue University at Fort Wayne, USA

Jubran, Bassam

Ryerson University, Canada

Afaneh Abdul-Hafiz

Robert Bosch Corporation, USA

Kakac, Sadik

University of Miami, USA

Afonso, Maria Dina

Institute Superior Tecnico, Portugal

Khalil, Essam-Eddin

Cairo University, Egypt

Badiru, Adedji B.

The University of Tennessee, USA

Mutoh, Yoshiharu

Nagaoka University of Technology, Japan

Bejan, Adrian

Duke University, USA

Pant, Durbin

Iowa State University, USA

Chalhoub, Nabil G.

Wayne State University, USA

Riffat, Saffa

The University of Nottingham, U. K

Cho, Kyu-Kab

Pusan National University, South Korea

Saghir, Ziad

Ryerson University, Canada

Dincer, Ibrahim

University of Ontario Institute of Technology,
Canada

Sarkar, MD. Abdur Rashid

Bangladesh University of Engineering &
Technology, Bangladesh

Douglas, Roy

Queen's University, U. K

Siginer, Dennis

Wichita State University, USA

El Bassam, Nasir

International Research Center for Renewable
Energy, Germany

Sopian, Kamaruzzaman

University Kebangsaan Malaysia, Malaysia

Haik, Yousef

United Arab Emirates University, UAE

EDITORIAL BOARD SUPPORT TEAM

Language Editor

Dr. Baker M. Bani-khair

Publishing Layout

Eng. Ali Abu Salimeh

SUBMISSION ADDRESS:

Prof. Moh'd Sami Ashhab, Editor-in-Chief
Jordan Journal of Mechanical & Industrial Engineering,
Hashemite University,
PO Box 330127, Zarqa, 13133, Jordan
E-mail: jjmie@hu.edu.jo



Hashemite Kingdom of Jordan



Hashemite University

Jordan Journal of
Mechanical and Industrial Engineering

JJMIIE

An International Peer-Reviewed Scientific Journal
Financed by Scientific Research Support Fund

Volume 14, Number 4, December 2020

<http://jjmie.hu.edu.jo/>

ISSN 1995-6665

Jordan Journal of Mechanical and Industrial Engineering (JJMIE)

JJMIE is a high-quality scientific journal devoted to fields of Mechanical and Industrial Engineering. It is published by Hashemite University in cooperation with the Jordanian Scientific Research and Innovation Support Fund, Ministry of Higher Education and Scientific Research.

Introduction: The Editorial Board is very committed to build the Journal as one of the leading international journals in mechanical and industrial engineering sciences in the next few years. With the support of the Ministry of Higher Education and Scientific Research and Jordanian Universities, it is expected that a heavy resource to be channeled into the Journal to establish its international reputation. The Journal's reputation will be enhanced from arrangements with several organizers of international conferences in publishing selected best papers of the conference proceedings.

Aims and Scope: *Jordan Journal of Mechanical and Industrial Engineering* (JJMIE) is a refereed international journal to be of interest and use to all those concerned with research in various fields of, or closely related to, mechanical and industrial engineering disciplines. *Jordan Journal of Mechanical and Industrial Engineering* aims to provide a highly readable and valuable addition to the literature which will serve as an indispensable reference tool for years to come. The coverage of the journal includes all new theoretical and experimental findings in the fields of mechanical and industrial engineering or any closely related fields (Materials, Manufacturing, Management, Design, Thermal, Fluid, Energy, Control, Mechatronics, and Biomedical). The journal also encourages the submission of critical review articles covering advances in recent research of such fields as well as technical notes.

Guide for Authors

Manuscript Submission:

High-quality submissions to this new journal are welcome now and manuscripts may be either submitted online or email.

Online: For online and email submission upload one copy of the full paper including graphics and all figures at the online, submission site, accessed via <http://jjmie.hu.edu.jo>. The manuscript must be written in MS Word Format. All correspondence including notification of the Editor's decision and requests for revision, takes place by e-mail and via the Author's homepage, removing the need for a hard-copy paper trail

Submission address and contact :

Prof. Moh'd Sami Ashhab

Editor-in-Chief

Jordan Journal of Mechanical & Industrial

Engineering, Hashemite University

PO Box 330127, Zarqa, 13115, Jordan

E-mail: jjmie@hu.edu.jo

Types of contributions: Original research papers and Technical reports

Corresponding author: Clearly indicate who is responsible for correspondence at all stages of refereeing and publication, including post-publication. Ensure that telephone and fax numbers (with country and area code) are provided in addition to the e-mail address and the complete postal address. Full postal addresses must be given for all co-authors.

Original material: Submission of an article implies that the work described has not been published previously (except in the form of itstan abstract or as part of a published lecture or academic thesis), that it is not under consideration for publication elsewhere, the publication is approved by all authors and that, if accepted, it will not be published elsewhere in the same form, in English or in any other language, without the written consent of the Publisher. Authors found to be deliberately contravening the submission guidelines on originality and exclusivity shall not be considered for future publication in this journal.

Withdrawing: If the author chooses to withdraw his article after it has been assessed, he shall reimburse JJMIE with the cost of reviewing the paper.

Manuscript Preparation:

General: Editors reserve the right to adjust style to certain standards of uniformity. Original manuscripts are discarded after publication unless the Publisher is asked to return original material after use. Please use MS Word for the text of your manuscript

Structure: Follow this order when typing manuscripts: Title, Authors, Authors title, Affiliations, Abstract, Keywords, Introduction, Main text, Conclusions, Acknowledgements, Appendix, References, Figure Captions, Figures and then Tables. Please supply figures imported into the text AND also separately as original graphics files. Collate acknowledgements in a separate section at the end of the article and do not include them on the title page, as a footnote to the title or otherwise.

Text Layout: Use 1.5 line spacing and wide (3 cm) margins. Ensure that each new paragraph is clearly indicated. Present tables and figure legends on separate pages at the end of the manuscript. If possible, consult a recent issue of the journal to become familiar with layout and conventions. All footnotes (except for table and corresponding author footnotes) should be identified with superscript Arabic numbers. To conserve space, authors are requested to mark the less important parts of the paper (such as records of experimental results) for printing in smaller type. For long papers (more than 4000 words) sections which could be deleted without destroying either the sense or the continuity of the paper should be indicated as a guide for the editor. Nomenclature should conform to that most frequently used in the scientific field concerned. Number all pages consecutively; use 12 or 10 pt font size and standard fonts.

Corresponding author: Clearly indicate who is responsible for correspondence at all stages of refereeing and publication, including post-publication. The corresponding author should be identified with an asterisk and footnote. Ensure that telephone and fax numbers (with country and area code) are provided in addition to the e-mail address and the complete postal address. Full postal addresses must be given for all co-authors. Please consult a recent journal paper for style if possible.

Abstract: A self-contained abstract outlining in a single paragraph the aims, scope and conclusions of the paper must be supplied.

Keywords: Immediately after the abstract, provide a maximum of six keywords (avoid, for example, 'and', 'of'). Be sparing with abbreviations: only abbreviations firmly established in the field may be eligible.

Symbols: All Greek letters and unusual symbols should be identified by name in the margin, the first time they are used.

Units: Follow internationally accepted rules and conventions: use the international system of units (SI). If other quantities are mentioned, give their equivalent quantities in SI

Maths: Number consecutively any equations that have to be displayed separately from the text (if referred to explicitly in the text).

References: All publications cited in the text should be presented in a list of references following the text of the manuscript.

Text: Indicate references by number(s) in square brackets in line with the text. The actual authors can be referred to, but the reference number(s) must always be given.

List: Number the references (numbers in square brackets) in the list in the order in which they appear in the text.

Examples:

Reference to a journal publication:

[1] M.S. Mohsen, B.A. Akash, "Evaluation of domestic solar water heating system in Jordan using analytic hierarchy process". Energy Conversion & Management, Vol. 38 (1997) No. 9, 1815-1822.

Reference to a book:

[2] Strunk Jr W, White EB. The elements of style. 3rd ed. New York: Macmillan; 1979.

Reference to a conference proceeding:

[3] B. Akash, S. Odeh, S. Nijmeh, "Modeling of solar-assisted double-tube evaporator heat pump system under local climate conditions". 5th Jordanian International Mechanical Engineering Conference, Amman, Jordan, 2004.

Reference to a chapter in an edited book:

[4] Mettam GR, Adams LB. How to prepare an electronic version of your article. In: Jones BS, Smith RZ, editors. Introduction to the electronic age, New York: E-Publishing Inc; 1999, p. 281-304

Free Online Color : If, together with your accepted article, you submit usable color and black/white figures then the journal will ensure that these figures will appear in color on the journal website electronic version.

Tables: Tables should be numbered consecutively and given suitable captions and each table should begin on a new page. No vertical rules should be used. Tables should not unnecessarily duplicate results presented elsewhere in the manuscript (for example, in graphs). Footnotes to tables should be typed below the table and should be referred to by superscript lowercase letters.

Notification: Authors will be notified of the acceptance of their paper by the editor. The Publisher will also send a notification of receipt of the paper in production.

Copyright: All authors must sign the Transfer of Copyright agreement before the article can be published. This transfer agreement enables Jordan Journal of Mechanical and Industrial Engineering to protect the copyrighted material for the authors, but does not relinquish the authors' proprietary rights. The copyright transfer covers the exclusive rights to reproduce and distribute the article, including reprints, photographic reproductions, microfilm or any other reproductions of similar nature and translations.

Proof Reading: One set of page proofs in MS Word format will be sent by e-mail to the corresponding author, to be checked for typesetting/editing. The corrections should be returned within **48 hours**. No changes in, or additions to, the accepted (and subsequently edited) manuscript will be allowed at this stage. Proofreading is solely the author's responsibility. Any queries should be answered in full. Please correct factual errors only, or errors introduced by typesetting. Please note that once your paper has been proofed we publish the identical paper online as in print.

Author Benefits:

No page charges: Publication in this journal is free of charge.

Free offprints: One journal issues of which the article appears will be supplied free of charge to the corresponding author and additional offprint for each co-author. Corresponding authors will be given the choice to buy extra offprints before printing of the article.

PAGES**PAPERS**

- 361 - 370 **MFL Based Prototype and Experimental Work for Detection of Defects in Cables of Bridge Structures**
Emad Abdelsalam, Feras Kafiah, Sanad Kiswani, Dana Ibrahima, Al Ghorbanpoor
- 371 - 379 **A Technical and Economic Study of a Photovoltaic–phase Change Material (PV-PCM) System in Jordan**
Salem Nijmeh, Bashir Hammad, Mohammad Al-Abed, Riad Bani-Khalid
- 381 - 386 **Development of A New Technique for Modeling and Optimizing Manufacturing Errors for Cn Machine Tools**
Messaoud Farouk, Rahou Mohamed, Sebaa Fethi
- 387 - 392 **Thermal Analysis of a Combined Cycle Power Plant under Varying Operating Conditions**
Mustafa Al-Qudah, Ahmad Sakhrieh, Ali Almarzouq, Ahmad Al-Omari
- 393 - 400 **In-situ Hybridization of Waste Palm Oil: A Physicochemical, Thermal, and Spectroscopic Analysis**
Josiah Pelemo, Omojola Awogbemi, Freddie Inambao, Emmanuel I. Onuh
- 401 - 411 **Designing Food Packages to Attract Customers: A Systematic Approach**
Olurotimi Akintunde Dahunsi, Olatunji Oladimeji Ojo, Ikeoluwa Ogedengbe, Omeiza Bayode Maliki
- 413 - 423 **Adaptive Disturbance Estimation and Compensation for Delta Robots**
Iyad Hashlamon
- 425 - 436 **Design of a Screw Conveyor for Transporting and Cooling Plantain Flour in a Process Plant**
Michael Kanisuru Adeyeri, Sesan Peter Ayodeji, Emmanuel Olatunji Outomilola, Janet Omoyeni Bako
-

MFL Based Prototype and Experimental Work for Detection of Defects in Cables of Bridge Structures

Emad Abdelsalam^{a*}, Feras Kafiah^a, Sanad Kiswani^a, Dana Ibrahim^a, Al Ghorbanpoor^b

^a School of Engineering Technology, Al Hussein Technical University, Amman 11831, Jordan

^b Civil & Environmental Engineering Department, 3200 North Cramer Street, Milwaukee, WI 53211, USA

Received May 10 2020

Accepted November 3 2020

Abstract

This work offers experimental work and a prototype device based on the Magnetic Flux Leakage (MFL) method to inspect and detect corrosion in the cables of cable-stayed bridges. The developed prototype was constructed from two flat permanent magnets to provide a uniform magnetic field. A Hall-effect assembly was designed and developed. The assembly was placed between the two magnets in order to detect magnetic field changes due to defects inside the cable. Experimental work and tests were conducted on a constructed real cable, with various size of fabricated defect sizes. The results show that the MFL method is capable of detecting loss of section due to corrosion defects of varying sizes. Considerable success has been achieved in detecting steel defects from a single broken wire to seven broken wires (full strand fracture), particularly at the surface of the steel (about 3.8 cm depth from the surface of the cable). However, limited success has been achieved in detecting defects at the center of the steel cable, limited to detecting the seven broken wires defect only.

© 2020 Jordan Journal of Mechanical and Industrial Engineering. All rights reserved

Keywords: NDE; Cable-Stayed Bridges; MFL; Corrosion;

1. Introduction

In the last seventy five years, a large number of bridges have been built in the United States and around the world. A majority of these bridge structures rely on stressed steel cables to carry all relevant loads from traffic, environmental effects, such as wind and temperature, earthquakes, and the weight of the structure. Over time, these bridges age and become exposed to environmental conditions, such as rain, snow, de-icing and harmful chemicals. These conditions cause various levels of deterioration in the steel, particularly corrosion. Having said that, corrosion causes a loss of cross-section in the steel, adversely affecting the bridge's capacity to carry its service loads, and can possibly place the bridge's performance and safety in a critical condition. Several cases of post-tensioned (P-T) cable corrosion in bridges have been reported throughout the world. For example, in the summer of 1999, Florida Department of Transportation (FDOT) discovered corrosion in multiple bridges including the Niles Channel Bridge in the Florida Keys. Also, in 2000, a fractured tendon and advanced stages of corrosion in the cable anchorage area were observed during a routine bridge inspection by FDOT at the Mid-bay Bridge near Destin. Moreover, similar problems have been discovered at the Skyway Bridge in Tampa, FL [1]. Also, bridge collapses due to excessive corrosion have been reported in the United States and in other parts of the world [2]–[7]. According to the above, there is a direct need for developing appropriate

inspection methods to effectively detect corrosion in bridge cables and evaluate the structural integrity, performance and safety of such structures. While different defects are formed in various structural members in bridge structures, the focus of this work is placed on the corrosion problems in primary steel cables of large bridges. Such cables are normally enclosed in protective polyethylene, metallic ducts or wrapping materials to prevent exposure to moisture and outside environment. As such, no visual evaluation is possible and there have been no practical commercial technologies that could be used to evaluate the condition of these bridge cables. There are many NDE methods such as X-ray, Ultrasound, Electrical Resistance gages, Time Domain Reflectometry, Linear Polarization, vibration techniques, Surface Potential Survey and Thermography that may be applicable for bridge cables inspection [8]–[28]. Although these NDE methods may offer some evaluation capabilities for bridge cables, it has been shown that they are ineffective in the detection of corrosion in bridge cables [10]–[19], [21]–[46]. However, the MFL concept has been successfully demonstrated to be effective in detecting defects such as loss of section and corrosion in external P-T ducts of concrete bridge structures [37], [43]–[52]. Based on the literature survey, it was found that only the MFL method can offer both the performance required to detect corrosion in bridge steel cables and the effectiveness for field applications [37], [43]–[46]. This work presents development and laboratory evaluation of an MFL system that is capable of inspecting and detecting steel corrosion in cable supported bridge structures. The work is part of our

* Corresponding author e-mail: Emad.Abdelsalam@htu.edu.jo.

proposed NDE system that combines MFL and Magnetostrictive techniques [53]. The MFL prototype and experimental work laid the ground for the feasibility of combining the Magnetostrictive and the MFL method to develop a comprehensive system that is not only capable of inspecting the entire length of the cable of the cable-stayed bridge, but also the anchorage area. Such system is not commercially available. There are systems in the market that use MFL, mostly cylindrical magnet with sensors [47], that can be mounted on the cable, but cannot inspect the anchorage area.

2. Theory and Concept

The basic principle behind the MFL method is to apply a magnetic field near the surface of the steel cable and monitor the variation of the magnetic flux in the cable. The magnetic field must be strong enough to adequately penetrate through the steel cable. Since steel is a ferromagnetic material, magnetic flux will flow through the steel and be confined within the steel structure, Figure 1.

However, if there is a deficiency in the physical structure of the steel, such as a loss of cross section due to corrosion or fracture, the magnetic flux will leak to the surrounding environment, Figure 1b. This is referred to as “magnetic fringing” phenomenon. To take advantage of this phenomenon, magnetic sensors, like Hall-effect, are placed near the surface of the cable where an electrical signal can be observed and recorded in the form of voltage variations due to magnetic fringing. This signal, which is an indication of the presence of the flaw, can then be used to evaluate the severity of the deterioration. The magnitude and duration of the signal varies based on several factors, including the depth, size and shape of the defect in the steel cable.

The flux leakage is dependent on the size of the flaw, strength of the magnetic field, and the distance between the flaw and magnetic sensor. The stronger the magnetic field, the more the leakage of the flux lines. Similarly, the larger the flaw is, the more leakage of the magnetic field. Figure 2 demonstrates the concept of MFL and the effect of magnetic field strength on the density of leakage flux.

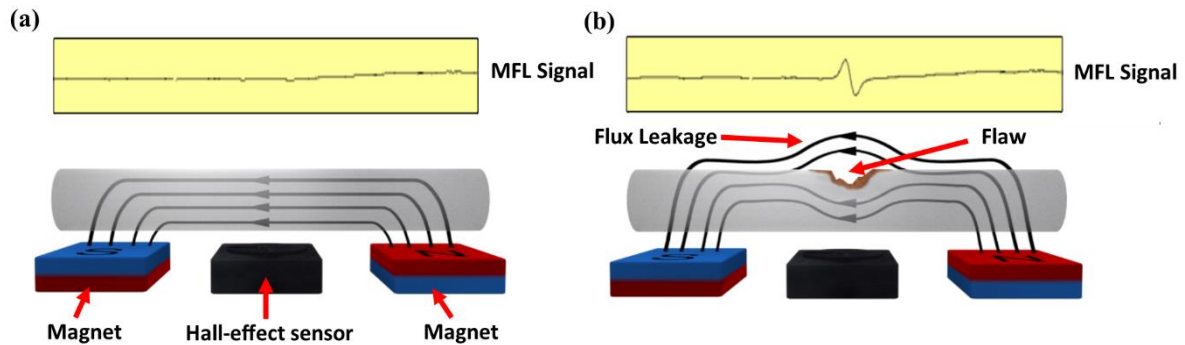


Figure 1. Demonstrating MFL concept: (a) without flaw in a steel bar, (b) with a flaw in a steel bar.

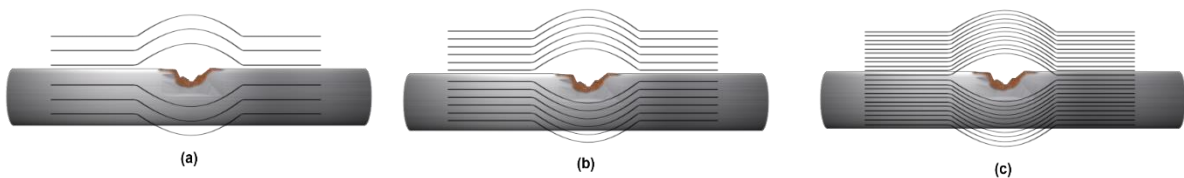


Figure 2. Effect magnetic field strength on the density of induced flux lines. (a) Low magnetic field, (b) Medium magnetic field and (c) Strong magnetic field.

2.1. Mathematical Model

The MFL technique has been widely used in NDE for detecting metal-loss due to corrosion or fatigue cracking problems in steel structures, particularly for inspecting oil and gas pipelines. The usage of the MFL technique to inspect gas pipelines goes back to early 1960's [54]–[64]. Similar to other NDE techniques, the interest when using the MFL method is to be able to predict the characteristics (size and shape) of the defect by solving the inverse problem of the signal output recorded from MFL sensors. As such, many methods have been attempted to solve the inverse problem solution; these can be classified as model or non-model based methods. The model-based (numerical) methods use a physical model to solve the inverse problem. These methods rely on iterative and optimized loops to find the solution for the inverse problem based on an initial guess or prior knowledge of the MFL defect parameters. These methods rely on numerical models [58]–[60], such as finite element method (FEM), analytical models [61]–[63], [65] and neural networks [55], [56], [64]. Although numerical methods provide an accurate solution for the inverse problem, they are computationally expensive. Corrosion characteristics [66] and estimation of defect severity [67] were studied. On the other hand, analytical and neural network methods are less accurate due to the approximation made to drive them, but they are faster methods [68]. The non-model based methods use signal processing techniques to correlate the signal from the MFL sensor to the shape of the defect. For example, the neural network method is used

to train the model to predict the shape of the MFL signal based on prior knowledge. However, the model is usually limited to a specific region in the defect and is difficult to apply to an arbitrary shape defect [68]. Other methods combine the accuracy of the FEM methods with the efficiency of the analytical methods using space mapping (SM) [69]–[74]. In the recent work [68], edge detection method is used to predict the shape of the flaw from the top, while using SM methods to estimate the depth parameter for an arbitrary defect. Also, other methods [75] have been proposed for the mathematical models of MFL defects based on the type of defect. Metal loss defects are classified as surface and sub-surface defects. For surface defects, the focus of the work was to develop an analytical model for a slot-type defect. As such, different models have been proposed which include Förster [76], Zatsopin and Shcherbinin [77], [78]. For sub-surface defects, the work was focused on two particular types of defects, cylindrical and spherical. The steel used in cable-stayed bridges is a bundle of either straight wires or strands; each strand consisting of a certain number of individual twisted wires, as shown in Figure 3. Although defects can be of any shape, it is reasonable to consider fractured wires as a target defect for our work following the same approach and consideration for similar types of research. As such, a broken wire is best represented by cylindrical sub-surface flaw, as seen in Figure 4. The mathematical model for a sub-surface cylindrical flaw, has been developed by Swartzendruber [79].

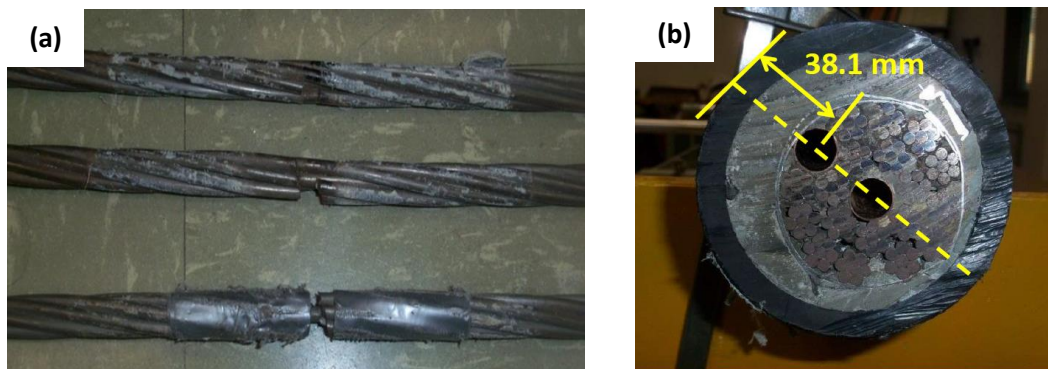


Figure 3. (a) Typical steel strands with a bundle of wires used in cable-stayed bridge; showing man-made defects, from top to bottom, of one broken wire, two broken wires and five broken wires. (b) Cable showing bundle of steel wires/strands with concrete grout and protective cover.

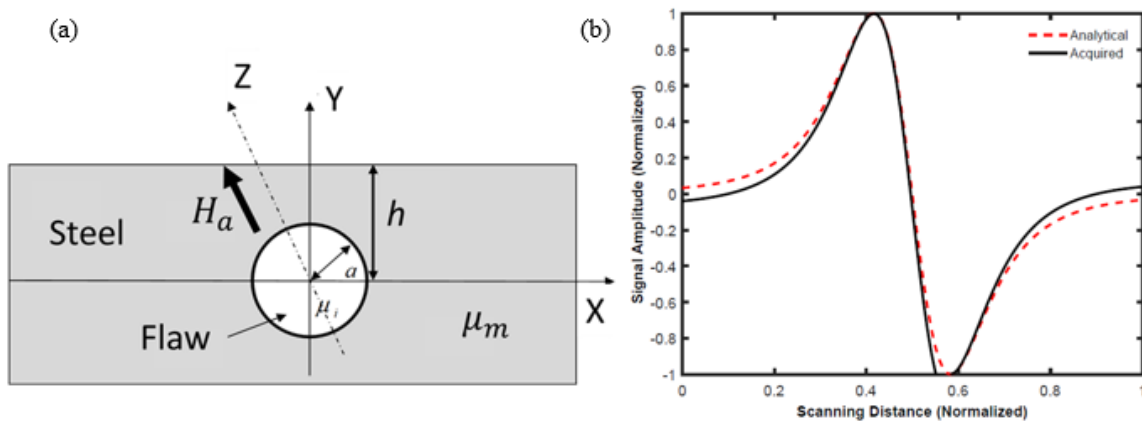


Figure 4: (a) MFL Mathematical Model: Illustration of sub-surface cylindrical flaw. (b) Acquired MFL signal and predicted signal based on the mathematical model in equation (2).

The analytical model for the magnitude of the flux leakage for a sub-surface cylindrical flaw of a radius a and depth h can be described with the following equation [79]:

$$m = \frac{2\mu_m}{\mu_m + \mu_i} \left[1 - \left(\frac{\mu_m - \mu_i}{\mu_m + \mu_i} \right)^2 \left(\frac{a}{2h} \right)^2 \right]^{-1} \frac{\mu_m - \mu_i}{\mu_m + \mu_i} H_a a^2 \quad (1)$$

$$H_y = \frac{2xy}{(x^2 + y^2)^2} (m - 2H_a a^2) \quad (2)$$

$$H_x = \frac{(x^2 - y^2)}{(x^2 + y^2)^2} (m - 2H_a a^2) \quad (3)$$

Where,

μ_m is permeability of the material under test; μ_i is permeability of the cylindrical defect; h is the depth of the flaw; a radius of the flaw; H_a is the applied magnetic field; H_x is the horizontal component of the magnetic field; H_y is the vertical component of the magnetic field.

The mathematical model stated above represents the flux leakage for a sub-surface cylindrical defect in a two-dimensional form. Figure 4 shows a comparison between a real magnetic flux leakage flaw signal from a test and that from the mathematical model of equation (2). The figure demonstrates that there is a good agreement between the signals from the real flaw and the mathematical model. The mathematical model shown above represents the flux leakage for a sub-surface cylindrical flaw in 2D only and it does not relate to the length of the flaw.

3. System Prototype

The MFL system developed consists of two strong permanent magnets as shown in Figure 5 (a). Each magnet is polarized perpendicular to its surface where the flux lines travel from the north-pole surface of the first magnet to the south-pole surface of the second magnet. The pair of magnets is polarized opposite to each other to allow the flux lines to travel from one magnet to the other, creating a uniform magnetic field between the two magnets. The permanent magnets selected for the MFL system are two large Neodymium Iron Boron magnets that have a strength of approximately 2,200 gauss at the center of each piece. Each one of the two magnets is a packed assembly of eight individual magnets of approximately 50 mm x 50 mm x 38 mm that are housed in a sealed stainless steel enclosure. The overall dimension of each magnet with the enclosure is approximately 210 mm x 108 mm x 46 mm. The weight of each magnet is approximately 6.2 kg. Each magnet's dimensions and layout have been optimized to provide a uniform magnetic field and maximum field penetration (50

to 75 mm from the surface of the cable) within the desired limits of detection for loss of section in bridge cables. A Hall-effect sensor enclosure that includes an array of ten Hall-effect sensors and a series of signal amplifiers have been placed between the two magnets. The Hall-effect sensors are placed at the isocenter of the two magnets to assure symmetry for the resultant MFL flaw signals. The Hall-effect sensors used in this MFL system are surface sensors and arranged to capture only the vertical component of the magnetic field leakage. The Hall-effect sensors are arranged in one array that consists of seven sensors. The lateral distance between each two adjacent sensors is kept at 25.4 mm. The sensors are arranged on a printed electrical circuit board along with electrical signal conditioning (amplification and filtration) hardware. The entire magnet and sensor assembly is mounted on an aluminum frame with wheels to allow moving the magnet on the surface of the cable. An encoder device is attached to one end of the frame to allow tracking of the position of the scan and subsequently it is used to identify the location of defects. The output of the sensors is connected to a data acquisition device. The data from sensors is collected and displayed in real time on a laptop computer using the LabVIEW software from the National Instrument Company (NI). The software has been designed to allow continuous display of data from all ten sensors simultaneously or from selected sensors only. Further post processing software application has been created to allow for data analysis.

4. Results and Discussion

To demonstrate the capabilities and effectiveness of the MFL system, several laboratory experiments were conducted. A 114.3 mm diameter bridge cable of 2.43 m long, which is similar to the commonly used bridge cables was used in the laboratory. The bridge cable consists of a bundle of 19 strands, as seen in Figure 3 (b). Two strands, one at the edge and one at the center of the strand bundle, were replaced by two copper tubes to allow insertion of strands with pre-set flaws in the laboratory bridge cable. Several defect sizes, from a single wire fracture to a complete strand fracture, were fabricated and inserted, one at a time, in the copper tube., Figure 5c. The magnet assembly was first mounted on top of the laboratory bridge cable and connected to the data acquisition software. The magnet assembly was then moved to a known starting point on the cable to establish a reference point for the start of the scan. The experiments were carried out by inserting a strand, with known flaws, into the top or the outer copper tube (25.4 mm) in the cable. The first inserted strand contained seven broken wires (complete strand fracture).

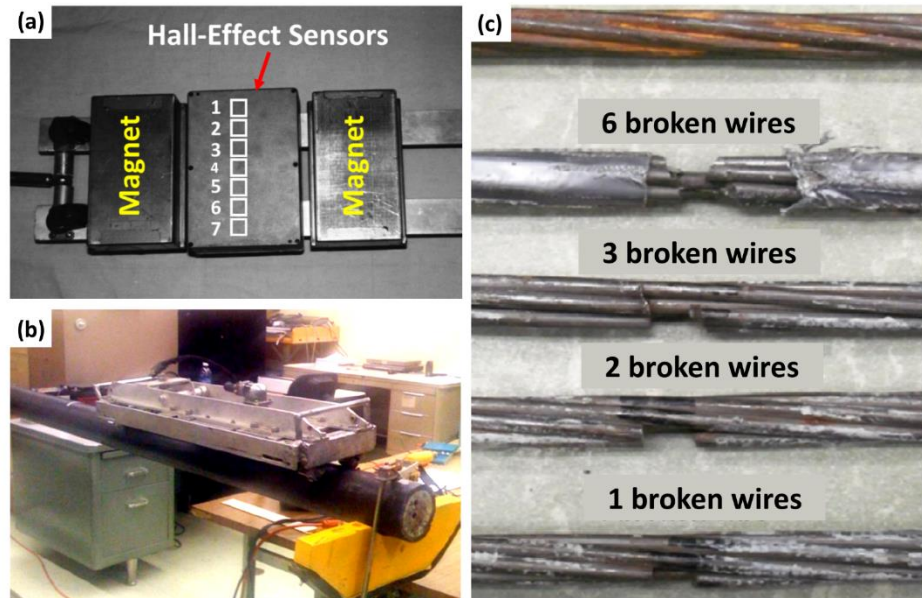


Figure 5. (a) The MFL system with two permanent magnets and a sensor enclosure (sensors 1 through 7) in the middle [37], [43]–[46] (b) MFL system installed on a laboratory bridge cable; showing 19 strands cable, with two strands inserted in the top and center holes in the cable. (c) Prestressing steel strands with no flaws (top) and with different sizes of flaws.

The strand was inserted inside the copper tube until it reached a predetermined length for the location of the flaw. The cable was scanned with the magnet assembly manually along the length of the cable in searching for flaws. The magnet assembly was moved as it passed the location of the flaw, and then stopped at the end of the cable. When the magnet reached at the end of the cable, data acquisition was stopped and the magnet was moved back to the start point, ready for the next scan. Data was collected continuously during each scan and it was transferred to the computer where it was saved for post-processing. The data from the seven Hall-effect sensors were collected and viewed in real-time while scanning the cable. When the first test was completed, the strand was removed and the second strand, with six broken wires, was inserted in the cable hole. Similar to the first scan, the magnet was moved over the flaw starting at the beginning of the cable from the same reference point and ending at the end of the cable moving exactly the same distance. The rest of the scanning was performed similarly for the remaining strands with varying defect sizes. When this part of the testing was completed, the first strand (with seven broken wires) was inserted in the center copper tube (located at 63.5 mm of depth) in the cable. The strand was pushed inside the cable until it reached the predetermined flaw location, similar to the first experiment, to maintain consistent location of the flaw within the cable.

4.1. Effect of seven broken wires at 38.1 mm depth inside the cable

The results of the first scan (seven broken wires in the outer copper tube) are shown in Figure 6. The x-axis of the graph represents the distance the magnet travelled during the scan. The y-axis represents the amplitude of the magnetic flux that leaked outside the steel. The graph shows only the vertical component of the magnetic flux; the flat line in the graph indicates that there is no flux leakage. Any

variations in the graph indicate the presence of a local disturbance of the magnetic field, and possibly an indication of the loss of section or presence of a flaw. The graphs clearly show strong variations based on the magnitude of the signal amplitude indicating the presence of disturbances near that area. Also, the data show that the signals recorded from all seven Hall-effect sensors vary in magnitude based on the location of each sensor. The maximum peak-to-peak magnitude ($0.9 V_{pk-pk}$) is observed at sensor four which is the closest sensor to the flaw. Additionally, the graph shows that the signal amplitude decreases from all other sensors as they are further away from the location of the flaw.

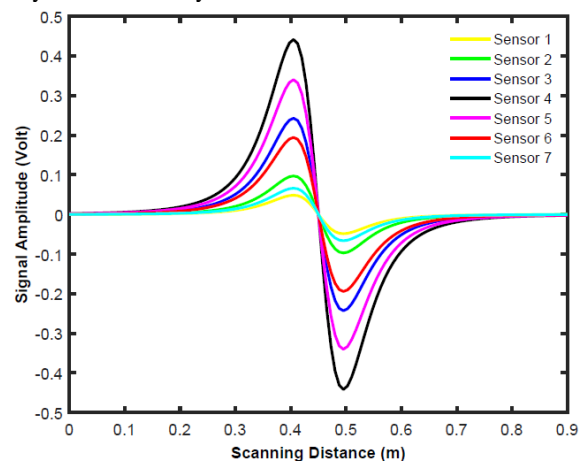


Figure 6. MFL signals recorded from sensors 1 through 7 for seven broken wires. Larger signal amplitude values are resulted from sensors that are located closer to the defects, i.e., data from sensors 4 and 5.

4.2. Effect of six broken wires at 38.1 mm depth inside the cable

In this experiment, the strand with seven broken wires was removed and a strand with six broken wires was

inserted in the top copper tube in the cable. Similar to the first scan, the magnet was moved over the flaw location traveling exactly the same distance on the cable. The signals recorded for the defects of the six broken wire-strand are shown in Figure 7. The signals from all seven sensors are almost identical to the defect signals of the seven-broken-wire strand, except that the peak-to-peak signal amplitude is lower. The data shows that the maximum signal amplitude recorded is about $0.8 V_{pk-pk}$; which corresponds to sensor four, as expected. The data also show that sensors 3 and 5 produced the next highest signal amplitude levels when compared to the signals from sensor four. It is also clear from the graphs that the signal from sensor one is the smallest since it is the farthest from the location of the defect.

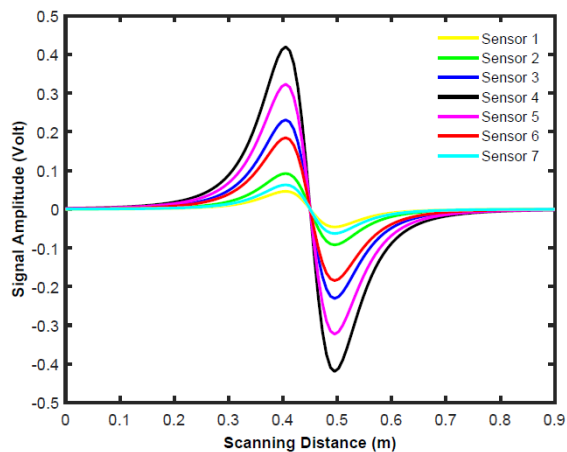


Figure 7. MFL signals recorded from sensors 1 through 7 for six broken wires. Larger signal amplitude values are resulted from sensors that are located closer to the defects, i.e., data from sensors 4 and 5.

4.3. Effect of five broken wires at 38.1 mm depth inside the cable

In this experiment, the strand with six broken wires was removed and a strand with five broken wires was inserted in the outer copper tube in the cable. The data for the defect of the five broken wires in the strand is shown in Figure 8. Consistent with the previous two experiments for 7-wires and 6-wires broken strands, the maximum signal is recorded from sensor four. As seen from the graph, the peak-to-peak magnitude of the signal for sensors four is about $0.7 V_{pk-pk}$. The signals from the rest of the sensors follow the pattern as in the previous two experiments, where sensor one shows the smallest magnitude.

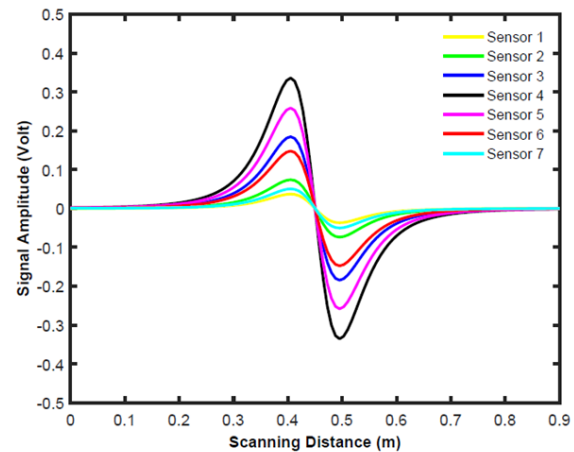


Figure 8. MFL signals recorded from sensors 1 through 7 for five broken wires. Larger signal amplitude values are resulted from sensors that are located closer to the defects, i.e., data from sensors 4 and 5.

4.4. Effect of four broken wires at 38.1 mm depth inside the cable

In this experiment, the strand with five-broken-wires was removed and a strand with four broken wires was inserted in the outer copper tube in the cable. The data is shown in Figure 9. Consistent with the previous results, the maximum signal is recorded from sensor four with $0.5 V_{pk-pk}$. The signals from the rest of the sensors follow the pattern as in the previous experiments, where, sensor one shows the smallest magnitude.

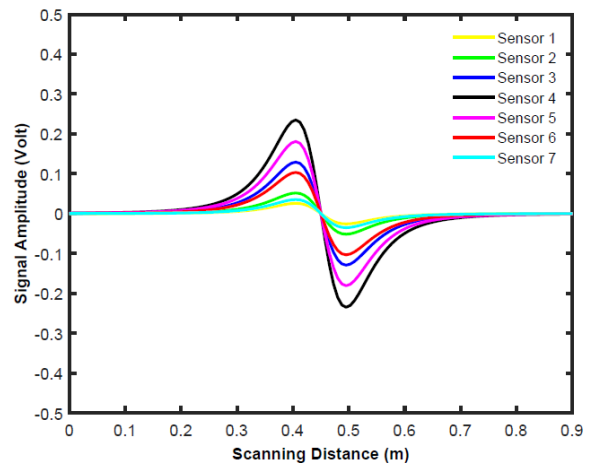


Figure 9. MFL signals recorded from sensors 1 through 7 for four broken wires. Larger signal amplitude values are resulted from sensors that are located closer to the defects, i.e., data from sensors 4 and 5.

4.5. Effect of three broken wires at 38.1 mm depth inside the cable

The data for the defect in a strand with three broken wires are shown in Figure 10. As seen from the graph, the peak-to-peak magnitude of the signal for sensor four about 0.35 V_{pk-pk}. The signals from the rest of the sensors follow the pattern as in the previous experiments, where, sensor one shows the smallest magnitude.

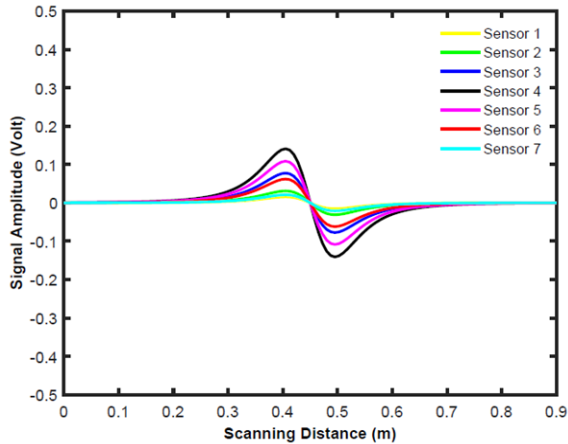


Figure 10. MFL signals recorded from sensors 1 through 7 for three broken wires. Larger signal amplitude values are resulted from sensors that are located closer to the defects, i.e., data from sensors 4 and 5.

4.6. Effect of two broken wires at 38.1 mm depth inside the cable

The data for the defects for the two broken wires strand is shown in Figure 11. As seen from the graph, the peak-to-peak magnitude of the signals from sensor four is almost about 0.15 V_{pk-pk}. The signals from the rest of the sensors follow the pattern as in the previous experiments, where, sensor one shows the smallest magnitude.

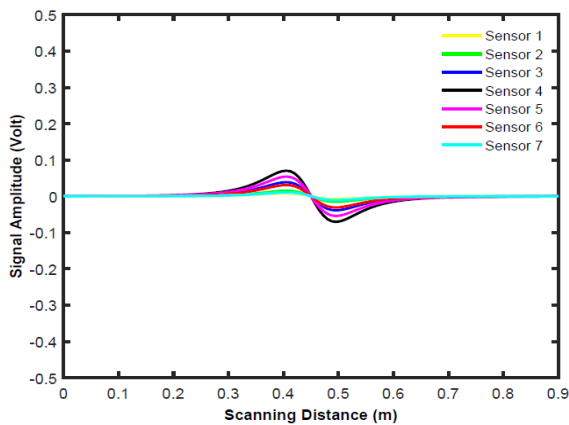


Figure 11. MFL signals recorded from sensors 1 through 7 for two broken wires. Larger signal amplitude values are resulted from sensors that are located closer to the defects, i.e., data from sensors 4 and 5.

4.7. Effect of one broken wire at 38.1 mm depth inside the cable

In the last experiment, a strand with one broken wire defect was inserted in the outer copper tube in the cable. The results for this experiment are shown in Figure 12. As seen

from the graph, the peak-to-peak magnitude of the signal for sensor four is about 0.075 V_{pk-pk}.

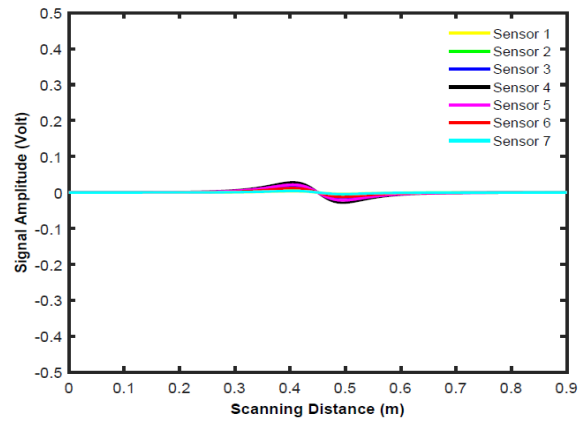


Figure 12. MFL signals recorded from sensors 1 through 7 for one broken wire. Larger signal amplitude values are resulted from sensors that are located closer to the defects, i.e., data from sensors 4 and 5.

The results of the experiments are summarized in Figure 13. The graph shows that the MFL system offers good response and sensitivity to the size of flaws varying from 1-broken wire to 7-broken wires in a strand. The experiments were carried out on single isolated defects (defects that are far from each other). However, when defects were very close to each other, it was difficult to visually distinguish the MFL signal for each individual defect. For example, the presence of a large defect next to relatively small defect may mask the signal from the small defect, which may alter the shape of the signal of the large defect. This may suggest the need for more sophisticated signal processing or pattern recognition techniques to improve defect detectability. Additionally, the developed prototype model is a rectangular magnet, it can only cover a section of the diameter of the cable. Hence, rotating the magnet around the diameter of the cable and rescanning is necessary to ensure full coverage of the diameter of the cable. However, this is not practical and is time consuming. Furthermore, keeping the magnet in a straight-line during scanning along the length of the cable is another practical challenge. Hence, motion alignment, tracking and adjustment are necessary. Installing the device on the cable is also another practical problem, as the magnet is very strong and can easily pull towards the cable quickly due to the magnetic force.

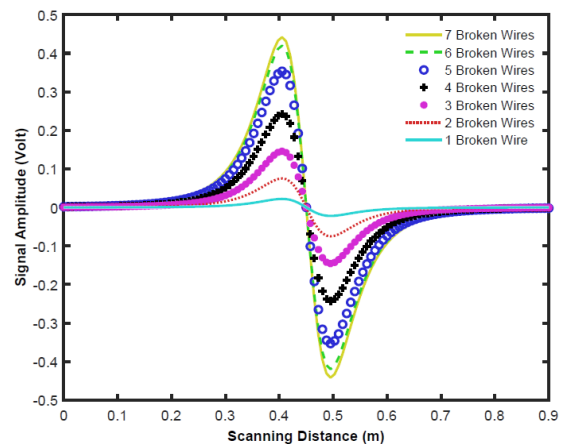


Figure 13. Summary of MFL signals recorded from sensors four for one broken wires to seven broken wires.

5. Conclusion

The use of MFL method has been studied and evaluated for detecting section losses in the bridge cables through experimental work. A prototype model of the MFL system has been used. Also, data acquisition hardware for signal amplification and conditioning has been developed. Furthermore, data acquisition software for real-time acquisition and post-processing analysis has been developed. A grouted 127 mm diameter bridge cable that consists of pre-stressing strands has been used for the MFL experiments to evaluate the system performance. The results have shown that the MFL technique is capable of detecting corrosion-related defects (section loss) inside the cable. These include a single broken wire within one strand to several broken wires with considerable success if the location of the flaw is within about 38.1 mm from the surface of the cable. However, successful section loss detection at the center of the steel cable has been limited to seven broken wires. The current MFL system built based on a flat rectangular magnets can only cover a portion of the circumference of the cable. As such, it is necessary to rotate the magnets around the cable and repeat the scans for the entire length of the cable several times to cover the full volume of the cable. This is not practical in the field, especially for long span bridges where the length of each bridge cable may exceed 426 m. To address this limitation, a new design based on cylindrical magnets can be proposed for future work.

References

- [1] Florida Department of Transportation (FDOT) Report, "Post-tensioned Bridges, Topic No. 700-000-000, Section 10.7," 2004.
- [2] A. G. Lichtenstein, "The silver bridge collapse recounted," *J. Perform. Constr. Facil.*, vol. 7, no. 4, pp. 249–261, 1993.
- [3] K. P. Chong, N. J. Carino, and G. Washer, "Health monitoring of civil infrastructures," *Smart Mater. Struct.*, vol. 12, no. 3, p. 483, 2003.
- [4] D. Appell, "Repairs without rivets.," *Sci. Am.*, vol. 297, no. 5, pp. 21–22, 2007.
- [5] R. J. Woodward and F. W. Williams, "COLLAPSE OF YNS-Y-GWAS BRIDGE, GLAMORGAN.," *Proc. Inst. Civ. Eng.*, vol. 84, no. 4, pp. 635–669, 1988.
- [6] D. Parker, "Pacific bridge collapse throws up doubt on repair method," *New Civ. Eng.*, vol. 12, pp. 12–96, 1996.
- [7] D. Parker, "Tropical overload," *New Civ. Eng.*, pp. 18–21, 1996.
- [8] D. E. Bray and R. K. Stanley, *Nondestructive evaluation: a tool in design, manufacturing and service*. CRC press, 1996.
- [9] P. J. Shull and C. R. C. Press, "Nondestructive Evaluation Theory, Techniques and Applications,(2002)." Marcel Dekker.
- [10] J. L. Robert and M. Brachet-Rolland, "Survey of structures by using acoustic emission monitoring," *IABSE REPORTS*, vol. 39, 1982.
- [11] M. Schupack, "Evaluation of Corrosion in Bonded and Unbonded Post-Tensioned Structures. How to make Today's Repairs Durable for Tomorrow," Houston, Texas, 1998.
- [12] S. Feliu, J. A. Gonzalez, C. Andrade, and I. Rz-Maribona, "Errors Introduced by the Guard Ring Device in the On-Site Measurement of Rebar Corrosion Rates. Corrosion of Reinforcement in Concrete. Papers Presented at the Third International Symposium On" Corrosion of Reinforcement in Concrete Construction", Belfry ,” *Publ. CICC Publ.*, pp. 293–302, 1990.
- [13] D. G. John and D. Eden, "Corrosion measurements on reinforcing steel and monitoring of concrete structures," *Corros. Met. Concr.*, pp. 159–167, 1987.
- [14] W. K. Green, S. B. Lyon, and J. D. Scantlebury, "Electrochemical changes in chloride-contaminated reinforced concrete following cathodic polarisation," *Corros. Sci.*, vol. 35, no. 5–8, pp. 1627–1631, 1993.
- [15] R. H. Suresh Babu, N. U. Nayak, C. Srividya Rajagopalan, S. Srinivasan, N. S. Rengaswamy, and Y. Mahadeva Iyer, "Monitoring of corrosion of prestressing steel cables in prestressed concrete bridges," *Trans. SAEST*, vol. 23, no. 2–3, pp. 203–206, 1988.
- [16] American Society for Testing Materials, "Standard Test Method for Half-Cell Potentials of Reinforcing in Concrete."
- [17] C. C. Naish, A. Harker, and R. F. A. Carney, "Concrete inspection: interpretation of potential and resistivity measurements," *CICC Publ. - Corros. Reinf. Concr.*, pp. 314–332, 1990.
- [18] E. Escalante, "Effectiveness of potential measurements for estimating corrosion of steel in concrete," *Elsevier Appl. Sci.*, pp. 281–292, 1990.
- [19] D. J. Daniels, "Surface-penetrating radar," *Electron. Commun. Eng. J.*, vol. 8, no. 4, 1996.
- [20] C. Hellier, *Handbook of Nondestructive Evaluation*, 2001st ed. McGraw-Hill Education, 2001.
- [21] N. J. Carino, "The impact-echo method: an overview," in *Structures 2001: A Structural Engineering Odyssey*, 2001, pp. 1–18.
- [22] H. E. Martz, D. J. Scheberk, G. P. Roberson, and P. J. M. Monteiro, "Computerized tomography analysis of reinforced concrete," *Mater. J.*, vol. 90, no. 3, pp. 259–264, 1993.
- [23] C. Flohrer and B. Bernhardt, "Detection of Prestressed Steel Tendons Behind Reinforcement Bars, Detection of Voids in Concrete Structures - A Suitable Application for Radar Systems," in *Conference Proceedings of The British Institute of Non-Destructive Testing International Conference, NDT in Civil Engineering 14-16 April 1993, Liverpool University. Volume 1*, 1992, pp. 227–237.
- [24] C.-C. Cheng and M. Sansalone, "Effects on impact-echo signals caused by steel reinforcing bars and voids around bars," *Mater. J.*, vol. 90, no. 5, pp. 421–434, 1993.
- [25] Y. Lin and M. Sansalone, "Detecting flaws in concrete beams and columns using the impact-echo method," *Mater. J.*, vol. 89, no. 4, pp. 394–405, 1992.
- [26] D. Pratt and M. Sansalone, "Impact-echo signal interpretation using artificial intelligence," *Mater. J.*, vol. 89, no. 2, pp. 178–187, 1992.
- [27] N. J. Carino and M. Sansalone, "Detection of voids in grouted ducts using the impact-echo method," *Mater. J.*, vol. 89, no. 3, pp. 296–303, 1992.
- [28] C. G. Petersen, "DOCTer impact echo testing of the injection of a post-tensioned cable steel duct "," *Report-German Instruments A/S*, 1993.
- [29] M. G. Ali and A. R. Maddocks, "Evaluation of corrosion of prestressing steel in concrete using non-destructive techniques," *Non-Destructive Testing-Australia*, vol. 40, no. 5, pp. 42–48, 2003.
- [30] M. B. Leeming, J. S. Lane, and P. J. Wade, "Post-tensioned bridge investigation-the way forward," in *Proceedings of the sixth international conference on structural faults and repair*, 1995, pp. 193–197.
- [31] R. T. Stain, "Dixon, 5,—Inspection of cables in post-tensioning bridge-What techniques are available "," *Construction/Repair*, pp. 297–300, 1994.
- [32] H. T. Williams and M. E. Hulse, "From theory to experience with inspection of post-tensioned bridges," in *Proc., 6th Int.*

- Conf. on Structural Faults and Repairs*, 1995, vol. 1, pp. 199–202.
- [33] M. Nagi and D. Whiting, “Corrosion of prestressed reinforcing steel in concrete bridges: State-of-the-art,” *Spec. Publ.*, vol. 151, pp. 17–42, 1994.
- [34] ANON, “Inspection of Prestressing Cables in Bridges,” *Indian Concr. J.*, vol. 61, no. 2, pp. 31–33, 1987.
- [35] O. Büyüköztürk, “Imaging of concrete structures,” *Ndt E Int.*, vol. 31, no. 4, pp. 233–243, 1998.
- [36] W. I. J. Price, “Highway Bridge Inspection: Principles And Practices In Europe,” *IABSE REPORTS*, vol. 38, 1982.
- [37] G. R. Steber, A. Ghorbanpoor, and T. E. Shew, “Magnetic field disturbance signal processing,” in *15th Annual Conference of IEEE Industrial Electronics Society*, 1989, pp. 474–479.
- [38] A. Ghorbanpoor and T. E. Shew, “Detection of flaws in bars and cables in concrete bridge structures,” *Transp. Res. Rec.*, no. 1211, pp. 84–91, 1989.
- [39] B. Gimmel, “Magnetoelastic Force Measurement in Prestressed Concrete,” in *Durability of Structures. IABSE Symposium, September 6-8 1989, Lisbon (IABSE Report Volume 57/1)*, 1989, pp. 239–334.
- [40] H. Scheel and B. Hillemeier, “Capacity of the remanent magnetism method to detect fractures of steel in tendons embedded in prestressed concrete,” *NDT E Int.*, vol. 30, no. 4, pp. 211–216, 1997.
- [41] M. G. Fontana, *Corrosion engineering*. Tata McGraw-Hill Education, 2005.
- [42] M. Huang, L. Jiang, P. K. Liaw, C. R. Brooks, R. Seeley, and D. L. Klarstrom, “Using acoustic emission in fatigue and fracture materials research,” *JOM*, vol. 50, no. 11, pp. 1–14, 1998.
- [43] A. Ghorbanpoor, R. Borchelt, M. Edwards, and E. A. Salam, “Magnetic-Based NDE of Prestressed and Post-Tensioned Concrete Members: The MFL System,” 2000.
- [44] A. Ghorbanpoor, G. R. Steber, and T. E. Shew, *Evaluation of Steel in Concrete Bridges: The Magnetic Field Disturbance (MFD) System*. Federal Highway Administration, 1991.
- [45] E. Abdelsalam, “Corrolation Analysis of Flaw Signal Detected by the MFD System,” University of Wisconsin-Milwaukee, 1998.
- [46] Engineering News-Record, “Magnetic Flux Leakage is Powerful New Force in Bridge Inspection,” *Equip. Tracks Trends*, vol. 244, no. 11, p. 35, 2000.
- [47] H. B. Yun, S. H. Kim, L. Wu, and J. J. Lee, “Development of inspection robots for bridge cables,” *Sci. World J.*, vol. 2013, no. December, 2013, doi: 10.1155/2013/967508.
- [48] Y. Ma, L. Lin, K. Jiang, and X. Zhao, “The application of magnetic shielding effect in drill pipe magnetic leakage flux testing,” *Proc. - 2013 5th Conf. Meas. Technol. Mechatronics Autom. ICMTMA 2013*, no. 1, pp. 1135–1138, 2013, doi: 10.1109/ICMTMA.2013.277.
- [49] K. Muramatsu, Y. Gao, Y. Moriyama, H. Dozono, T. Nishino, and K. Miura, “Modeling of Leakage Magnetic Field of Electric Machines Using Blocks with Magnetizations for Design of Magnetically Shielded Room,” *IEEE Trans. Magn.*, vol. 53, no. 6, pp. 2015–2018, 2017, doi: 10.1109/TMAG.2017.2657639.
- [50] A. Azad and N. Kim, “Design and optimization of an MFL coil sensor apparatus based on numerical survey,” *Sensors (Switzerland)*, vol. 19, no. 22, 2019, doi: 10.3390/s19224869.
- [51] K. Tsukada *et al.*, “Detection of Inner Corrosion of Steel Construction Using Magnetic Resistance Sensor and Magnetic Spectroscopy Analysis,” *IEEE Trans. Magn.*, vol. 52, no. 7, pp. 1–4, 2016, doi: 10.1109/TMAG.2016.2530851.
- [52] K. Tsukada *et al.*, “Detection of Inner Cracks in Thick Steel Plates Using Unsaturated AC Magnetic Flux Leakage Testing with a Magnetic Resistance Gradiometer,” *IEEE Trans. Magn.*, vol. 53, no. 11, pp. 1–5, 2017, doi: 10.1109/TMAG.2017.2713880.
- [53] A. Salam and E. Ismail, “System for Detection of Defects in Cables of Bridge Structures,” 2013.
- [54] S. R. H. Hoole, “Artificial neural networks in the solution of inverse electromagnetic field problems,” *IEEE Trans. Magn.*, vol. 29, no. 2, pp. 1931–1934, 1993.
- [55] P. Ramuhalli, L. Udpa, and S. Udpa, “Neural network algorithm for electromagnetic NDE signal inversion,” *Electromagn. Nondestruct. Eval.*, pp. 121–128, 2001.
- [56] P. Ramuhalli, L. Udpa, and S. S. Udpa, “Neural network-based inversion algorithms in magnetic flux leakage nondestructive evaluation,” *J. Appl. Phys.*, vol. 93, no. 10, pp. 8274–8276, 2003.
- [57] R. Schifini and A. C. Bruno, “Experimental verification of a finite element model used in a magnetic flux leakage inverse problem,” *J. Phys. D. Appl. Phys.*, vol. 38, no. 12, pp. 1875–1880, 2005.
- [58] Z. Chen, G. Preda, O. Mihalache, and K. Miya, “Reconstruction of crack shapes from the MFLT signals by using a rapid forward solver and an optimization approach,” *IEEE Trans. Magn.*, vol. 38, no. 2, pp. 1025–1028, 2002.
- [59] M. Yan, S. Udpa, S. Mandayam, Y. Sun, P. Sacks, and W. Lord, “Solution of inverse problems in electromagnetic NDE using finite element methods,” *IEEE Trans. Magn.*, vol. 34, no. 5, pp. 2924–2927, 1998.
- [60] C. Mandache and L. Clapham, “A model for magnetic flux leakage signal predictions,” *J. Phys. D. Appl. Phys.*, vol. 36, no. 20, pp. 2427–2431, 2003.
- [61] D. Minkov, J. Lee, and T. Shoji, “Study of crack inversions utilizing dipole model of a crack and Hall element measurements,” *J. Magn. Magn. Mater.*, vol. 217, no. 1–3, pp. 207–215, 2000.
- [62] C. Edwards and S. B. Palmer, “The magnetic leakage field of surface-breaking cracks,” *J. Phys. D. Appl. Phys.*, vol. 19, no. 4, pp. 657–673, 1986.
- [63] A. Joshi, L. Udpa, S. Udpa, and A. Tamburrino, “Adaptive wavelets for characterizing magnetic flux leakage signals from pipeline inspection,” *IEEE Trans. Magn.*, vol. 42, no. 10, pp. 3168–3170, 2006.
- [64] P. Ramuhalli, L. Udpa, and S. S. Udpa, “Electromagnetic NDE signal inversion by function-approximation neural networks,” *IEEE Trans. Magn.*, vol. 38, no. 6, pp. 3633–3642, 2002.
- [65] D. Minkov and T. Shoji, “Method for sizing of 3-D surface breaking flaws by leakage flux,” *NDT E Int.*, vol. 31, no. 5, pp. 317–324, 1998.
- [66] E. Vannan and P. Vizhian, “Corrosion Characteristics of Basalt Short Fiber Reinforced with Al-7075 Metal Matrix Composites,” 2015.
- [67] V. V. Rao and C. Ratnam, “Estimation of Defect Severity in Rolling Element Bearings using Vibration Signals with Artificial Neural Network,” 2015.
- [68] M. Ravan, R. K. Amineh, S. Koziel, N. K. Nikolova, and J. P. Reilly, “Sizing of 3-D arbitrary defects using magnetic flux leakage measurements,” *IEEE Trans. Magn.*, vol. 46, no. 4, 2009.
- [69] J. W. Bandler, Q. Cheng, D. H. Gebre-Mariam, K. Madsen, F. Pedersen, and J. Sondergaard, “EM-based surrogate modeling and design exploiting implicit, frequency and output space mappings,” in *IEEE MTT-S International Microwave Symposium Digest, 2003*, 2003, vol. 2, pp. 1003–1006.
- [70] J. W. Bandler *et al.*, “Space mapping: the state of the art,” *IEEE Trans. Microw. Theory Tech.*, vol. 52, no. 1, pp. 337–361, 2004.
- [71] D. Echeverría and P. W. Hemker, “Space mapping and defect correction,” *Comput. Methods Appl. Math.*, vol. 5, no. 2, pp. 107–136, 2005.
- [72] S. Koziel, J. W. Bandler, and K. Madsen, “A space-mapping framework for engineering optimization—Theory and

- implementation," *IEEE Trans. Microw. Theory Tech.*, vol. 54, no. 10, pp. 3721–3730, 2006.
- [73] R. K. Amineh, S. Koziel, N. K. Nikolova, J. W. Bandler, and J. P. Reilly, "A space mapping methodology for defect characterization from magnetic flux leakage measurements," *IEEE Trans. Magn.*, vol. 44, no. 8, pp. 2058–2065, 2008.
- [74] J. W. Bandler, S. Koziel, and K. Madsen, "Space mapping for engineering optimization," *SIAG/Optimization Views-and-News Spec. Issue Surrog. Optim.*, vol. 17, no. 1, pp. 19–26, 2006.
- [75] N. N. Zatsepin and V. E. Shcherbinin, "On calculation of magnetostatic field generated by surface flaws. I," *Topogr. fields flaws Model. Defektoskopiya*, vol. 5, pp. 50–59, 1966.
- [76] F. Förster, "Nondestructive inspection by the method of magnetic leakage fields- Theoretical and experimental foundations of the detection of surface cracks of finite and infinite depth," *Sov. J. Nondestruct. Testing*, (ISSN 0038-5492), vol. 18, no. 11, pp. 841–858, 1983.
- [77] N. N. Zatsepin, V. E. Shcherbinin, and A. M. Pashagin, "Investigation of the Magnetic Field of Flaws on the Inner Surface of Ferromagnetic Pipes. 1," *Basic Regul. Mech. Flaw-f. Form. Defektoskopiya*, no. 2, pp. 8–16, 1969.
- [78] V. E. Shcherbinin and N. N. Zatsepin, "Calculation of the magnetostatic field of surface defects. I. Field topography of defect models," *Defectoscopy*, vol. 5, pp. 385–393, 1966.
- [79] L. J. Swartzendruber, "Magnetic leakage and force fields for artificial defects in magnetic particle test rings," in *In Proceedings of the XII Symposium on NDE (SWRI, San Antonio, TX)*, 1979, pp. 150–161.

A Technical and Economic Study of a Photovoltaic–phase Change Material (PV-PCM) System in Jordan

Salem Nijmeh^a, Bashar Hammad^b, Mohammad Al-Abed^{c,d,*}, Riad Bani-Khalid^{a,e}

^aDepartment of Mechanical Engineering, The Hashemite University, Zarqa, Jordan

^bDepartment of Mechanical and Maintenance Engineering, German Jordanian University, Amman, Jordan

^cDepartment of Biomedical Engineering, The Hashemite University, Zarqa, Jordan

^dCenter of Renewable Energy, Water, and Environment, The Hashemite University, Zarqa, Jordan

^eMinistry of Education, Amman, Jordan

Received August 11 2020

Accepted November 2 2020

Abstract

This work presents a technical and economic evaluation of the application of phase change material (PCM) in the cooling and thermal regulation of photovoltaic (PV) panels. The technical study is performed based on experimental tests carried out on two identical 3.99 kWp PV systems for one full year at the Hashemite University, Jordan. The backside of the first system was integrated with BioPCM. It is a safe, environmentally friendly, and economically sustainable product that is typically employed in the building industry to save energy in HVAC. This PCM has the potential to answer the many concerns associated with the traditional PCMs. The second PV system is used as a reference for performance comparison purposes. The actual performance results show there is an increase of 3.4% in the annual power production due to the application of BioPCM. The annual conversion efficiency is 12.50% for the PV/BioPCM system, while it is 12.08% for the reference PV system. The economic study investigates the viability of the inclusion of PCM in terms of the payback period, net present value, and internal rate of return. These parameters indicate that the PCM investment is economically unattractive at present.

© 2020 Jordan Journal of Mechanical and Industrial Engineering. All rights reserved

Keywords: photovoltaic systems; phase change material; experimental study; technical evaluation; economic feasibility;

1. Introduction

1.1. Energy situation in Jordan

Jordan is a Middle Eastern country with limited resources and an estimated population of about 10.554 million inhabitants in 2019 [1]. Jordan imports most of its primary energy requirements (92% in 2018), which leads to severe financial strain on the national economy. The cost of consumed energy reaches 10% of the GDP [2]. Jordan's energy strategy has focused primarily on reducing dependence on oil products, increasing natural gas, and alternative energy inputs, including renewable energy, especially in the electricity generation sector. It is blessed with high annual daily average solar irradiance, which ranges between 4-8 kWh/m², and adds up to a total of 1400-2300 kWh/m² annually [3].

The updated national energy strategy set a 10% target of renewable energy by 2020 [4]. To meet this target, the Renewable Energy and Energy Efficiency Law (REEEL) No.13 was approved in 2012 [5]. The law gives incentives and tax exemptions to promote the installation of renewable energy systems. The law allows the development of distributed electricity generation under the Net Metering and Wheeling mechanisms, allowing small RE installations

for different sectors to sell the exceeding electricity to the grid.

The most promising application of RE in Jordan is solar PV power generation. National Electric Power Company (NEPCO) estimates in 2018 that the electricity generated from solar energy amounted to nearly 7% [6]. Recent projects accomplished on the ground with the collaboration of the private sector include Almafraq and Al-Quweira solar PV plants with capacities of 100 MW and 103 MW, respectively. The largest project currently under construction is the Baynouna (east of Amman) with a 200 MWp solar power plant. The connectivity to the grid is expected in 2020 [7]. The total installed renewable capacity is expected to reach 2400 MWp by 2021, and that will constitute 20% of the total electricity generation [8].

1.2. Effect of rising temperature on PV modules

Rising temperature of PV module causes reduction in power output which is determined by temperature coefficient [9]. This coefficient depends on the type of cell and was determined as -0.446%/°C, -0.387%/°C, and -0.172%/°C for mono-crystalline, multi-crystalline and CdTe cells, respectively [10]. Another work [11] investigated the power-temperature coefficient for different types of modules. It shows that all thin-film technologies have lower values (-0.13%/°C to -0.36%/°C) in comparison

* Corresponding author e-mail: drnijmeh@hu.edu.jo.

with to the c-Si wafer-based modules ($-0.45\%/^{\circ}\text{C}$). The percentage loss at 80°C compared to power at Standard Test Condition ranges from 7.2% to 24.8%. Alrwashdeh [12] simulated the output of five PV panels at different operating temperatures in Amman, Jordan. The power output was reduced between 0.25% and 0.30% for each $^{\circ}\text{C}$ of temperature rise.

Another adverse effect of rising temperatures is accelerated degradation. The operating solar PV module at lower temperatures increases its lifespan [13]. The high temperatures cause stresses which accelerate degradation rates, with cell encapsulation and soldering being the most susceptible [14]. A study in the high-temperature desert region of Algeria predicted that the life of a PV module, under conditions of the open-circuit could be shortened by four years [15]. Another mathematical study by the same research group predicted that the annual rate of degradation is in the order of 1.5%/year [16]. This has led to a strong requirement for PV thermal control to increase panel power yield and lifespan [17].

1.3. Cooling techniques of PV panels

Many researchers have proposed and tested several new materials and techniques to manage the temperature of the PV systems thermally using passive and active means. The simplest and least expensive is by using natural- or forced-air cooling. A theoretical and experimental study conducted in Iraq shows that using fin cooling technique results in an increase in the module generated power by about 15.3% [18]. Natural ventilated systems can reach PV temperatures between $50\text{--}70^{\circ}\text{C}$ [19]. The main drawback of natural ventilation is the very high panel temperature during peak insolation [20].

As for the active or forced-air cooling, Amelia et al. [21] have developed an active air-cooling system using fans fitted at the backside of PV panels. It was found that the optimum number of DC fans used was two units. The power output increased by about 37.17% for this case. There is no mention of the electrical power consumed or the capital investment required.

There is a large number of technical studies on active water-cooling systems. Odeh and Behnia [22] did a long-term simulation of a solar PV water pumping system. The cooling of the PV module is obtained by water trickling on the upper surface. Results show an increase of 5% in energy output during dry and warm seasons. Irwan et al. [23] conducted an indoor test performance of a PV panel sprayed with water over the front surface. Results indicate that the power output increased by 9–22%. Bahaidarah et al. [24] introduced a water-cooled mono-crystalline PV module from the backside in the hot climate of Dhahran, Saudi Arabia. This has led to an improvement of 9% in efficiency.

Other works employed nanofluids in PV and PV/T (photovoltaic thermal) systems because of their higher thermal conductivity and heat capacity [25]. Hashim et al. [26] evaluated employing Al_2O_3 -water for cooling by applying forced convection. The authors concluded that at 0.3% concentration, the electrical efficiency rose from 8% to 12.1%. Ebaid et al. [27] carried out an experimental investigation of cooling PV cells using water and two different types of nanofluids under the real outdoor conditions of Jerash-Jordan. The generated power increases

for TiO_2 nanofluid and water as compared to no cooling by 6.05% and 3.75%, respectively. In general, active systems raise the cost greatly due to the pumping costs of air and water.

Other cooling techniques include heat thermosyphon cooling. Habeeb et al [28] studied the use of this method in cooling different PV modules. Results show that the efficiency is enhanced by 4–14% as compared with the reference module. One of the most critical techniques studied in the past few years is the photovoltaic cooling utilizing phase change materials (PCMs). Most of the work in literature are either theoretical or in laboratory. The few studies conducted under field conditions are for a short duration, which puts a significant limitation on the reliability, repeatability, and generalization of the results obtained [20].

1.4. Cooling techniques using PCM

1.4.1. Technical and economic feasibility studies

In general, PCMs are classified into three groups, organic which includes paraffin-based materials, inorganic, which includes salt hydrates, and eutectics of organic and inorganic compounds [29]. Organic PCMs have low thermal conductivity, high flammability, and can release toxic vapors [30]. This can be a problem in high insolation areas where the back-surface temperature of PV panels can exceed 80°C during peak hours. Also, for none of the systems studied in the literature, the economic advantage out-performed the invested cost. On the other hand, salt hydrates have high thermal conductivity and latent heat of fusion [29]. The main disadvantages may include solidification problems at night, corrosion, long term degradation, and chemical instability.

Literature works of cooling techniques using PCM are focused on the groups mentioned above. In a recent work carried out in Jordan [31], the effect of using PCM (paraffin graphite PCM47) on both the efficiency and power output using two identical PV panels was investigated. The theoretical results were compared with short-term outdoor experimental results in October. It is found that the PCM would give positive results only when the panel temperature surpasses the PCM melting temperature.

Another simulation and experimental study [32] was carried out in the city of Ljubljana using organic PCM (Rubitherm RT28 HC) with a melting temperature of 28°C . An average increase in efficiency of 1.1–2.8% was obtained based on temperature measurements. Simulation results reveal that the generated power rose by 7.3% in one year. On the other hand, a recent study [33] conducted under Mediterranean climate in Portugal on another organic product (Rubitherm RT 22 HC) concluded that the use of this PCM have a negative effect on the performance. The daily energy produced decreased between 3.3–6.5%, and it is concluded that a PCM with a higher melting temperature is required for this climate.

Nada and Nagar [34] investigated the performance of free stand and building-integrated PV modules using PCM (paraffin wax RT 55) and PCM with added 2% Al_2O_3 in Giza, Egypt. It was found that adding PCM to a building-integrated PV module improves its daily efficiency by 7% to 14.2%.

There are many technical studies on PV-PCM systems, but few studies investigated their cost and financial viability. A very recent work [35] investigated numerically paraffin-based PV-PCM and PV-FPCM (finned phase change material) systems for PV cooling under the climatic conditions of Southeast of England. The extracted heat is used for space heating. It was observed that the daily power increased by 7% for the PCM cooled system and 8% for the FPCM cooled system as compared with the reference PV. A short cost analysis study shows that PV-FPCM is not economical. The cost of electricity generation is 0.094 £/kWh for the PV system as compared with 0.119 £/kWh for the system using FPCM. This is due to the low irradiance level and low ambient temperatures. A short experimental study conducted in Lebanon [36] concluded that the installation of Petroleum jelly PCM would have a payback period of 12.3 years. Arici et al. [37] performed a simulation study on a 10 kW PV system with different PCMs in two Turkish cities (Ankara and Mersin). The calculated Levelized Cost of Energy (LCOE) varied between 0.13 €/kWh and 0.146 €/kWh, as compared with 0.096 €/kWh to 0.108 €/kWh for the reference PV system.

1.4.2. Criteria for selecting appropriate PCM for our tests

It can be seen that there are many concerns associated with traditional PCMs relating to safety, environment, and performance. This led the authoring team to consider a more environmentally friendly and safer product derived from sustainable, renewable sources. The PCM used in this work is the Phase Change Energy Solution BioPCM™ M51 Q25. It is made from a renewable and sustainable plant extract, which is picked and then manufactured into blankets [38,39]. The M-value gives the heat storage capacity of the material in Btu per square foot (51). The second code Q refers to the melting temperature of the BioPCM™ (25 °C in our case).

BioPCM™ is used in the building industry, where it is claimed that HVAC energy savings in the 25–35% range can be achieved. It is both a LEED and a BEES (Building for Environmentally and Economic Sustainability) friendly product. The product is tested to ASTM E84 Standards and meets or exceeds the safety guidelines of the building products industry [39].

This particular product was chosen based on availability and previous works on BioPCM™ in other applications recommending low melting temperatures. For example, a simulation study on BioPCM™ [40] investigated the thermal improvement through retrofitting existing residential buildings in the Mediterranean area. Results for Bari, Athens, and Tunis show that PCM M91/Q25 with a melting point temperature of 25 °C is the most effective. For example, energy savings of 66% was obtained for Bari for the whole summer. Similar results were obtained for Athens and Tunis with cooling savings of 43% in both cities. Another simulation work [41] investigated the use of 3 types of PCMs in envelopes of buildings. Results show that BioPCM™ with a low melting point temperature produced superior energy savings for the HVAC system over other types of PCMs. For example, electricity savings present in Tokyo were shown to be 9.69%. Hence, for the concerns and merits mentioned above, BioPCM™ M51 Q25 is selected for our tests. A technical and economic

evaluation of PV cooling employing this particular PCM is conducted in this work.

2. Materials and Methods

2.1. Systems Setup

Two on-grid identical PV systems (PV/PCM and reference PV) are installed at the Hashemite University, Jordan (lat. 32.1° N, long. 36.2° E). They are fixed systems sloped at 26° towards the south. Both systems are positioned on rooftop of the Presidency Building, as shown in Figure 1. A rooftop view of the Presidency Building and PV systems from Google Map is shown in Figure 2.



Figure 1. PV systems on the rooftop of the Presidency Building.



Figure 2. Google Map of Presidency Building and PV systems.

Each system consists of 14 Poly-Crystalline cell-type panels of 285 W rated capacity (SunTech, China). The total capacity of both systems is 7.98 kWp (DC) wired to a three-phase 8 kW inverter. The AC power is supplied to the university grid. The two systems are fitted with data acquisition systems to obtain system and weather data outputs, synchronously collected at a one-minute interval. The data is acquired using pyranometers to measure the total incident radiation on tilted planes, and type-k thermocouples to measure the ambient and cell temperatures. Also, voltage and current transducers are used to obtain the output DC voltage and current, respectively. The data is monitored directly over the internet by authorized persons and can be studied and analyzed offline.

The experimental data were collected over one full year from the 1st of August, 2015 up to the 31st of July, 2016. The collected data is analyzed, and the following parameters are determined for both systems on a daily, monthly, and yearly bases as discussed later:

1. Total incident solar radiation on a 26° tilted plane (kWh/m²)

2. PV modules DC electrical power output (kWh)
3. PV modules actual conversion efficiency (%)

2.2. Integration of PCM into PV panels

An Allen key was used to disassemble the 14 modules of the first system (PV/PCM) from their frames. The back surface of the panels and the outer surfaces of the PCM plastic envelopes were bonded together using Bison epoxy double syringes workable for 5 minutes (6305448), as shown in Figure 3. The surfaces to be bonded must be clean, dry, free of dust, and grease. Equal amounts of both components (resin and hardener) from the Bison epoxy were pressed out and mixed thoroughly in a mixing tray until an even color is obtained. A thin layer of about 1 mm thickness was then applied to the outer surface of the plastic envelopes, which contain the PCM. The parts to be bonded together were pressed using a square thin wooden block and kept in place for 20 minutes. Curing time is one hour approximately. A total of 57 double syringes was used in the bonding process. Finally, the PV panels were mounted back and tightened onto the frames. The 28 m² BioPCMTM mats used has the specifications tabulated in Table 1 [39].



Figure 3. Pasting PCM on the PV panels backside.

Table 1. Thermo-physical properties of BioPCMTM.

Parameter	Value
Model	M51/Q25
Melting point temperature	25 °C
Latent heat storage capacity	0.161 kWh/m ²
Unit thickness	15 mm
Product weight per m ²	3.76 kg

2.3. Methodology

2.3.1. Technical evaluation

The technical performance of the two PV systems are assessed using the following parameters:

1. Instantaneous DC power output (P_{DCout}) in Watts:

It is determined as by multiplying the measured DC voltage (V) by the measured DC current (I) and expressed as

$$P_{DCout} = V \times I \quad (1)$$

The instantaneous power values are utilized to determine the daily, monthly, and annual values in kWh, as discussed later in this work.

2. Conversion efficiency (η):

The operating efficiency obtained under real outdoor conditions is different from the one achieved in the laboratory under Standard Test Conditions (STC). The values of STC are solar irradiance of 1000 W/m², cell temperature of 25 °C, and air mass of 1.5 [42]. However, these conditions are rarely achieved in reality. The real operating efficiency of the PV modules is expressed as:

$$\eta = \frac{P_{DCout}}{n_p A_c I_d} \times 100 \quad (2)$$

where P_{DCout} is the DC power output in kWh of the PV modules, A_c is the area for each panel (=1.752 m²), and I_d is the measured total incident radiation on the tilted plane in kWh/m². In this work, n_p is the number of panels in each system (14). Monthly and annual values are determined to compare between the two PV systems.

2.3.2. Economic analysis

The economic analysis parameters utilized in this work are as follows [43]:

1. Payback Period (PBP):

Defined as the time taken to recover the cost of an initial investment from the annual savings it makes. The PBP is expressed as:

$$PBP = \frac{Investment}{Savings} \quad (3)$$

However, depending on a simple PBP calculation is not preferential, since it does not include other economic factors such as inflation, system depreciation, and maintenance overheads.

2. Net Present Value (NPV):

It is a measure of the difference between the present value of cash inflows and outflows over some time by discounting the flows at a specified rate. In our case, the discount rate is assumed to be 10%, as discussed later. A positive NPV indicates that the investment will be profitable while a negative NPV presents a business case with a net loss. The NPV metric is used to evaluate commercial and large-scale PV systems, and possibly some residential systems. The NPV is expressed as [43]:

$$NPV = -C_0 + \sum_{i=1}^T \frac{C_i}{(1+r)^i} \quad (4)$$

where C_0 is the initial investment, C_i is the annual balance net cash flow, r is the discount rate, and T is the lifespan of the project, which is taken as 20 years. This is dependent on the power purchase agreements (PPAs) signed between investors or independent power producers (IPPs) and Jordan's electricity company NEPCO [44].

3. Internal Rate of Return (IRR) [45]:

It represents the discount rate at which the project NPV is zero. This is a useful parameter for comparing the returns of different investments and choosing precisely between them.

If the IRR exceeds the discount rate r , then the investment is viable. It is expressed as:

$$NPV = 0 = -C_0 + \sum_{i=1}^T \frac{C_i}{(1+IRR)^i} \quad (5)$$

where C_0 is the initial investment, C_i is the annual balance net cash flow for the i^{th} year, and T is time (20 years) similar to the NPV calculations.

It should be noted that the IRR is an inferior metric for characterizing the value of solar systems in some cases. This

is due to the incentives and nature of financed costs, which could lead to an inflated misleading value [46].

3. Results and Discussion

3.1. Technical analysis

1. Solar irradiance

Solar irradiance measurements on the 26° tilted plane were recorded over a one-year testing period. They were analyzed to determine the daily solar irradiation, as shown in Figure 4. The peak value of 7.84 kWh/m² is reached on the 1st of July, while the minimum value of 0.87 kWh/m² is captured on the 25th of January. There are significant drops in winter due to cloudy and wintry weather conditions. The annual average daily irradiation is about 6.15 kWh/m².

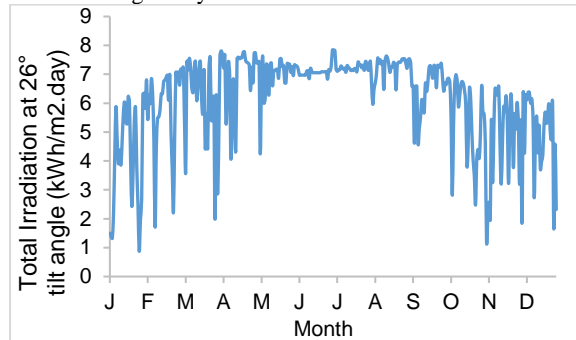


Figure 4. Daily irradiation on 26° tilted plane over a one-year testing period.

The daily values are added up to obtain the monthly irradiation illustrated in Figure 5. The maximum and minimum values received are 223.8 kWh/m² in July and 130.8 kWh/m² in January, respectively. The total annual irradiation is the sum of the monthly values, which is 2246.2 kWh/m². The monthly and annual irradiances are used to determine the conversion efficiencies.

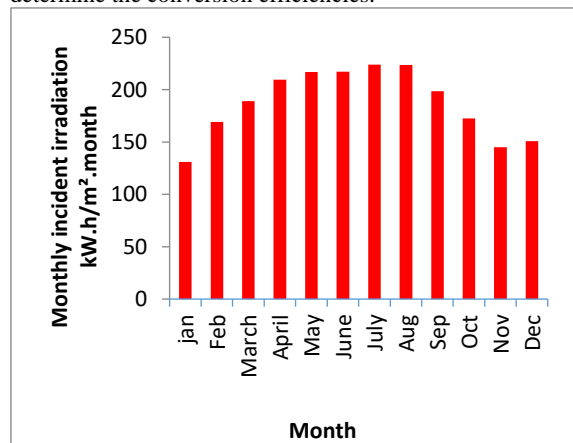


Figure 5. Monthly incident irradiation on a 26° tilted plane.

2. Actual power output

The instantaneous DC power output under actual operating conditions is determined from Equation (1) and presented in Figure 6 for a sample day (the 4th of September). The power curves are nearly symmetrical and typical for a clear day. The peak values obtained at 12:30 pm are 3089 W for the PV/PCM system, and 2806 W for the reference PV system.

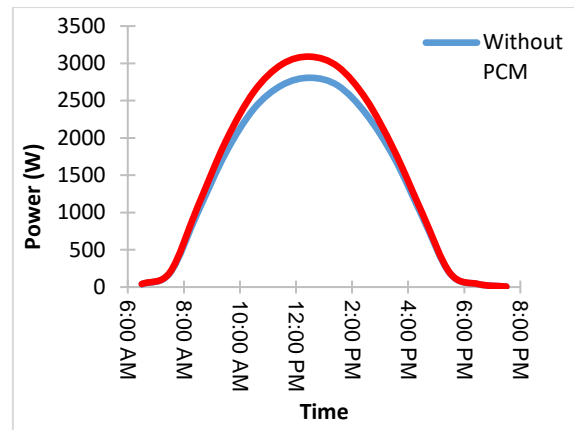


Figure 6. Instantaneous DC output power on the 4th of September.

This output is used to calculate the total daily yield power in kWh/day, as presented in Figure 7. There is a good match between the daily irradiation and power curves, as expected, with significant falls on cloudy days and little variations over the summer period.

The summation of the daily values produces the monthly yield power, as shown in Figure 8. It can be seen that there is no substantial difference in power output between the two systems from October till March due to the mild ambient and cell temperatures recorded. The PV systems operated below the STC temperature (25 °C) for the period from November to February, ranging from 16.4 °C to 23.8 °C. The results show that the benefit of PCM in cooling the modules at low temperatures is negligible. This is in agreement with literature in which it is reported that the PCM in general works better in warm and stable climatic conditions than the colder and variable conditions [47]. Smith et al. [48] found that the most considerable enhancement in performance was achieved in areas with high values of solar insolation and ambient temperatures all year-round, such as Africa, South Asia, Australia, and South America.

The yearly power output is obtained by adding up the monthly values. Under actual operating conditions, the yearly output of the PV/PCM system is 6879.2 kWh by comparison with 6654.7 kWh for the one without PCM. Hence, the increase in power production is about 3.4% due to the application of PCM.

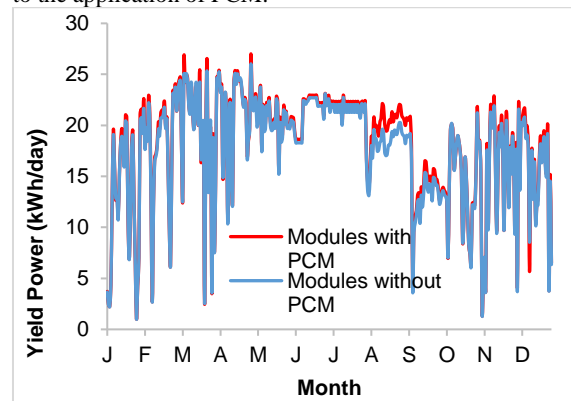


Figure 7. Daily yield power of the two PV systems.

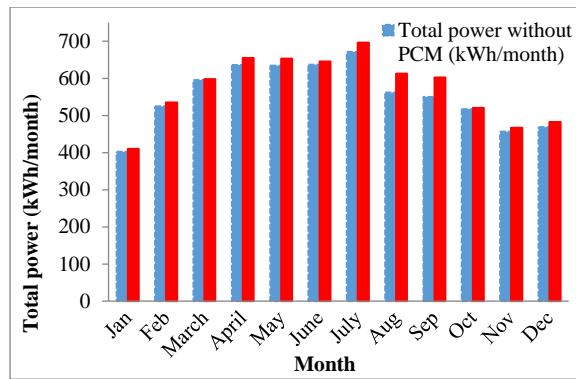


Figure 8. Monthly yield power of the systems with and without PCM.

3. Conversion efficiency (η)

The monthly average conversion efficiencies of the two PV systems are determined using Equation (2) and shown in Figure 9. The maximum monthly efficiencies obtained are 13.2% in November for the PV-PCM system and 12.9% in March for the reference system. It can be seen that the maximum efficiencies occur from November to March due to the low ambient temperatures experienced in these months. Another contributing factor can be attributed to the minimal dust build-up because of the repeated rainfall in this period. A recent study in Jordan [49] found that the efficiency decreases because of dust are 0.768%/day and 0.607%/day based on two different models. The minimum efficiencies occur in August for both systems, with 11.2% for the PV-PCM system and 10.2%, for the reference system. This is expected mainly due to the high ambient temperatures and considerable dust accumulation.

The annual conversion efficiency is an essential parameter in the technical comparison between the two systems. It is determined as 12.50% for the PV-PCM system, while it is 12.08% for the reference PV system. There is an improvement of about 3.48% due to the employment of PCM.

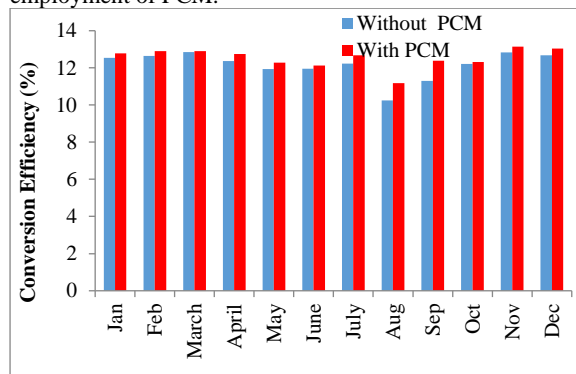


Figure 9. Monthly average conversion efficiencies of the two PV systems.

3.2. Economic analysis

1. Basic assumptions

The economic study is carried out in the local currency (Jordanian Dinar JD). Every 1 US\$ is equal to 0.708 JD. The economic metrics used and cost assumptions made to perform this economic study are as follows:

1. The electricity tariff for the Hashemite University in 2016 is 0.256 JD/kWh, including additional charges [44].
2. Based on electricity costs in Jordan between 2005-2013 [50], the annual tariff increment is assumed to be 5%.
3. The operating and maintenance costs (*OMCs*) are assumed to be approximately 14 JD/kWp/year for each PV system [51]. The total *OMCs* add up to around 56 JD with an annual inflation rate of 3%.
4. The average value for the interest rate on bank credit to the private sector in Jordan is around $9 \pm 0.2\%$ for the period 2008-2012 [52]. Hence, an upper limit for the discount rate r is assumed to be 10% in this study.
5. The PV modules' annual output power is reduced linearly from the nominal power output based on the 25-year transferrable power output warranty [53].

Also, the actual cost and quantity of PCM mats and epoxy purchased to conduct the tests are presented in Table 2.

Table 2. Cost and quantity of purchased PCM and epoxy.

Item	Description	Origin	Quantity	Total Price (JD)
1	BioPCM™ M51 Q25	USA	28 m ²	735
2	Bison Epoxy 6305446	Holland	57 syringes	178
				913

2. Yearly balance cash flows

Based on the assumptions presented above, the *OMCs* for the next 20 years is determined by:

$$OMCs = 56 \times (1.03)^{Y-1} \quad (6)$$

Similarly, the annual electricity tariff rate TR is calculated as follows:

$$TR = 0.266 \times (1.05)^{Y-1} \quad (7)$$

where Y is the year number.

Throughout our study, the PV/PCM system generated 6879.2 kWh/yr, whereas the system without PCM generated actual power of 6654.7 kWh/yr. The annual power production (*APP*) of each system is projected for the next 20 years using the reduction percentage values derived from the manufacturer's brochure.

The cash flow resulting from Annual Sold Energy (*ASE*) is determined by multiplying the annual power production (*APP*) by the tariff rate (TR) as follows:

$$ASE = APP \times TR \quad (8)$$

By combining the cash flows for the capital cost C_0 , *OMCs*, and *ASE*, the annual balance cash flow for the PV system using PCM is presented in Figure 10. Similarly, the annual balance cash flow for the PV system without PCM is shown in Figure 11. This is obtained by adding the cash flows for *OMCs* and *ASE* with no initial investment. The annual balance net cash flow C_i is the difference between the cash flows presented in Figures 10 and 11. This net balance is shown in Figure 12.

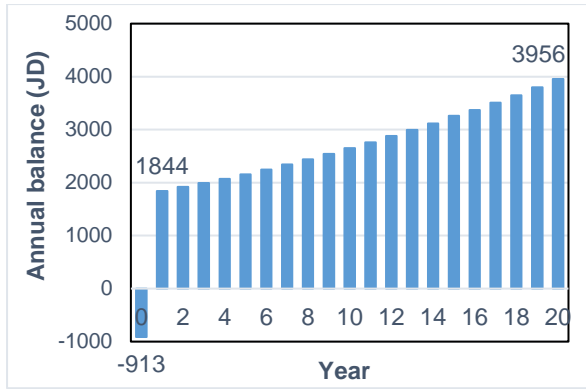


Figure 10. The annual balance cash flow for the PV system using PCM.

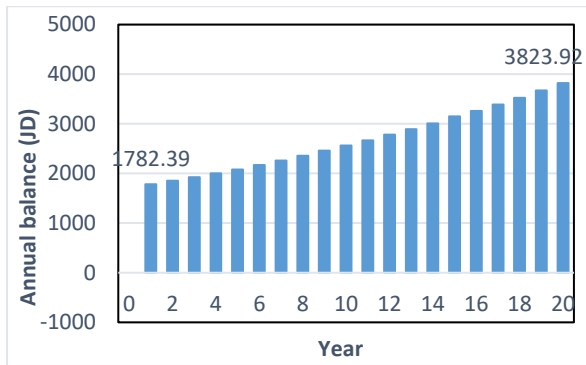


Figure 11. Annual balance cash flow for the PV system without PCM.

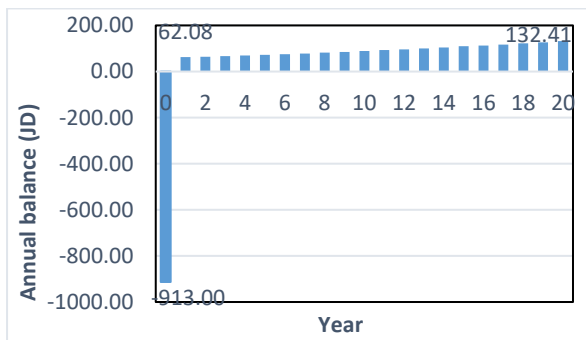


Figure 12. Annual balance cash flow for the net difference between the two systems.

3. Payback Period (PBP)

The initial PCM investment is calculated as 913 JD, as shown in Table 2. From the net cash flows in Figure 12, the savings achieved by using the PV system with PCM is 838.70 JD for the first eleven years. Hence,

$$PBP = 11 + \frac{913 - 838.70}{100.41} = 11.74 \text{ years}$$

= 11 years and 9 months

where 100.41 JD is the savings achieved in the 12th year.

4. Net Present Value (NPV)

The NPV is determined by using spreadsheets based on Equation (4), and net cash flows C_i in Figure 12. It is found that:

$$NPV = -913 + \sum_{i=1}^{20} \frac{C_i}{(1 + 0.10)^i} = -212.41 \text{ JD}$$

Net present value is negative, which implies that the PCM investment is not profitable and will result in a net loss.

5. Internal Rate of Return (IRR)

Similarly, the IRR is determined by using an Excel spreadsheet based on Equation (5) and net cash flows. It is found that $IRR = 6.87\%$, which is less than the discount rate of 10%. This indicates that the PCM investment is not economically attractive based on the IRR metric.

4. Conclusions

This study presented a technical-economic investigation of the enhancement of PV power production utilizing the PCM passive cooling means. Two identical 3.99 kWp PV/PCM and reference PV systems were installed and tested year-round at the Hashemite University, Jordan.

Technical analysis shows that the annual output of the PV/PCM system is 6879.2 kWh by comparison with 6654.7 kWh for the reference PV system. Hence, the modest increase in power generated is about 3.4% due to the application of BioPCM. Also, the monthly yield power indicates that there is no considerable difference in power output between the two systems from October till March due to the mild ambient and cell temperatures recorded. The PV systems operated below the STC temperature (25 °C) for this fraction of the year. It can be concluded that the benefit of PCM in cooling the modules at low temperatures is negligible.

The brief economic study carried out in this work does not currently support the application of PCM in Jordan and countries of similar climates. The analysis reveals that the payback period for the PCM investment is 11.74 years. The net present value NPV is negative, and the internal rate of return IRR is 6.87%, which is less than the discount rate. The feasibility of the PV/BioPCM system will vary if PCM is purchased in much larger quantities or if it was manufactured locally. Other economic metrics that might positively affect the financial viability of this investment include falling discount rate, rising electricity tariff, and longer operating lifespan (dependent on the agreement between investors and National Electricity power Company NEPCO). The current trends of these metrics are in favor of the PCM investment in the future.

Funding

This research was funded by the Deanship of Scientific Research, the Hashemite University, Jordan.

Acknowledgments

The work is dedicated to the memory of the late Prof. Ahmad Al-Ghandour, who was recognized as a pioneer in the field of renewable energy in Jordan and the region. He has inspired, mentored, and lead a generation of researchers and students in different fields.

Conflicts of Interest

The authors declare no conflict of interest.

References

- Population of the Kingdom by Sex According to the 1952, 1961, 1979, 1994, 2015 and 2018 Censuses, and Estimated Population for Some Selected Years; Department of Statistics, Ministry of Planning, Jordan: Amman, Jordan, 2019.
- Energy 2019 - Facts and Figures; Ministry of Energy and Mineral Resources: Amman, Jordan, 2019.
- Alwashdeh, S.S.; FMA, M.A.S. Solar radiation map of Jordan governorates. *International Journal of Engineering & Technology* **2018**, *7*, 1664-1667.
- Abu-Rumman, G.; Khair, A.I.; Khair, S.I. Current status and future investment potential in renewable energy in Jordan: An overview. *Heliyon* **2020**, *6*, e03346.
- Jordan Renewable Energy & Energy Efficiency (Law No. 13). 2012.
- Annual Report 2018; National Electric Power Company (NEPCO): Amman, Jordan, 2019.
- Renewable Energy Projects in Jordan, May 2020. Ministry of Energy and Mineral Resources (MEMR), The Hashemite Kingdom of Jordan: Amman, Jordan, 2020.
- Marrar, Y. Renewable Energy Program in Jordan; Ministry of Energy and Mineral Resources (MEMR), The Hashemite Kingdom of Jordan: Amman, Jordan, 2019.
- Furkan, D.; Mehmet Emin, M. Critical factors that affecting efficiency of solar cells. *smart grid and renewable energy* **2010**, 2010.
- Dash, P.; Gupta, N. Effect of temperature on power output from different commercially available photovoltaic modules. *International Journal of Engineering Research and Applications* **2015**, *5*, 148-151.
- Virtuani, A.; Pavanello, D.; Friesen, G. Overview of temperature coefficients of different thin film photovoltaic technologies. In *Proceedings of 25th European photovoltaic solar energy conference and exhibition/5th World conference on photovoltaic energy conversion*; pp. 6-10.
- Alwashdeh, S.S. Comparison among Solar Panel Arrays Production with a Different Operating Temperatures in Amman-Jordan. *International Journal of Mechanical Engineering and Technology* **2018**, *9*, 420-429.
- Sharma, R.; Gupta, A.; Nandan, G.; Dwivedi, G.; Kumar, S. Life span and overall performance enhancement of solar photovoltaic cell using water as coolant: a recent review. *Materials Today: Proceedings* **2018**, *5*, 18202-18210.
- Amalu, E.H.; Hughes, D.J.; Nabhani, F.; Winter, J. Thermo-mechanical deformation degradation of crystalline silicon photovoltaic (c-Si PV) module in operation. *Engineering Failure Analysis* **2018**, *84*, 229-246.
- Boussaid, M.; Belghachi, A.; Agroui, K.; Abdelaoui, M.; Otmani, M. Solar cell degradation under open circuit condition in out-doors-in desert region. *Results in physics* **2016**, *6*, 837-842.
- Boussaid, M.; Belghachi, A.; Agroui, K.; Djarfour, N. Mathematical models of photovoltaic modules degradation in desert environment. *AIMS Energy* **2019**, *7*, 127-140.
- Hasan, A.; McCormack, S.J.; Huang, M.J.; Norton, B. Energy and cost saving of a photovoltaic-phase change materials (PV-PCM) system through temperature regulation and performance enhancement of photovoltaics. *Energies* **2014**, *7*, 1318-1331.
- Hasan, I.A. Enhancement the Performance of PV Panel by Using Fins as Heat Sink. *Engineering and Technology Journal* **2018**, *36*, 798-805.
- Du, D.; Darkwa, J.; Kokogiannakis, G. Thermal management systems for photovoltaics (PV) installations: a critical review. *Solar Energy* **2013**, *97*, 238-254.
- Chandel, S.; Agarwal, T. Review of cooling techniques using phase change materials for enhancing efficiency of photovoltaic power systems. *Renewable and Sustainable Energy Reviews* **2017**, *73*, 1342-1351.
- Amelia, A.; Irwan, Y.; Irwanto, M.; Leow, W.; Gomesh, N.; Safwati, I.; Anuar, M. Cooling on photovoltaic panel using forced air convection induced by DC fan. *International Journal of Electrical and Computer Engineering* **2016**, *6*, 526.
- Odeh, S.; Behnia, M. Improving photovoltaic module efficiency using water cooling. *Heat Transfer Engineering* **2009**, *30*, 499-505.
- Irwan, Y.; Leow, W.; Irwanto, M.; Amelia, A.; Gomesh, N.; Safwati, I. Indoor test performance of pv panel through water cooling method. *Energy Procedia* **2015**, *79*, 604-611.
- Bahaidarah, H.; Subhan, A.; Gandhidasan, P.; Rehman, S. Performance evaluation of a PV (photovoltaic) module by back surface water cooling for hot climatic conditions. *Energy* **2013**, *59*, 445-453.
- Grubišić-Čabo, F.; Nižetić, S.; Giuseppe Marco, T. Photovoltaic panels: A review of the cooling techniques. *Transactions of FAMENA* **2016**, *40*, 63-74.
- Hussien, H.A.; Noman, A.H.; Abdulmunem, A.R. Indoor investigation for improving the hybrid photovoltaic/thermal system performance using nanofluid (Al₂O₃-water). *Engineering and Technology Journal* **2015**, *33*, 889-901.
- Ebaid, M.S.; Ghrair, A.M.; Al-Busoul, M. Experimental investigation of cooling photovoltaic (PV) panels using (TiO₂) nanofluid in water-polyethylene glycol mixture and (Al₂O₃) nanofluid in water-cetyltrimethylammonium bromide mixture. *Energy Conversion and Management* **2018**, *155*, 324-343.
- Habeeb L., Mutasher D., Abd Ali F. Solar panel cooling and water heating with an economical model using thermosyphon. *Jordan Journal of Mechanical and Industrial Engineering* **2018**, *12*, 3, 189 -196.
- Socaciu, L.; PLEȘA, A.; UNGUREȘAN, P.; Giurgiu, O. Review on phase change materials for building applications. *Leonardo Electronic Journal of Practices and Technologies* **2014**, *25*, 179-194.
- Chandel, S.; Agarwal, T. Review of current state of research on energy storage, toxicity, health hazards and commercialization of phase changing materials. *Renewable and Sustainable Energy Reviews* **2017**, *67*, 581-596.
- Kiwan, S.; Ahmad, H.; Alkhalidi, A.; Wahib, W.O.; Al-Kouz, W. Photovoltaic Cooling Utilizing Phase Change Materials. In *Proceedings of E3S Web of Conferences*; p. 02004.
- Stritih, U. Increasing the efficiency of PV panel with the use of PCM. *Renewable Energy* **2016**, *97*, 671-679.
- Soares, N.; Costa, J.; Gaspar, A.; Matias, T.; Simões, P.N.; Durães, L. Can movable PCM-filled TES units be used to improve the performance of PV panels? Overview and experimental case-study. *Energy and Buildings* **2020**, *210*, 109743.
- Nada, S.; El-Nagar, D. Possibility of using PCMs in temperature control and performance enhancements of free stand and building integrated PV modules. *Renewable energy* **2018**, *127*, 630-641.
- Singh, P.; Khanna, S.; Newar, S.; Sharma, V.; Reddy, K.S.; Mallick, T.K.; Becerra, V.; Radulovic, J.; Hutchinson, D.; Khusainov, R. Solar Photovoltaic Panels with Finned Phase Change Material Heat Sinks. *Energies* **2020**, *13*, 2558.
- Khaled, M.; Hachem, F.; El-Rab, G.; Ramadan, M. Cooling photovoltaic cells using phase change materials—Experiments and economical study. *ERJ. Engineering Research Journal* **2017**, *40*, 25-29.
- Ancı, M.; Bilgin, F.; Nižetić, S.; Papadopoulos, A.M. Phase change material based cooling of photovoltaic panel: a simplified numerical model for the optimization of the phase change material layer and general economic evaluation. *Journal of Cleaner Production* **2018**, *189*, 738-745.

38. Berardi, U.; Manca, M. The energy saving and indoor comfort improvements with latent thermal energy storage in building retrofits in Canada. *Energy Procedia* **2017**, 111, 462-471.
39. BioPCMat. Australia, P.C.E.S., Ed. Phase Change Energy Solutions Australia: Mitcham, Australia, 2015.
40. Lassandro, P.; Di Turi, S. Energy efficiency and resilience against increasing temperatures in summer: the use of PCM and cool materials in buildings. *International Journal of Heat and Technology* **2017**, 35, S307-315.
41. Gassar, A.A.A.; Yun, G.Y. Energy saving potential of PCMs in buildings under future climate conditions. *Applied Sciences* **2017**, 7, 1219.
42. Gupta, A.; Kumar, P.; Pachauri, R.; Chauhan, Y.K. Effect of Environmental Conditions on Single and Double Diode PV system: Comparative Study. *International Journal of Renewable Energy Research (IJRER)* **2014**, 4, 849-858.
43. Blank, L.T.; Tarquin, A.J. Basics of engineering economy/Leland Blank, Anthony Tarquin; Boston: McGraw-Hill Higher-Education: 2008.
44. Hammad, B.; Al-Sardeah, A.; Al-Abed, M.; Nijmeh, S.; Al-Ghandoor, A. Performance and economic comparison of fixed and tracking photovoltaic systems in Jordan. *Renewable and Sustainable energy reviews* **2017**, 80, 827-839.
45. Rahman, M.A.; Kholilullah, M.I. Use of solar panel at rural areas in Bangladesh: Impacts, financial viability and future prospects. *International Journal of Science and Research* **2017**, 6, 398-404.
46. Drury, E.; Denholm, P.; Margolis, R. Impact of Different Economic Performance Metrics on the Perceived Value of Solar Photovoltaics; National Renewable Energy Lab.(NREL), Golden, CO (United States): 2011.
47. Hasan, A.; McCormack, S.; Huang, M.; Sarwar, J.; Norton, B. Increased photovoltaic performance through temperature regulation by phase change materials: Materials comparison in different climates. *Solar Energy* **2015**, 115, 264-276.
48. Smith, C.J.; Forster, P.M.; Crook, R. Global analysis of photovoltaic energy output enhanced by phase change material cooling. *Applied energy* **2014**, 126, 21-28.
49. Hammad, B.; Al-Abed, M.; Al-Ghandoor, A.; Al-Sardeah, A.; Al-Bashir, A. Modeling and analysis of dust and temperature effects on photovoltaic systems' performance and optimal cleaning frequency: Jordan case study. *Renewable and Sustainable Energy Reviews* **2018**, 82, 2218-2234.
50. Komendantova, N.; Irshaid, J.; Marashdeh, L.; Al-Salaymeh, A.; Ekenberg, L.; Linnerooth-Bayer, J. Country Fact Sheet Jordan: Energy and Development at a Glance 2017: Background Paper. MENA-SELECT Working Paper **2017**.
51. Salasovich J, G.J., Mosey G, Healey V. Feasibility Study of Economics and Performance of Solar Photovoltaics at the Kolthoff Landfill in Cleveland, Ohio. A Study Prepared in Partnership with the Environmental Protection Agency for the RE-Powering America's Land Initiative: Siting Renewable Energy on Potentially Contaminated Land and Mine Sites; No. NREL/TP-7A40-58760; National Renewable Energy Lab (NREL): Golden, CO, USA, 2013.
52. Rajha, K.S. Determinants of non-performing loans: Evidence from the Jordanian banking sector. *Journal of Finance and Bank Management* **2016**, 4, 125-136.
53. Suntech STP285 - 24/Vd. Suntech, Ed. Suntech: 2011.

Development of A New Technique for Modeling and Optimizing Manufacturing Errors for Cn Machine Tools

Messaoud Farouk^a, Rahou Mohamed^{b,*}, Sebaa Fethi^a

^aLaboratoire d'Ingénierie des systèmes mécaniques et matériaux, Department of Mechanical Engineering, University of Technology, Tlemcen BP 230 - 13000 Tlemcen, Algeria.

^bDepartment of Mechanical Engineering, Higher school of applied sciences of Tlemcen, BP 165 RP Bel Horizon, 13000 Tlemcen, Algeria.

Received December 24 2019

Accepted October 31 2020

Abstract

This paper presents a new technique for optimizing manufacturing tolerances. This technique is based on the combination of two methods, the goal programming method and the genetic algorithm. Firstly, cubic splines interpolation is used to describe machining errors by a set of cubic polynomials. Tool path error, table motion error and tool wear error are considered in this study. Then, based on the goal programming method, the optimization problem is established. In order to avoid weighting effects in the objective functions, we used a genetic Non-dominated Sorting Genetic Algorithm (NSGA) for the resolution of the objective programming problems. A description of optimization processes based on NSGA is presented, and some of the genetic operators are explained. As a result, zero percent rejection of machining parts are obtained by this method. In this study, only three type of machining errors are considered.

© 2020 Jordan Journal of Mechanical and Industrial Engineering. All rights reserved

Keywords: Manufacturing tolerances, Goal programming, Machining errors, Cubic spline interpolation, Genetic algorithm;

1. Introduction

Currently, Multi-axis machine tools are used in various fields of advanced manufacturing, for instance the aerospace, the military, the automobile manufacturing and other fields. Improving the tools' machining precision is one of the major significant pursuits for industry manufactures. Machining errors are investigated and divided into two categories, systematic and random errors. Then, the compensation method is performed by tool path modification [1]. However, only systematic errors are compensated in this study. Systematic errors are determined [2] based on three stage experimental study. A new methodology for error compensation of free-form surface is offered [3]. The machined surface is obtained under the base of the T-spline surface reconstruction, using the online inspection data. Using mirror symmetry model, a compensate surface is constructed and used in the CAM process for error compensation. However, the impact of sampling point's distributions on the machining precision are not showed. By using an adaptive neuro-fuzzy inference system and a neural network system, an intelligent system for machine condition monitoring is developed [4].

Thermal errors can have significant effects on CNC machine tool accuracy. The errors come from thermal deformations of the machine elements affected by heat sources within the machine structure or from ambient temperature change [5]. A test piece is considered in order to evaluate thermal errors of five axis machine tools. Also, the R-Test measurement system is used in order to inspect

the thermal comportment of the machine tools which were used in thermal test piece machining [6]. However, the R-Test measurement instruments require experienced operators to avoid collusion. In [7] a review of all experimental techniques used for temperature measurement of machine tools and workpiece, a novel approach for an adaptive learning control for thermal error estimation and compensation for 5-axis machine tools was adopted [8]. The sources of thermal error are presented and discussed, then the temperature monitoring technology and thermal deformation monitoring technology are presented. Finally, a new measurement technology called the "fiber bragg grating distributed sensing technology" is introduced for heavy-duty CNC machine tools. A technique has been developed for the error's compensation under temperature stress on five-axis machine tools [9].

Tool error is an important factor that affects the quality and tolerance of machined parts. Tool errors are classified into static and dynamic errors, then error identification method based on shape mapping are presented [10]; a new prediction model of tool errors is developed based on back propagation neural network and genetic algorithm. Based on tool error parameters, the machining error are determined by using the prediction model, then by adjusting the NC code, the tool errors compensation method is carried out. However, machine tool errors and lubrication effect are not considered. A novel technique to estimate the volumetric accuracy of five axis machine tools is presented [11]. A spherical deviation measurement method based on double ball-bar is proposed. An adaptive machining approach by using measured free form deformation data is developed [12]. Template tool positions are revised based

* Corresponding author e-mail: am_rahou@yahoo.fr.

on information from the real part geometry. A Bezier surface is used to project the novel tool positions. However, this approach can be more improved by taken into account cutting forces. In order to minimize tool deflection errors, genetic algorithm is used to determine the optimized machining parameters [13]. Tool wear monitoring technique in real time is presented in [14] based on ultrasonic system and adaptive neuro-fuzzy inference system.

Many sources of errors contribute in the tool path deviation, kinematic and geometric errors contribute with large amount of deviations [15]. A new technique for three axis machine tools kinematic errors identification is proposed, by conducting a series of machining test in order to separate geometric errors from profile errors [16]. In order to identify geometric errors on three axis machine tools, thermo-invariant multi-features bar (MFB) is designed and developed [17]. A kinematic model for a 5-axis machine tool is built in order to identify geometric error and setup position error, the methodology to calculate these errors is presented [18]. Geometric errors of the two rotary axes are identified and compensated in [19] by adopting an artifact as the test piece and touch-trigger probe for indirect measurement. A new error compensation model is developed based on tool path modification. However; we notice deviation between the predicted and the measured error, this study can be more enhanced by considering other source errors, such as thermo-mechanical error. Adopting differential motion matrix, a new model to identify position independent geometric errors is built in [20]. A geometric errors compensation method for large five axis machine tools is presented. A laser tracker is used for the machine tool tip position measurement; then two position-dependent geometric error models of a machine tool are constructed based on tool tip measurement. Optimal machine tool compensation tables are generated for each model [21]. An efficient geometric errors identification method for non-orthogonal five axis machine tools is considered for the coupling relationship of the error parameters [22].

2. Modeling of machining errors using cubic spline

Modeling machining errors or any large data set can be a very challenging task. Generally, the higher the order of polynomial is, the more accurate it is. However; the computation operations on polynomials of high degree involve certain problems, it is suitable to use polynomials of low degree. In order to achieve the higher accuracy and minimize the complexity of computation operations, cubic spline is proposed in this paper for machining errors modeling instead of polynomials interpolation.

A spline is a set of polynomials of degree k that are smoothly connected at certain data points. At each data point, two polynomials connect, and their first derivatives (tangent vectors) have the same values. The definition also requires that all their derivatives up to the $(k - 1)$ st be the same at the point [23].

For data set of N points; cubic spline $S_k(x)$ in $[x_k, x_{k+1}]$ with $k = 0, \dots, N - 1$. Are defined with the following steps:

$$\begin{aligned} S_k(x_k) &= y_k \\ S_k(x_{k+1}) &= y_{k+1} \\ S'_k(x_k) &= S'_{k-1}(x_k) \\ S'_k(x_{k+1}) &= S'_{k+1}(x_{k+1}) \\ S''_k(x_k) &= S''_{k-1}(x_k) \\ S''_k(x_{k+1}) &= S''_{k+1}(x_{k+1}) \end{aligned} \quad (1)$$

In this work, path errors, tool wear and table movement errors are modeled by the cubic spline method. The data set used in this study is taken from Ph.D. thesis of (Rahou, 2010) [24] which include these error measurements. Evaluation between cubic spline and Polynomials interpolation is also presented to show the advantages of modeling by cubic spline in this section.

2.1. Tool path error modeling

Figure (1) represents the cutting tool path errors. The cubic spline $f_1(x)$ is composed of a set of 24 cubic polynomials smoothly connected

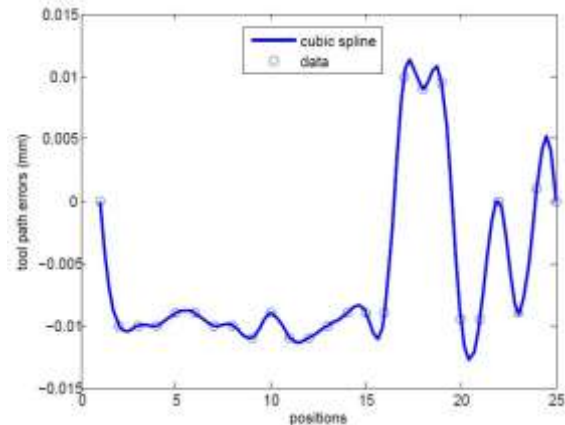


Figure 1. Cutting tool path error curve

$$f_1(x) = \begin{cases} S_0 & 0 \leq x \leq 1 \\ S_1 & 1 \leq x \leq 2 \\ \vdots & \vdots \\ S_{24} & 24 \leq x \leq 25 \end{cases} \quad (2)$$

2.2. Table motion errors

Figure (2) represents the table motion errors. The cubic spline $f_2(x)$ of table motion errors is a set of 24 cubic equations

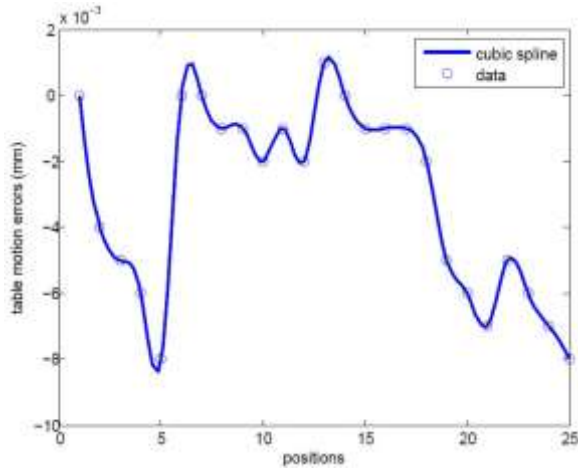


Figure 2. Table motion errors curve

$$f_2(x) = \begin{cases} S_0 & 0 \leq x \leq 1 \\ S_1 & 1 \leq x \leq 2 \\ \vdots & \\ S_{24} & 24 \leq x \leq 25 \end{cases} \quad (3)$$

2.3. Tool wear error modeling

As we can see in Figure (3), cubic spline curve and linear curve are the same, so it is more practical to work with the linear curve rather than the cubic spline curve, especially if we know that the spline curve is composed from 39 cubic polynomials.

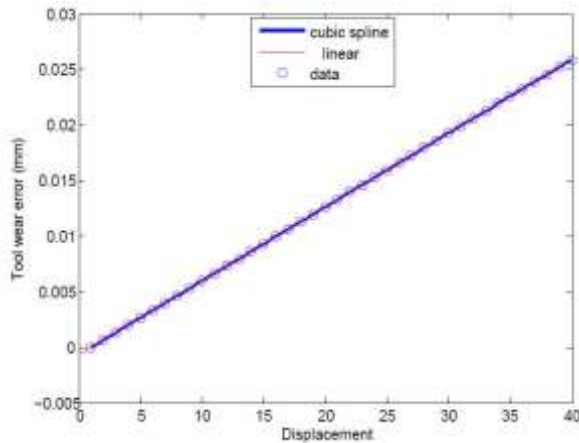


Figure 3. Tool wear error curve

Tool wear error is given by the linear equation (3)

$$f_3(x) = 0.00066 * x - 0.0006 \quad (4)$$

As we can see in fig (1) and fig (2) with data set of 25 points, using polynomials interpolation (for instance Lagrange polynomial) will produce a polynomial of 24 degree, contrary to cubic spline interpolation which produced a set of cubic polynomials smoothly connected. The highest precision is achieved, with low degree polynomials.

Manufacturing errors are given above by mathematical equations. In this paper, an investigation is presented, by seeking the optimum amount of each manufacturing error so, the sum of these manufacturing errors does not exceed the tolerance design equation. 5.

$$\sum_1^3 f_i(x) \leq IT \quad (5)$$

This technique will not only guarantee the conformity of all the machined parts; but can be used for errors prediction.

Goal programming is used to establish the problem, then based on genetic algorithm, the problems is solved.

3. Goal Programming problem formulation

Based on goal programming, a nonlinear programming problem is established. Then, a minimization of the weighted sum of deviations from the goals was carried out.

$$\begin{cases} \text{Minimize } \sum_{i=1}^P |f_i(x) - g_i| \\ C(x) \leq c \text{ (constraints)} \end{cases} \quad (6)$$

$f_i(x)$: Objective functions
 g_i : The goal set for the i-th goal (for $i = 1, 2, \dots, p$);
 $C(x)$: Manufacturing tolerance interval
 c : Design tolerance interval

By introducing the negative and positive deviations N_i and P_i respectively. The system (6) can be written as:

$$\begin{aligned} \min Z &= \sum_{i=1}^P (w_i * N_i + w_i * P_i) \\ \text{Subject to} & \end{aligned} \quad (7)$$

$$\begin{cases} \sum_{i=1}^P a_{ij}x_j - P_i + N_i = g_i \text{ for each goal } i \quad (i = 1,2, \dots, p) \\ x_j \geq 0 \text{ (for } j = 1,2, \dots, n) \\ P_i \times N_i = 0 \text{ (for } i = 1,2, \dots, n) \\ P_i \geq 0, N_i \geq 0 \end{cases}$$

In our case, positive deviations are minimized in order not to violate the tolerance interval. Which lead us to rewrite the equation (5) to the next system

$$\begin{aligned} \min \sum_1^4 w_i P_i \\ \text{Subject to} \\ f_1(x) - P_1 = IT \\ f_2(x) - P_2 = IT \\ f_3(x) - P_3 = IT \\ \sum_1^3 f_i(x) - P_4 = IT \\ P_i \geq 0 \end{aligned} \quad (8)$$

Where

w_i is the weight factors fixed by the user which represents the goals preference and the sum equal to one.

N_i and P_i are the negative and the positives deviations from the goal respectively.

IT is the tolerance interval

Note that in the system (8), the negative deviations N_i in the constraints are eliminated by using a (\leq) relation.

4. Non-dominated sorting genetic algorithm

The selection operation is the only difference between the non-dominated sorting genetic algorithm (NSGA) and simple genetic algorithm. The crossover operator and

mutation operator work the same way. NSGA used in this study is a real parameters GA.

Classifying the population into P_k classes based on non-domination is the first stage of NSGA.

$$P = \bigcup_{k=1}^n P_k \quad (9)$$

n : The total number of fronts

4.1. Non-dominated sorting of a population:

Considering a population P of N solutions, the following procedure could be used to deduce the classes non-dominated of solutions:

- Step 0: set all non-dominated sets $P_k = \emptyset$; ($k=1, 2, \dots$). For non-domination level $k = 1$
- Step 1: set counter solution $i = 1$, $P' = \emptyset$.
- Step 2: for a solution $j \in P$ ($j \neq i$). If solution j dominate solution i , go to step 4.
- Step 3: Increase j and go to step 2. Otherwise set $P' = P' \cup \{i\}$
- Step 4: increment i . If $i \leq N$ go to step 2. Otherwise stop and declare P' as the non-dominated set.
- Step 5: update $P_k = P'$ and $P = P/P'$
- Step 6: if $P \neq \emptyset$; increment k and go to Stage1. If not, stop and announce all non-dominated sets P_k

This procedure can handle any numbers of objectives, maximization or minimization problems can be treated. The next step is to assign a value for each solution of these classes.

4.2. Sharing method

For a given front k , which contain n_k solutions; each have a fitness value equal to f_k , the sharing method is explained as follow:

Firstly, the sharing functions value is calculated by using the following function [25]

$$Sh(d_{ij}) = \begin{cases} 1 - \left(\frac{d_{ij}}{\sigma_{share}}\right)^2, & \text{if } d_{ij} \leq \sigma_{share} \\ 0; & \text{otherwise} \end{cases} \quad (10)$$

The parameter d_{ij} is the Euclidian distance between any two solutions in the populations in the same front. d_{ij} is determined as follows:

$$d_{ij} = \sqrt{\sum_{p=1}^P \left(\frac{x_k^i - x_k^j}{x_k^{max} - x_k^{min}}\right)^2} \quad (11)$$

P : The problem variables. Then, a niche count ηc_i is calculated for the i -th solution as follows:

$$\eta c_i = \sum_{j=1}^N Sh(d_{ij}) \quad (12)$$

The final step is to calculate the shared fitness value as follows

$$f'_i = f_i / \eta c_i \quad (13)$$

The minimum shared fitness in this class is noted $f'_k{}^{min}$. In order to proceed the next non-dominated class, the assigned fitness value is equal to:

$$f_{k+1} = f'_k{}^{min} - \epsilon \quad (14)$$

ϵ : is small positive number.

4.3. reproduction operator

Making several copies of good solutions and removing bad solutions from the population is the main goal of the selection operator while keeping population size constant, Based on the dummy fitness value and stochastic remainder proportionate selection.

4.4. Crossover and mutation operators:

As mentioned above, selection operator cannot produce any new solutions, it only duplicate good solutions at the expense of bad solutions. Crossover and mutation operators are responsible to create new solutions.

For crossover operation, two solutions are picked (called parent solutions) from the mating pool at random and crossed with a probability $p_c = 0.9$. in this study simulated binary crossover (SBX) operator is used. The procedure of computing children solutions x_1 and x_2 from the parent solutions y_1 and y_2 is described below [25]:

Step 1: choose a random number $u \in [0; 1]$

Step 2: calculate β_{qi} using the next equation:

$$\beta_{qi} = \begin{cases} (2u_i)^{\frac{1}{\eta_c+1}}; & \text{if } u_i \leq 0.5 \\ \left(\frac{1}{2(1-u_i)}\right)^{\frac{1}{\eta_c+1}}; & \text{otherwise} \end{cases} \quad (15)$$

η_c : distribution index. In this study, η_c is fixed 20.

Step 3: the children solutions are created using the following equations

$$x_1 = 0.5[(1 + \beta_{qi})y_1 + (1 - \beta_{qi})y_2] \quad (16)$$

$$x_2 = 0.5[(1 - \beta_{qi})y_1 + (1 + \beta_{qi})y_2] \quad (17)$$

Using the above step by step, the children solutions are created. Note that the two children solutions are symmetric about the parent solutions.

Polynomial mutation [25] is used in this study to create a new solution z_i from the parent solution x_i ; the following step by step is used for a mutation probability $p_m = 0.1$:

Step 1: create a random number $u \in [0; 1]$

Step 2: calculate the parameters δ_i as follows:

$$\delta_i = \begin{cases} (2u_i)^{\frac{1}{\eta_m+1}} - 1 & \text{if } u_i < 0.5 \\ 1 - \left[2(1-u_i)^{\frac{1}{\eta_m+1}} - 1\right] & \text{if } u_i \geq 0.5 \end{cases} \quad (18)$$

η_m : distribution index for mutation. $\eta_m = 150$ is fixed in this study.

Step 3: calculate Z_i by the relation (19):

$$z_i = x_i + \delta_i(x_i^u - x_i^l) \quad (19)$$

x_i^u and x_i^l Are the superior and inferior bounds of parameter x_i .

5. Problem description and optimization problem

In this paper, the above multi objective GA is used in order to solve goal programming problem in system 8, however some changes are needed for this purpose.

Minimizing the positive deviations P_i in system 8, with $P_i \geq 0$ generate two scenarios:

$$\text{If } P_i = 0 \Rightarrow f_i(x) = IT \Rightarrow f_i(x) - IT = 0.$$

$$\text{Or } P_i > 0 \Rightarrow f_i(x) - P_i = IT \Rightarrow f_i(x) - IT = P_i.$$

We can reformulate system 8 as:

$$\min \langle f_i(x) - IT \rangle \tag{20}$$

With the bracket operator $\langle \rangle$ returns the operand value if it is positive, otherwise returns 0. By this way a GP problem is rewritten to multi objective problem, and we can use NSGA to solve it. The advantage is that we can get several solutions to the GP problem simultaneously which are not subjective to the user. We use a population of size 50 for a 50 generation.

RAHOU *et al* [2] consider the following part as a test piece Figure. 4. The tolerance interval is fixed at 0.02 (IT = 0.02). The results of the following system (21) are shown in Figure 5 and listed in the table. 1.

$$\begin{aligned} \min \langle f_1(x_1) - 0.02 \rangle \\ \min \langle f_2(x_2) - 0.02 \rangle \\ \min \langle f_3(x_3) - 0.02 \rangle \\ \min \langle f_1(x_1) + f_2(x_2) + f_3(x_3) - 0.02 \rangle \end{aligned} \tag{21}$$

Subject to
 $1 \leq x_1 \leq 25, 1 \leq x_2 \leq 25, 1 \leq x_3 \leq 40.$

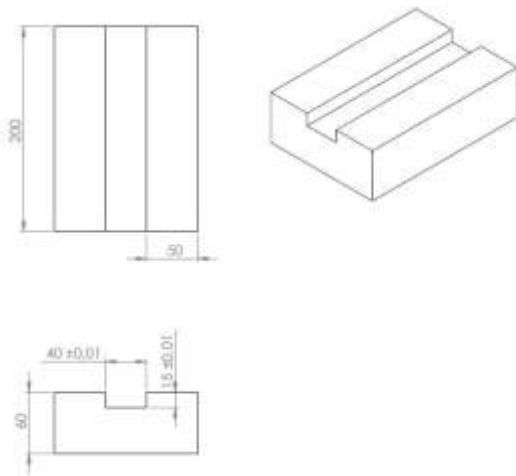


Figure 4. test piece

Figure 5. Optimization result

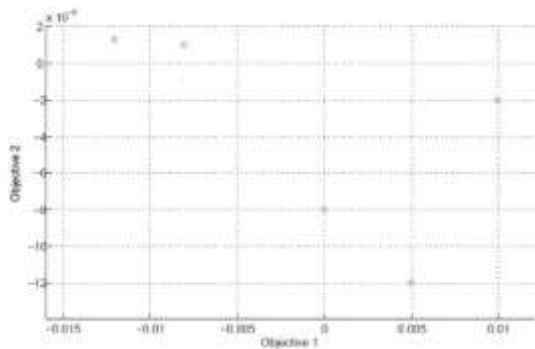


Table 1. Optimization result

x_1	x_2	x_3	$f_1(x_1)$	$f_2(x_2)$	$f_3(x_3)$	$\sum_1^3 f_i(x_i)$
1	5	1	0	-0.008	0	-0.008
10	7	15	-0.008	0.001	0.01	0.003
17	10	20	0.01	-0.002	0.012	0.02
20	14	30	-0.012	0.0013	0.017	0.0063
24	21	40	0.005	-0.012	0.027	0.02

We can notice that all the result founded are less then IT= 0.02, more on that, the sum of the machining errors is less than the IT.

We can also fix some errors at the minimum, in order to get the max of the other errors with the condition that the sum of all the machining errors are less than IT. For example, we can set tool wear error at 0.02, which mean we change the cutting tool when the tool wear error exceeds 0.02 however, that mean we minimize in the tool life. But in the other hand we can permit to maximize the amount of the other errors like table motion error, considering the sum of all the machining errors are less than or equal to design tolerance IT.

Based on this study and the result listed in the table 1, we can see that the workpiece accuracy is more influenced by the tool wear error f_3 , approximately by 42% than the other errors.

6. Conclusion

In this paper, we simultaneously consider tool wear-, table motion-, and tool path errors and have addressed the accuracy – errors trade off problem for multi-axis machine tools. A new methodology is developed in this study for optimizing the machining errors of multi-axis machine tools and the procedure of reallocating of each machining error. This was achieved by optimizing the machining errors and taken the design tolerance as hard constraint in order to achieve zero percent rejection. The machining errors considered in this study mentioned above are modeled based on cubic spline interpolation, then based on goal programming the optimization problem is formulated. Finally, NSGA is used to solve this problem. The result obtained in this study are summarized here:

- Using cubic spline interpolation for modeling generate high accuracy model of machining errors with low degree polynomials.
- It is robust
- Zero percent rejection of machining parts are obtained by this method
- More complex models for 100% conformity rate by including other errors can easily be applied using the same framework.

In terms of shortcomings of the work and areas of future studies, the following issues would be recommended for further studies:

This work considers only tool path-, tool wear-, and table motion errors. Extension to the other errors such as thermal induced errors should be considered in future research.

References

- [1] Y. Chen, H. Tang, Q. Tang, A. Zhang, D. Chen, K. Li, "Machining error decomposition and compensation of complicated surfaces by EMD method". *Measurement*, Vol. 116, 2018, 341-349. <https://doi.org/10.1016/j.measurement.2017.11.027>
- [2] M. Rahou, A. Cheikh, F. Sebaa, "Real Time Compensation of Machining Errors for Machine Tools NC Based on Systematic Dispersion". *Jordan Journal of Mechanical & Industrial Engineering*, Vol. 4, No. 5, 2010.
- [3] J. Lai, J. Fu, C. Xia, Z. Lin, G. Fu, Z. Chen, "Error compensation of free-form surface with critical area based on T-spline surface reconstruction". *International Journal of Computer Integrated Manufacturing*, Vol. 30, No. 8, 2017, 782-791. <http://dx.doi.org/10.1080/0951192X.2016.1187302>
- [4] M. Samhouri, A. Al-Ghandoor, S.A. Ali, I. Hinti, W. Massad, "An intelligent machine condition monitoring system using time-based analysis: neuro-fuzzy versus neural network". *Jordan Journal of Mechanical and Industrial Engineering*, Vol. 3, No. 4, 2009, 294-305.
- [5] A.M. Abdulshahed, P. Longstaff, S. Fletcher, "The application of ANFIS prediction models for thermal error compensation on CNC machine tools". *Applied Soft Computing*, Vol. 27, 2015, 158-168. <http://dx.doi.org/10.1016/j.asoc.2014.11.012>
- [6] M. Wiessner, P. Blaser, S. Böhl, J. Mayr, W. Knapp, K. Wegener, "Thermal test piece for 5-axis machine tools". *Precision Engineering*, Vol. 52, 2018, 407-417. <https://doi.org/10.1016/j.precisioneng.2018.01.017>
- [7] Goyal, S. Dhiman, S. Kumar, R. Sharma, "A Study of Experimental Temperature Measuring Techniques used in Metal Cutting". *Jordan Journal of Mechanical & Industrial Engineering*, Vol. 8, No. 2, 2014, 82-93.
- [8] P. Blaser, F. Pavliček, K. Mori, J. Mayr, S. Weikert, K. Wegener, "Adaptive learning control for thermal error compensation of 5-axis machine tools". *Journal of Manufacturing Systems*, Vol. 44, 2017, 302-309. <http://dx.doi.org/10.1016/j.jmsy.2017.04.011>
- [9] D. Zhao, Y. Bi, Y. Ke, "An efficient error prediction and compensation method for coordinated five-axis machine tools under variable temperature". *The International Journal of Advanced Manufacturing Technology*, Vol. 96, No. 9-12, 2018, 4431-4443. <https://doi.org/10.1007/s00170-018-1923-z>
- [10] H. Yu, S. Qin, G. Ding, L. Jiang, L. Han, "Integration of tool error identification and machining accuracy prediction into machining compensation in flank milling". *The International Journal of Advanced Manufacturing Technology*, Vol. 102, No. 9-12, 2019, 3121-3134. <https://doi.org/10.1007/s00170-019-03365-2>
- [11] L. Zhong, Q. Bi, Y. Wang, "Volumetric accuracy evaluation for five-axis machine tools by modeling spherical deviation based on double ball-bar kinematic test". *International Journal of Machine Tools and Manufacture*, Vol. 122, 2017, 106-119. DOI 10.1016/j.ijmactools.2017.06.005
- [12] Z. Zhao, D. Ding, Y. Fu, J. Xu, "Measured data-driven shape-adaptive machining via spatial deformation of tool cutter positions". *Measurement*, Vol. 135, 2019, 244-251. <https://doi.org/10.1016/j.measurement.2018.11.051>
- [13] M. Soori, B. Arezoo, M. Habibi, "Tool deflection error of three-axis computer numerical control milling machines, monitoring and minimizing by a virtual machining system". *Journal of Manufacturing Science and Engineering*, Vol. 138, No. 8, 2016. <https://doi.org/10.1115/1.4032393>
- [14] D. Dinakaran, S. Sampathkumar, J.S. Mary, "Real time prediction of flank wear by neuro fuzzy technique in turning". *Jordan Journal of Mechanical & Industrial Engineering*, Vol. 4, No. 6, 2010, 725-732.
- [15] M.V. Nojdedeh, M. Habibi, B. Arezoo, "Tool path accuracy enhancement through geometrical error compensation". *International Journal of Machine Tools and Manufacture*, Vol. 51, No. 6, 2011, 471-482. doi:10.1016/j.ijmactools.2011.02.005
- [16] M. Pezeshki, B. Arezoo, "Kinematic errors identification of three-axis machine tools based on machined work pieces". *Precision Engineering*, Vol. 43, 2016, 493-504. <http://dx.doi.org/doi:10.1016/j.precisioneng.2015.09.018>
- [17] F. Viprey, H. Nouira, S. Lavernhe, C. Tournier, "Novel multi-feature bar design for machine tools geometric errors identification". *Precision Engineering*, Vol. 46, 2016, 323-338. <http://dx.doi.org/doi:10.1016/j.precisioneng.2016.06.002>
- [18] N. Huang, Y. Jin, X. Li, L. Liang, S. Wu, "Identification of integrated geometric errors of rotary axis and setup position errors for 5-axis machine tools based on machining test". *The International Journal of Advanced Manufacturing Technology*, Vol. 102; No. 5-8, 2019, 1487-1496. <https://doi.org/10.1007/s00170-018-03223-7>
- [19] Q. Bi, N. Huang, C. Sun, Y. Wang, L. Zhu, H. Ding, "Identification and compensation of geometric errors of rotary axes on five-axis machine by on-machine measurement". *International Journal of Machine Tools and Manufacture*, Vol. 89, 2015, 182-191. <http://dx.doi.org/10.1016/j.ijmactools.2014.11.008>
- [20] J. Yang, H. Ding, "A new position independent geometric errors identification model of five-axis serial machine tools based on differential motion matrices". *International Journal of Machine Tools and Manufacture*, Vol. 104, 2016, 68-77. <http://dx.doi.org/10.1016/j.ijmactools.2016.02.001>
- [21] J. Creamer, P.M. Sammons, D.A. Bristow, R.G. Landers, P.L. Freeman, S.J. Easley, "Table-based volumetric error compensation of large five-axis machine tools". *Journal of Manufacturing Science and Engineering*, Vol. 139, No. 2, 2017. <https://doi.org/10.1115/1.4034399>
- [22] D. Chen, S. Zhang, R. Pan, J. Fan, "An identifying method with considering coupling relationship of geometric errors parameters of machine tools". *Journal of Manufacturing Processes*, Vol. 36, 2018, 535-549. <https://doi.org/10.1016/j.jmapro.2018.10.019>
- [23] Salomon D. Curves and surfaces for computer graphics. Springer, New York, NY; 2007. <https://doi.org/10.1007/0-387-28452-4>
- [24] Rahou M. Contribution au développement de nouvelles approches de tolérancement pour l'usinage sur machine-outil à commande numérique. Ph.D. thesis, Tlemcen University, Algeria. 2010.
- [25] Deb K. Multi-objective optimization using evolutionary algorithms. Chichester: John Wiley & Sons; 2001.

Thermal Analysis of a Combined Cycle Power Plant under Varying Operating Conditions

Mustafa Al-Qudah^a, Ahmad Sakhrieh^{b,c,*}, Ali Almarzouq^d, Ahmad Al-Omari^e

^aKOSPO/Jordan O&M company for Qatrania Electrical Power Company, Jordan

^bMechanical Engineering Department, The University of Jordan, Amman 11942, Jordan

^cDepartment of Mechanical and Industrial Engineering, American University of Ras Al Khaimah, 10021, United Arab Emirates

^dNational Energy Research Center / Royal Scientific Society, Jordan

^eQatrania Electric Power Company, Jordan

Received August 16 2019

Accepted November 16 2020

Abstract

Combined Cycle Power Plants are preferred for their high efficiency and low pollutant emissions. Combined cycle power plants are becoming increasingly prevalent in the Jordanian electric market place. The output of CCPPs in operation in Jordan counts 2,180 MW which represents 55% out of total installed generation capacity. In this work, the effect of Turbine Inlet Temperature on the net output work and thermal efficiency of the combined cycle are investigated. The power output and thermal efficiency are increasing with increasing Turbine Inlet Temperature. The performance of the power plant was analyzed for two types of fuels; natural gas and fuel oil with 100% and 75% load factors. It was found that Al-Qatrania Power Plant has a maximum efficiency of 43.25% when operated with 100% NG. This produces 374.62 MW total output power. Increasing Turbine Inlet Temperature increased the overall thermal efficiency to 43.69% and the total output power to 378.51MW.

© 2020 Jordan Journal of Mechanical and Industrial Engineering. All rights reserved

Keywords: CCPP, power plant, TIT;

List of abbreviations

CCPPs	Combined Cycle Power Plants
TIT	Turbine Inlet Temperature
NG	Natural Gas
FO	Fuel Oil
ST	Stem Turbine
GT	Gas Turbine
HRSG	Heat Recovery Steam Generator
AQPP	Al-Qatrania Power Plant
CHP	Combined Heat and Power
OTC	Outlet Temperature Control

1. INTRODUCTION

Combined Cycle Power Plants (CCPPs) are the preferred technology for electricity generation due to its high efficiency and low emitted pollutants. CCPPs' efficiency ranges from 40 - 60%. CCPP consists of a Gas Turbine (GT), Heat Recovery Steam Generator (HRSG), Steam Turbine (ST), condenser, and balance of plant equipment such as fuel system, boiler feed pump, water treatment plant, etc. The major difference between a conventional power plant and a combined cycle power plant is that the CCPP utilizes exhaust gases from GT to turn

water into steam inside the HRSG. In the CCPP, both the GT and ST produce electricity, whereas, in conventional power plants, electricity is produced in ST only.

According to thermodynamic principles, inputs and outputs are needed to calculate the efficiency of a system. If the efficiency of the system under study is less than the recommended efficiency by the manufacturer, a deep analysis of the system should be conducted to reduce losses and increase efficiency. Due to the difference between actual and recommended Al-Qatrania Power Plant (AQPP) efficiencies, energy analysis for AQPP is required to improve the power plant performance. This will be reflected on the plant's output power, consumed fuel, and emissions.

There are several methods used to improve power plant efficiency. Energy analysis of the power plant and its operating parameters is one of these methods. In this context, many studies have been delivered in the last few years. Jamnani and Kardgar [1] performed energy-exergy analysis for the gas-fired combined-cycle power plant which will be constructed in Kuantan and Kapar in the Malay Peninsula in 2020. The study revealed that numerous considerations for the CCPPs can be implemented to identify irreversibilities and use several methods to improve plant performance. Suresh et al [2] applied thermodynamic analysis on a Combined Heat and Power (CHP) plant. Energy and exergy analyzes are carried out based on the first and second thermodynamics laws for power generation systems including a 10 MW solar combustion gas turbine, a 4 MW steam turbine, a 100,000 pph heat recovery steam

* Corresponding author e-mail: ahmad.sakhrieh@aurak.ac.ae.

generator (HRSG), three 125,000 pph package boilers and auxiliary equipment. They used actual system data to assess the district heating system performance, energy and exergy efficiencies, exergetic improvement potential, and exergy losses. The results showed how thermodynamic analysis can be used to identify the magnitudes and location of energy losses to improve the existing system, processes, or components. Polyzakis et al [3] analyzed a combined cycle power plant describing and comparing four different gas turbine cycles; simple cycle, inter-cooled cycle, reheated cycle and intercooled and reheated cycle. The proposed combined cycle plant would produce 300 MW of power (200 MW from the gas turbine and 100 MW from the steam turbine). They showed that the reheated gas turbine is the most desirable, mainly because of its high turbine exhaust gas temperature which causes the high thermal efficiency of the bottoming steam cycle. They concluded that the optimal gas turbine cycle leads to a more efficient combined cycle power plant (CCPP). Fellah et al., [4] conducted an exergoeconomic analysis for Unit Gt14 of South Tripoli Gas Turbine Power Plant. The analysis assists in the understanding of the cost value associated with exergy destroyed in a thermal system, and hence provides energy system's designers and operators with the information, necessary for operating, maintaining, and evaluating the performance of energy systems.

Ankur Geete and A.I.Khandwawala [5] generated correction curves for power and heat rate. The thermodynamic analysis of 120 MW thermal power plant has been done at particular inlet pressure and at different inlet temperatures. Mohanty and Venkatesh [6] studied the effect of various operating parameters such as TIT and pressure ratio of the Brayton cycle on the net output work and thermal efficiency of the combined cycle. They found that TIT of Brayton cycle has significant effects on the performance of the CCPP. Also, they found that the power output of Rankine cycle is strongly affected by TIT. Lebele-Alawa and Asuo [7] studied the effect of the variation of power turbine inlet temperature on the performance of a gas turbine. They found that when TIT was reduced, the turbine efficiency and power output were reduced. Ersayin and Ozgener [8] implemented a performance analysis of an operating power plant with actual operating data acquired from the power plant control unit. Energy and exergy efficiencies of each component of the power plant system were calculated. They applied the first law and the second law of thermodynamics, energy and exergy efficiencies of the combined cycle power plant were found as 56% and 50.04% respectively. Kumar and Singh [9] developed a general model of a combined cycle performance for varying TIT. They found that by increasing TIT from 1600 K to 1800 K, the combined cycle efficiency

increases by 2.37%, and the combined specific work increases by 185.42 kJ/kg. Recently, several researchers studied the use of solar energy for integration with power-plant units. Ahmadi et al., [10] investigated a full repowering simultaneously with merging solar energy in 200 MW units of Montazeri steam power plant in Iran. The study indicated that the energy and exergy efficiencies have increased.

Due to the difference between actual and recommended Al-Qatrana Power Plant (AQPP) efficiencies, energy analysis for AQPP is required to improve the power plant performance. In this work, the actual performance of Al-Qatrana Power Plant (AQPP) has been calculated using data extracted from the plant's control system and compared with the theoretical ones. The difference between the actual and theoretical performance measures the potential for future improvements. Furthermore, the performance of the AQPP has been evaluated under the variation of two operating parameters; fuel types and power output factor. The study analyzed the effect of these variations on power output and thermal efficiency. These parameters were selected because they are the main parameters that affect the operation performance. After performance evaluation under these parameters completed, the effect of increasing TIT on actual power output and thermal efficiency has been studied as a suggested improvement.

2. THEORETICAL BACKGROUND

Thermodynamic principles are used to determine the energy content of a system and to calculate system efficiency.

Energy balance for a system undergoing any kind of process is expressed in Equation 1 [11, 12]

$$E_{in} - E_{out} = \Delta E_{system} \quad (1)$$

Equation 2 is the control volume energy rate balance for a steady state steady flow process, [11, 12]

$$\dot{Q}_{C.V} + \sum \dot{m}_i \left(h_i + \frac{v_i^2}{2} + g \cdot Z_i \right) = \sum \dot{m}_e \left(h_e + \frac{v_e^2}{2} + g \cdot Z_e \right) + \dot{W}_{C.V} \quad (2)$$

Figure 1 illustrates the energy flow in CCPP. The energy chain at CCPP is divided into two areas; GTG and STG. In GTG, fuel burns inside combustion chambers and produces heat that drives the turbine and generator where the work is produced. The flue gas leaves the GTG at a temperature of 500 °C or more. Flue gas is directed to HRSG to produce superheated steam which drives the STG to generate the second portion of work. As a result, the total work produced from CCPP is the work from GTG and STG.

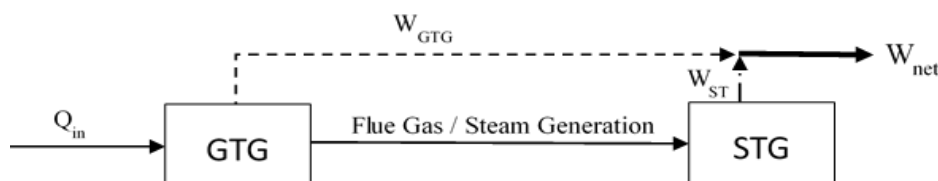


Figure 1. CCPP Energy Chain

Combined cycles have separate cycles with different fluids; air and flue gases inside Brayton cycle and water or steam in Rankine cycle. The enthalpy of each fluid is calculated as follows:

1. The enthalpy of the ideal gas mixtures is determined as the sum of the particular properties of the component gases as shown in Equation 3

$$h = \sum_{i=1}^k (mf_i * h_i) \tag{3}$$

where $h_i = \int c_{pi} dt$, $cp = \sum_{i=1}^k (mf_i \cdot c_{pi})$

mf_i is a practical mass fraction of ideal gas, c_{pi} is obtained from the table of each gas at a certain temperature.

2. The thermodynamic properties of the water and steam are obtained from steam tables at a certain pressure and temperature

The thermal efficiency of CCPP is calculated using equation 4 [11, 12], where the W is the output work in and Q is the heat added by burning the fuel, either in terms of kJ or kJ/kg.

$$\eta_{th} = \frac{W_{net}}{Q_{in}} \quad \text{or} \quad \eta_{th} = \frac{w_{net}}{q_{in}} \tag{4}$$

One of the methods used to improve the efficiency of a gas turbine is to increase the turbine inlet temperature. TIT is one of the most critical parameters which influence the gas turbine performance. Usually, TIT is kept constant during GT operation. Increasing TIT will be reflected on CCPP efficiency and power output. It should be ensured that TIT temperature increase has no negative impact on GT's material strength and burner's performance.

The basic principle of combustion chamber operation is based on the energy balance principle. The direct effect of TIT on flue gas energy is calculated using Equation (5) [6],

$$m_a C_{pa} T_2 + m_f \times LHV + m_f C_{pf} T_f = (m_a + m_f) C_{pg} \times TIT \tag{5}$$

Where m_f is the mass flow rate of the fuel (kg/s), m_a is the mass flow rate of air (kg/s), LHV is low heating value, TIT is the turbine inlet temperature, C_{pa} , C_{pf} and C_{pg} are the specific heat of air, fuel and flue gases respectively, and T_f is the temperature of the fuel.

Increasing TIT should be within the acceptable range of the GTG manufacturer. Moreover, the effect on HRSG and STG should also be evaluated and consulted with the manufacturers. It should also be ensured that increasing TIT will not affect GTG and HRSG materials and burner's performance

3. PLANT DESCRIPTION AND ANALYSIS

Al-Qatrana electric power company (AQPP) is a private shareholding company producing 373 MW in Al-Qatrana town. AQPP consists of two GT, two HRSG, one ST, an air-cooled condenser (ACC), and a balance of plant equipment such as fuel systems, boiler feed pumps, water treatment plant, etc. as shown in figure 2 [13]. AQPP uses Natural Gas as a primary fuel, and Fuel Oil as a backup fuel. The GTs used in AQPP are Siemens SGT5-2000E. They are using Outlet Temperature Control (OTC) that controls (but not measure) temperature inside GT combustion chamber. OTC value depends on GT exhaust temperature and ambient temperature. TIT can be increased by increasing OTC value. A standard combined cycle is considered for the present analysis. Air after compression in the compressor enters the combustion chamber where its temperature is raised by the combustion of fuel. The gases then expand in the turbine and produce the work output part of which is supplied to run the compressor. The heat carried by the exhaust gases is recovered in the HRSG to generate steam for expansion in the steam turbine.

AQPP has been operating for ten years as a baseload power plant. The plant is always in-operation except for the annual maintenance. Table (1) shows the operation parameters such as energy consumption, production, and performance indicators for the AQPP power plant for three years. The actual performance is compared with the theoretical one. The energy analysis is performed on the power plant using two types of fuels; natural gas (NG) and fuel oil (FO) with 100% and 75% load factors.

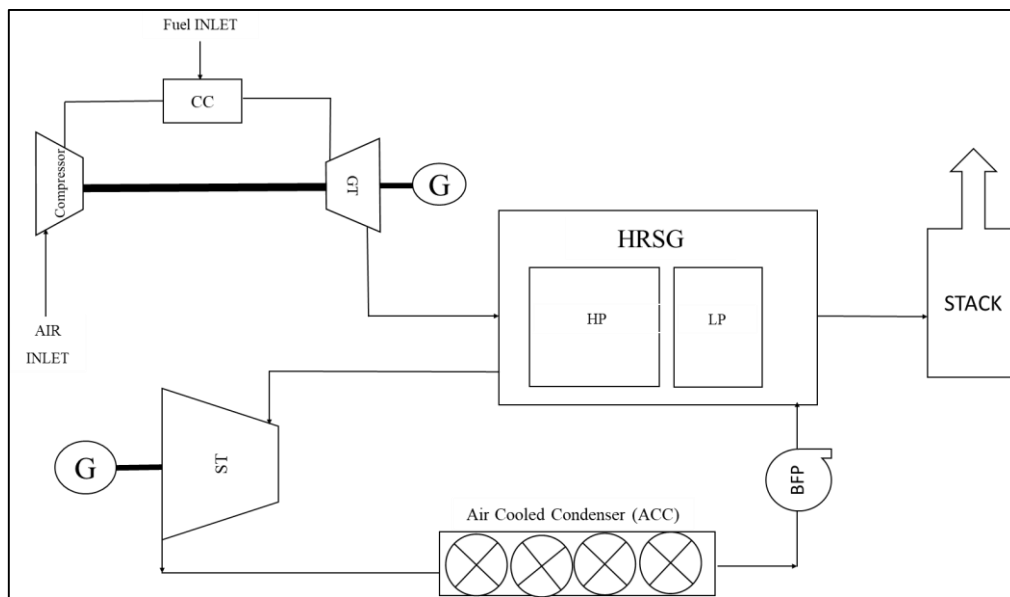


Figure 2. Schematic diagram of AQPP

Table 1. AQPP Operation Parameters

Item	Year 1	Year 2	Year 3
Generated Energy (MWh)	2,436,533	1,509,033	2,274,288
FO Consumption (GJ)	11,150,879	2,489,148	15,196,597
NG Consumption (GJ)	9,105,093	10,523,838	3,934,116
Internal consumption Rate (%)	1.70%	1.89%	1.62%
Plant Availability (%)	97.46%	92.59%	92.70%
Utilization Factor (%)	73.43%	45.63%	68.60%
Actual Efficiency (%)	39.56%	37.95%	38.96%

In Table 1, the fuel used over the period is a mix of NG and FO, due to a shortage in NG supply. In the second year, the planned maintenance was longer than the other two years. The effect of this breakdown is shown in the reduction in the generated energy, plant availability, and utilization factor percentage. The actual efficiency is calculated annually when AQPP is operated using both fuel types and various power output ranges.

The data required to calculate the theoretical performance of AQPP is taken from the manufacturers of the power plant equipment (GT, STG, and HRSG) at AQPP reference conditions. The actual performance of AQPP is conducted in normal operation days. The actual performance is corrected to reference conditions because values are related to reference conditions such as site conditions and the operational parameters of plant equipment. The correction curves are usually supplied by the original equipment manufacturers. Table 2 presents AQPP reference conditions.

The three correction factors listed below are the most important factors which indicate the operational effects on thermal input and power and thus requiring all measured

values of the thermal input and power to be corrected to reflect the accurate analysis and results; these factors have been considered for the energy analysis of this work:

1. Ambient temperature
2. Ambient pressure
3. Ambient humidity

Table 2. AQPP reference conditions

Item	Reference value
Barometric Pressure	0.9270 bar
Inlet Air Temperature	36 °C
Relative Humidity	55 %
Frequency	50 H z
Power Factor	0.85

The cycle thermal efficiency and output power were calculated using two fuels; NG and FO with different load factors. The operation matrix is presented in Table 3.

Table 3. Operation Matrix

Fuel type	Output load factor	
NG	100 % of full output power	75 % of full output power
	100 % of full output power	75 % of full output power

The actual thermodynamic properties of each stream are shown in Table 4. These properties were collected from AQPP control system. Equation 3 is used to calculate the enthalpy of each stream. It is more accurate to calculate the enthalpy of the mixture as a summation of individual species enthalpies rather than taking a rough estimation that the whole mixture behaves as air [14]. In this work, the enthalpies for each case under study were calculated based on exhaust gas percentages presented in Table 4.

Table 4. Plant Streams Thermodynamic Properties

NG Operation										
Power Output Factor			100 %				% 75			
Component	State		T [°C]	P [kPa]	m [kg/s]	h [kJ/kg]	T [°C]	P [kPa]	m [kg/s]	h [kJ/kg]
1	Compressor	Inlet air	5.85	91.43	1030.00	280.02	15.78	92.25	945.00	288.94
2	Compressor	Outlet air	332.00	1110	1030.00	613.21	314.60	901.76	945.00	626.33
3	Turbine	fuel inlet (NG)	52.04	1999.52	20.00	4605.00	117.30	2053.65	15.00	878.94
4	Turbine	Turbine outlet	527.64	137.60	1050.00	958.92	529.21	110.00	960.00	954.93
5	HRSG	Main stack	132.38	101.00	1050.00	442.61	123.25	101.00	960.00	431.90
6	HRSG	inlet Water	48.26	2389.90	125.01	204.10	45.75	2385.37	102.24	193.60
7	STG	HP Steam	506.15	7009.32	106.15	3425.12	511.25	6606.00	84.00	3442.00
8	STG	LP Steam	193.76	465.18	17.04	2844.00	194.69	317.20	15.38	2854.00
9	STG	Exhaust steam	52.89	15.00	123.20	2362.00	45.10	10.00	99.38	2345.00
10	ACC	Condensate	47.07	37.36	123.20	197.10	44.20	35.64	99.38	185.10
FO Operation										
Power Output Factor			%100				%75			
Component	State		T [°C]	P [kPa]	m [kg/s]	h [kJ/kg]	T [°C]	P [kPa]	m [kg/s]	h [kJ/kg]
1	Compressor	Inlet air	30.12	91.39	866.33	309.82	11.69	92.62	791.82	309.82
2	Compressor	Outlet air	355.04	1013.98	866.33	673.74	289.60	830.59	791.82	673.74
3	Turbine	fuel inlet (FO)	33.05	516.01	18.67	535.58	28.77	313.40	14.18	528.10
4	Turbine	Turbine outlet	518.01	121.68	885.00	944.64	484.37	104.53	806.00	944.64
5	HRSG	Main stack	172.44	101.30	885.00	488.16	165.86	101.30	806.00	488.16
6	HRSG	inlet Water	52.21	2028.43	97.00	220.30	52.67	2553.09	84.60	222.60
7	STG	HP Steam	501.51	6574.60	94.06	3419.00	494.47	6517.37	79.56	3403.00
8	STG	LP Steam	197.09	279.00	2.68	2861.00	197.87	234.00	4.99	2864.00
9	STG	Exhaust steam	50.18	10.14	96.74	2354.00	51.20	10.25	84.55	2595.00
10	ACC	Condensate	50.06	38.74	96.74	209.60	51.06	40.22	84.55	213.80

Table 5. Exhaust Gases Composition

Fuel type	NG		FO		
	Output power factor	100%	75%	100%	75%
CO2		3.34%	3.21%	4.15%	3.98%
N2		75.18%	75.27%	76.21%	76.27%
H2O		7.01%	6.76%	4.36%	4.21%
O2		13.60%	13.87%	14.37%	14.63%

Table 5 was used to calculate the actual thermal efficiency and power output. The calculated values were corrected to reference conditions. These values were compared with the theoretical ones that have been calculated using manufacturers' data.

4. RESULTS AND DISCUSSION

AQPP thermal efficiency and power output were calculated and presented in Figures 3 and 4. Using NG (100% load factor) leads to the highest efficiency and power output for theoretical and actual cycles. The maximum difference (4.59%) between theoretical and actual cycle efficiency is obtained when NG 100% load factor is used. The minimum difference (2.88%) between theoretical and actual cycle efficiency is achieved when FO 75% load factor is used. The difference between theoretical and actual output power is around 5 MW for all fuels with different load factors except NG 75% load factor. Operating the power plant using NG is more efficient than using FO due to the fact that GT power output and HRSG efficiency are higher when NG is used. As shown in Table 5 the flue gas leaves the combined cycle at 132 °C and 172 °C when GT operates using NG and FO respectively. This dissipates more energy when the plant is operated using FO. The plant draws hotter flue gases to the atmosphere in case of FO operation to avoid SO_x dew point on the main stack because FO contains more sulfur than NG.

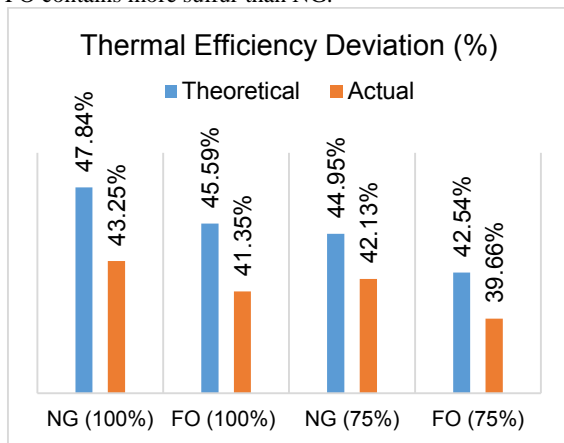


Figure 3. Theoretical and Actual Thermal Efficiency

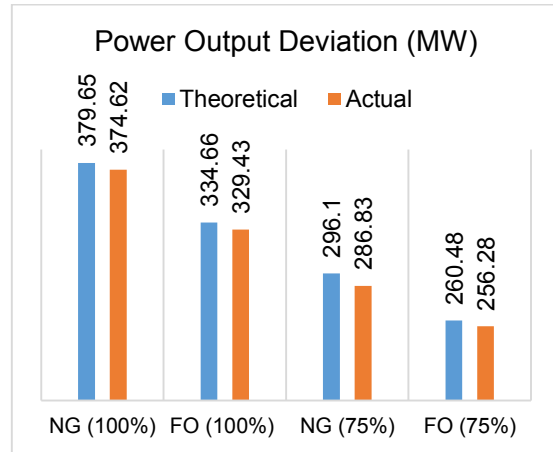


Figure 4. Theoretical and Actual Power Output

The turbine inlet temperature (TIT) plays an important role on the performance of combined cycle. Table 6 presents the effect of increasing TIT on GT power output, GT efficiency, plant overall thermal efficiency, and plant power output. The actual performance of AQPP has been calculated using data extracted from the plant's control system. OTC was increased from 523 °C to 533 °C (10 degrees). TIT significantly affects the performance of the gas turbine engine. GT output, GT efficiency, plant overall thermal efficiency, and plant power output are improved by increasing TIT temperature. TIT should be kept higher to minimize losses in the gas turbine system. Increasing the TIT increases the output power and thermal efficiency as a result of increasing the turbine work. For STG, GT flue gas mass flow rate is increased which is reflected positively on steam quantity produced from HRSG. GT power output has a direct relation with TIT. In summary, Power output is increased when TIT is increased due to GT and STG power output increase. Kaviri et al. [15], indicated that increasing the gas turbine inlet temperature decreases the combustion chamber exergy destruction. The reason is due to the fact that this increase leads to the decrease of the entropy generation. Compared to Sanjay [16], the parameter that affects cycle performance most is the TIT (turbine inlet temperature).

Table 6. The effect of increasing TIT on power plant performance

	OTC (523 °C)	OTC (533 °C)	Improvement
GT Efficiency (%)	29.35	29.87	0.52
Overall Efficiency (%)	43.25	43.69	0.44
GT power output (MW)	127.14	129.25	2.11
Power plant power output (MW)	372.63	378.51	5.88

The actual results are compared with theoretical ones. The difference between the theoretical cycle efficiency and the actual cycle efficiency was reduced from 4.5% to 4.1% as shown in figure 5. The effect of increasing TIT on the overall power output is presented in figure 6. The calculations revealed that the power output increased from 374.62 MW to 378.51 MW with a difference of 4.1 MW between the theoretical and the improved cycle.

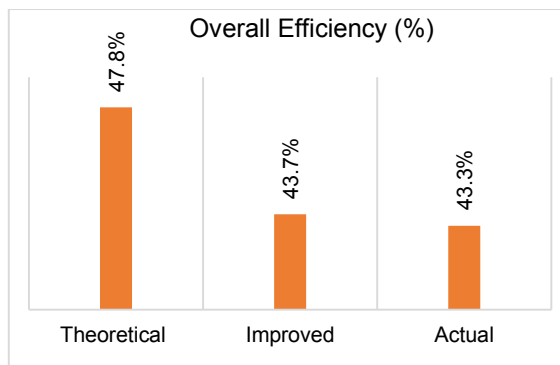


Figure 5. Theoretical and Improved Overall Thermal Efficiency deviation

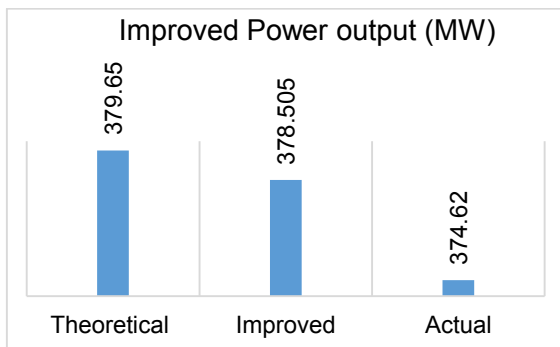


Figure 6. Theoretical and Improved Plant Overall Power output Gap

The study results provide useful information and guidelines to power plant engineers and operators; such as choosing possible performance enhancement modifications to combined cycle power plants.

5. CONCLUSIONS

The current study presents an analysis of Al-Qatrana combined cycle power plant using real data extracted from the plant's control system. The effect of TIT on GT power output, GT efficiency, plant overall thermal efficiency, and plant power output was calculated and compared with the theoretical values. The turbine inlet temperature significantly affects the performance of the combined cycle. It should be kept on the higher side for minimizing the exergy losses. The results obtained were validated against published data. Furthermore, the performance of the power plant was analyzed for two types of fuels; natural gas and fuel oil with 100% and 75% load factors. Operating the power plant using NG is more efficient than FO.

These results are very helpful for future improvements because the difference between the actual and theoretical performance measures the potential for future improvements. This difference could be further reduced by increasing HRSG heat transfer efficiency.

REFERENCES

- [1] Mohammadreza Babaei Jamnani and Amin Kardgar (2020), "Energy-exergy performance assessment with optimization guidance for the components of the 396-MW combined-cycle power plant", *Energy Sci Eng.* 2020;00:1–14.
- [2] Sharan Suresh, Hariharan Gopalakrishnan and Dr. Dragoljub Kosanovi (2011), "Thermodynamic Analysis of Combined Cycle District Heating System", *Proceedings of the 2011 Industrial Energy Technology Conference New Orleans, Louisiana, May 17-19, 2011*
- [3] A.L. Polyzakis, C. Koroneos and G. Xydias (2008), "Optimum Gas Turbine Cycle for Combined Cycle Power Plant", *Energy Conversion and Management* 49 (2008) 551–563
- [4] Giuma M. Fellah, Fathi A. Mgherbi, Saleh M. Aboghres (2010), "Exergoeconomic Analysis for Unit Gt14 of South Tripoli Gas Turbine Power Plant, *Jordan Journal of Mechanical and Industrial Engineering*, Volume 4, Number 4, 2010
- [5] Ankur Geete and A.I.Khandwawala (2013), "Thermodynamic analysis of 120 MW thermal power plant with combined effect of constant inlet pressure (124.61 bar) and different inlet temperatures, *Case Studies in Thermal Engineering*, Volume 1, Issue 1, October 2013, Pages 17-25
- [6] Dillip Kumar Mohanty and Vijay Venkatesh (2014), "Performance Analysis of a Combined Cycle Gas Turbine Under Varying Operating Conditions", *Mechanical Engineering: An International Journal (MEIJ)*, Vol. 1, No. 2, August 2014
- [7] Barinaadaa Thaddeus Lebele-Alawa and Jerry Mike Asuo, "Influence of the Variation of Power Turbine Inlet Temperature on Overall Turbine Efficiency, *International Journal of Engineering and Innovative Technology (IJET)* Volume 2, Issue 7, January 2013
- [8] Erdem Ersayin and Leyla Ozgener (2014), "Performance analysis of combined cycle power plants: A case study", *Renewable and Sustainable Energy Reviews* 43, 832–842
- [9] Sanjay Kumar and Onkar Singh (2013), "Performance Evaluation of Gas-Steam Combined Cycle Having Transpiration Cooled Gas Turbine", *Distributed Generation and Alternative Energy Journal* Vol. 28, No. 2.
- [10] Gholamreza Ahmadi, Davood Toghraie, Ahmadreza Azimian, Omid Ali Akbari (2017), "Evaluation of synchronous execution of full repowering and solar assisting in a 200 MW steam power plant, a case study", *Applied Thermal Engineering*, Volume 112, Pages 111-123.
- [11] Yunus A. Cengel and Michael A. Boles, *Thermodynamics an engineering approach*, the McGraw-Hill Inc., USA, 2006
- [12] Claus Borgnakke and Richard E. Sonntag, *Fundamentals of Thermodynamics*, John Wiley and Sons Inc., U.S.A., 2009
- [13] Power plant description (2009), KOSPO/Jordan, AlQatrana, Jordan
- [14] Sakhrieh, E. Abu-Nada, B. Akash, I. Al-Hinti, A. Al-Ghandoor, "Performance of Diesel Engine using Gas Mixture with Variable Specific Heats Model, *Journal of the Energy Institute*, Volume 83, 217-224, 2010.
- [15] Kaviri AG, Jaafar MNM, Lazim TM (2012) Modeling and multi-objective exergy based optimization of a combined cycle power plant using a genetic algorithm. *Energ Convers Manage* 58: 94-103.
- [16] Sanjay (2011), "Investigation of effect of variation of cycle parameters on thermodynamic performance of gas-steam combined cycle. *Energy* 36: 157-167

In-situ Hybridization of Waste Palm Oil: A Physicochemical, Thermal, and Spectroscopic analysis

Josiah Pelemo, Omojola Awogbemi* , Freddie Inambao, Emmanuel I. Onuh

Discipline of Mechanical Engineering, University of KwaZulu-Natal, Durban, South Africa

Received October 25 2020

Accepted November 25 2020

Abstract

Hybridization is one of the techniques for unearthing novel feedstock and diversifying the existing waste cooking oil feedstock stream. In the present research, in-situ hybridization was carried out on waste palm oil (WPO) samples obtained from different sources. The aim of this current study is to investigate the effect of hybridization on the physicochemical properties, thermal degradation, and spectroscopic on both the WPO and hybridized samples. Two WPO samples were mixed in different ratio and subjected to property determination and characterization. Hybridization was found to increase the iodine value, and reduce the density, kinematic viscosity, and saponification values but does not affect the acid value, cetane index and higher heating values of the samples. All the samples witnessed one stage of thermal decomposition; samples A, B, C, D, and E experienced 13 %, 11 %, 10 %, 8 %, and 3 % weight loss respectively between 320 °C and 470 °C. The peak of derivative weight percentage of -0.06 \%m^{-1} was observed at 433 °C, -0.05 \%m^{-1} at 430 °C, -0.11 \%m^{-1} at 432 °C, -0.09 \%m^{-1} at 422 °C, and -0.06 \%m^{-1} at 430 °C for samples A, B, C, D, and E respectively. The infrared spectrum curves revealed that the peculiar peaks at 1226 cm^{-1} , 1363 cm^{-1} , and 1378 cm^{-1} found in the parent samples A and B disappeared in the spectrum curves of hybridized samples C, D, and E. The outcome of this investigation shows that hybridization is a viable technique for improving the quality of existing feedstock as well as creating novel high-quality feedstock for biodiesel generation.

© 2020 Jordan Journal of Mechanical and Industrial Engineering. All rights reserved

Keywords: Characterization, feedstock, in-situ hybridization, waste palm oil;

1. Introduction

Renewability, biodegradability, environmental sustainability, and affordability are some of the factors that have popularized the application of biodiesel as a sustainable replacement for fossil-based diesel (FBD) fuel to run compression ignition (CI) engines. The International Energy Agency has projected that the global oil demand will escalate to 105.4 MMbpd in 2030 from the 96.9 MMbpd recorded in 2018 [1]. This increased energy demand has made the use of alternative energy a priority in order to meet the soaring global energy demand. Similarly, the damaging effect of the exploitation and utilization of FBD fuel, depletion of oil reserves, deteriorating oil production capacities, and the increasing price of FBD fuel in the global market has brought about the necessity to move to low-carbon emitting fuels a global priority. The depletion of fossil fuel reserves has made the search for alternative and sustainable fuel inevitable. Such alternative fuel must be affordable, environmentally benign, and carbon neutral [2-4].

Consequently, researchers have continued to commit considerable time and resources to the production and utilization of biodiesel [5, 6]. Biodiesel is biodegradable, more environmentally friendly, more lubricating, and it emits less carbon monoxide, soot, and unburnt hydrocarbon emissions, and generates less engine noise and vibration as

well when compared with FBD as CI engine fuel. Biodiesel has also been found to exhibit a higher cetane number and flash point, low sulphur content, and is non-carcinogenic, less toxic, and safer to handle when compared with FBD fuel [7-11].

The high cost of feedstock, the conflict between some food-based feedstock and the food chain, and scarcity of feedstock have continued to negatively impact the commercialization of biodiesel. Economically, the price of feedstock has been found to account for between 60 % to 80 % of the overall production expenditure of biodiesel [10, 12-14]. The use of inedible oil, waste cooking oil (WCO), and recovered animal fats have been discovered to considerably lower the production cost of biodiesel. The use of these feedstocks does not conflict with the food chain and serve as a sustainable waste disposal mechanism. For example, biodiesel generated from WCO was much cheaper than that generated from neat palm oil [15-17]. Lee et al. [18] reported a production cost of 0.7 US\$/L of biodiesel when using waste canola oil compared to 1 US\$/L for fresh canola oil. At 1.65 US \$/L, WCO [19] is the cheapest feedstock when compared with neat vegetable oil at 4.2 US \$/L [16], and neat soybean oil at 6.234 US \$/L [20].

Waste palm oil (WPO) is commonly used as biodiesel feedstock due mainly to its availability and reasonably low cost when compared with other forms of inedible vegetable oil [21, 22]. WPO is obtained when palm oil is used domestically for frying. Palm oil is obtained from palm

* Corresponding author e-mail: jolawogbemi2015@gmail.com.

fruit, which is predominantly grown in tropical Africa, South America, and Southeast Asia. About 90 % of palm oil is believed to be consumed domestically as food, while the remaining 10 % is used for industrial, cosmetics, lubricants, fuels, and as a bio-asphalt binder, among other uses [23, 24]. The domestic consumption of palm oil as food has continued to increase over the last five years (Figure 1). This is because of urbanization, increased population, and change of lifestyles. Exposure of palm oil to temperatures above 200 °C in the presence of moisture and salt during frying predisposes the oil to physio-chemical and thermal decomposition. Domestic consumption of palm oil that has been used for frying is harmful to health, causing cancer, diabetes, and other diseases [25, 26].

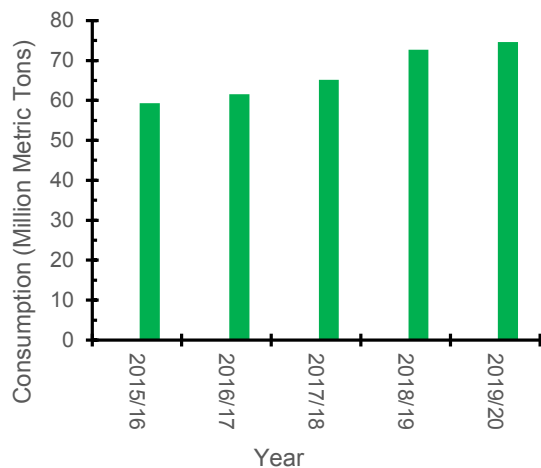


Figure 1. Consumption of palm oil (Million Metric Tons) from 2015/16 to 2019/20

Hybridization is the mixing of two or more distinct feedstocks in varying fractions to create a novel feedstock. The hybridized feedstock has always different properties compared with the parent stocks. Feedstocks can be hybridized in-situ, ex-situ, bi or poly, with the main target being the generation new feedstocks with enhanced physicochemical properties, improved conversion efficiency, and thermal properties [27, 28]. In in-situ blending, which is the method for this research, two different WPO are blended to generate another feedstock with a distinct fingerprint from the parent feedstock.

Not many studies on hybridization of used vegetable oil as feedstock are published in literature. In separate researches, Eloka-Eboka and Inambao [27, 28] carried out in-situ and ex-situ mixing of oils and biodiesels from *Moringa oleifera* and *Jatropha curcas* in varying proportions. The new products possess distinct properties from their parent feedstock and methyl esters with the potential to open a new vista in the biofuel industry. The relevant question to ask, therefore, is whether the possibility of hybridization of feedstock in creating new and improved feedstocks has been well interrogated. The objective of this research is to investigate the effects of hybridization of two samples of WPO on the properties, thermal degradation and spectroscopic transformation of the outcome of the hybridization.

Specifically, in-situ hybridization was carried out between two WPO samples that have been utilized to fry different food. The samples were mixed in different proportions and the resulting mixtures were tested and

analyzed. The motivation was to create different sets of feedstocks, which are expected to have different properties and thermal behavior from the parent WPO samples. The scope of the current research was limited to in-situ hybridization of two WPO samples in varying proportions which were then subjected to density, kinematic viscosity, acid value, iodine value, and saponification value testing as well as characterization by thermogravimetric analysis (TGA), derivative thermogravimetric analysis (DTG) and Fourier Transform Infrared Spectroscopy (FTIR).

2. Materials and methods

2.1. Material collection and samples preparation

Two WPO samples were collected from two restaurants in Durban, KwaZulu-Natal Province, South Africa at the point of disposal. One of the WPO samples had been used to fry fish and chips (WPO_{FC}) for 14 days while the second WPO sample was used to fry sausages and chips (WPO_{SC}) for 14 days. The samples were pretreated by subjecting them to heating on an electric stove / magnetic stirrer maintained at 110 °C and stirring speed of 50 rpm to remove the moisture trapped in the oil. The samples were later subjected to vacuum filtration to eliminate food particles, debris, and other foreign bodies in the oil [25]. Figure 2 shows the picture of the parent samples.

The oils were heated to 60 °C and poured into a clean beaker and weighed on an electric weigh balance and poured into a bigger beaker where the oils were mixed in a specified ratio. In the present investigation, simple mixing ratios were adopted in order to prevent undue influence of the one parent sample over the other. The oils in the mixing beaker were stirred with the aid of a magnetic stirrer maintained at a speed of 50 rpm for 20 min to allow for a homogeneous mixture of the oils.

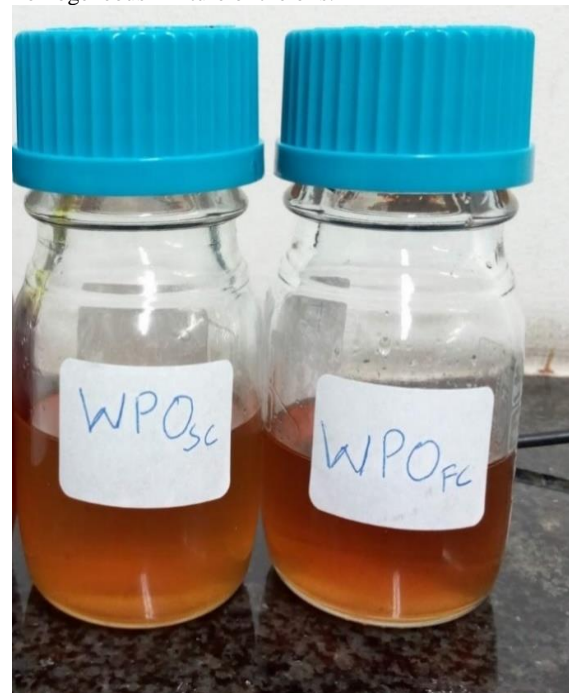


Figure 2: Picture of the parent samples

The hybridized samples are labeled accordingly and stored in airtight glass bottles for property determination

and characterization procedures. The details of the in-situ hybridization are shown in Table 1 while Figure 3 illustrates the flowchart of the methodology. The hybridization protocols are chosen to have different scenarios of mixing the two parent samples WPO_{FC} and WPO_{SC}.

Table 1. Details of the samples and hybridization protocol

Sample notation	Hybridization protocol ratio	
	WPO _{FC}	WPO _{SC}
A	0	1
B	1	0
C	1	1
D	2	1
E	1	2

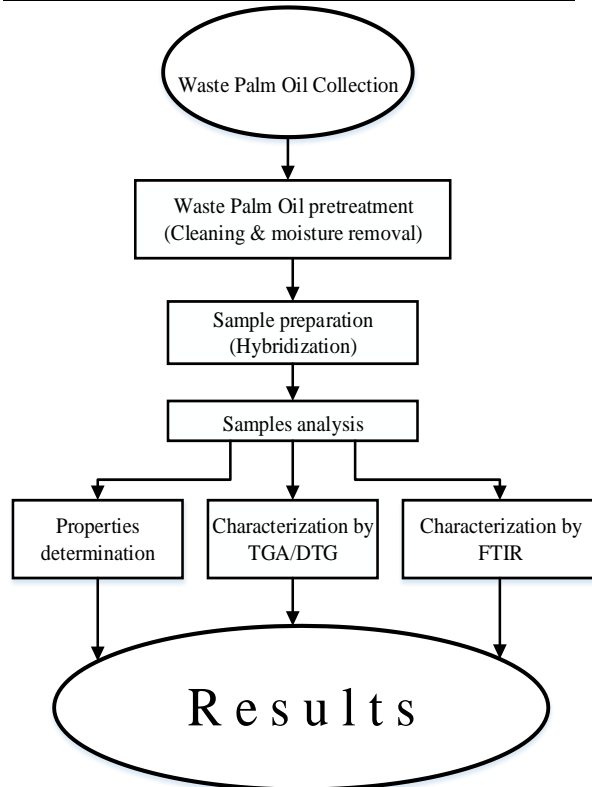


Figure 3. Flowchart of the methodology

2.2. Property determination of samples

The density, kinematic viscosity, acid value, iodine value, and saponification value of the samples were determined by using the appropriate method as shown in Table 2, and the procedures were highlighted in our previous works [18].

Table 2. Methods for properties determination

Property	Unit	Method
Density at 20 °C	Kg/m ³	ASTM D1298
Kinematic viscosity at 40 °C	mm ² /s	ASTM D445
Acid value	mgKOH/g	AOCS Ca 5a-40
Iodine value (IV)	cg/g	AOCS Cd 1b-97
Saponification value (SV)	mg KOH/g	AOCS Cd 3-25
Cetane index (CI)	N/A	By calculation
Higher heating value (HHV)	MJ/kg	By calculation

The CI and the HHV were calculated using the mathematical relations shown in equations 1 and 2.

$$CI = 46.3 + \frac{5458}{SV} - \frac{0.225}{IV} \quad [29]$$

(1)

$$HHV = 49.43 - 0.041(SV) - 0.015(IV) \quad [30]$$

(2)

2.3. Spectroscopic characterization of samples

In order to obtain a recognizable absorption spectrum, the dilution and homogenization of the samples were measured and recorded from 300 cm⁻¹ to 4000 cm⁻¹ on a spectrometer (model system 1000 FTIR, Perkin Elmer Co., USA) with a resolution of 2.0 cm⁻¹.

2.4. Thermal characterization of samples

The TGA/DTG analyses were performed using a DTG-60AH simultaneous DTA-TG apparatus coupled with a TA-60WS thermal analyzer (Shimadzu). The sample weight was about 10 mg, a temperature range of 30 °C to 500 °C, a heating rate of 20 °C/min and a nitrogen flow rate of 50 cm³/min. The data were analyzed by using the TA-60 ch 1 DTG-60AH workstation.

3. Results and Discussions

3.1. Effects on physicochemical properties

The density, kinematic viscosity, acid value, IV, SV, CI, and HHV of the samples are presented in Table 3. The density of the individual parent samples and the hybridized samples are within the same range, though the hybridized samples C, D and E presented slightly lower density than the samples A and B. The kinematic viscosity of the hybridized samples C, D, and E are marginally lower than those of samples A and B. The slight reduction recorded in the values of density and kinematic viscosity can be attributed to the effects of the physical mixing of the parent samples. This conforms with the outcomes of similar work reported in the literature [27, 28]. Rahiman and Santhoshkumar [31] reported that the density of liquid does are not only affected by mixing or blending but also by the temperature. They attributed the variation to the effect of the intermolecular interactions between mixing liquids. The acid value of the samples is not affected by hybridization while the saponification value of the hybridized samples C, D, and E were lower than that of the parent samples A and B. Hybridization lowers the iodine value of the samples when compared with the parent samples. CI and HHV are not affected by hybridization since mixing did not affect the heating capacity of the samples. Since hybridization of the samples took place at room temperature and no chemical reaction was witnessed, the variations in the physicochemical properties of the hybridized samples can only be traced to the effect of the mixing compared with the parent samples.

3.2. Effects on TGA

The outcomes of the TGA examination of the five samples are presented in Figure 3. The TGA plot compares the percentage weight loss of the two-parent WPO samples

with the three hybridized samples concerning the change in temperature. A temperature range of 30 °C to 500 °C was adopted for the five samples. The samples experienced single-stage thermal degradation which starts at around 330 °C for all the samples. With the test temperature differential, sample A, B, C, D, and E witnessed 13 %, 11 %, 10 %, 8 %, and 3 % weight loss, respectively. The thermal degradation commenced at between 320 °C to 330 °C for all the samples. The thermal degradation stopped at 450 °C for samples A, B, C, and D while that of sample E ended at 470 °C. Only the degradation curve for sample E dovetailed into the negative region of the curve. The commencement of the degradation temperature agrees with the outcome of our earlier work [26]. The high degradation temperature was due to the presence of several complex chemical compounds in the samples [32]. Waste cooking oil is susceptible to thermal decomposition at high temperatures as a result of the existence of unsaturated fatty acids which require low thermal energy to break [33-35].

3.3. Effects on DTG

The samples exhibited a similar trend of percentage derivative weight during the thermal degradation process. As shown in Figure 4, the thermal decomposition occurred between 350 °C and 500 °C with each curve presenting a single noticeable peak. The peak in the curves were observed as -0.06 \%m^{-1} at 433 °C for sample A, -0.05 \%m^{-1} at 430 °C for sample B, -0.11 \%m^{-1} at 432 °C for sample C, -0.09 \%m^{-1} at 422 °C for sample D, and -0.06 \%m^{-1} at 430 °C for sample E. During the degradation process, sample C showed the greatest percentage derivative weight, followed by sample D and sample E in that other. This indicates that hybridization slightly influenced the derivative weight percentage and showed that hybridization can produce new sets of feedstocks different from the parent feedstock with the capability of positively influencing biodiesel conversion efficiency [36-38].

Table 3. Properties of the oil samples

samples	Density @ 20°C (Kg/m ³)	Kinematic viscosity @ 40 °C (mm ² /s)	Acid value (mgKOH/g)	Iodine value (cg/g)	Saponification value (mg KOH/g)	Cetane index	Higher heating value (MJ/kg)
A	9188.3	35	1.38	54.4	197.6	73.92	40.51
B	9171.2	34.2	0.97	74.4	199.9	74.30	40.32
C	9150.4	31.7	1.18	89.7	195.9	73.88	39.97
D	9161	30	1.09	92	193	74.58	40.14
E	9169.3	30.8	1.16	86	192	74.72	40.27

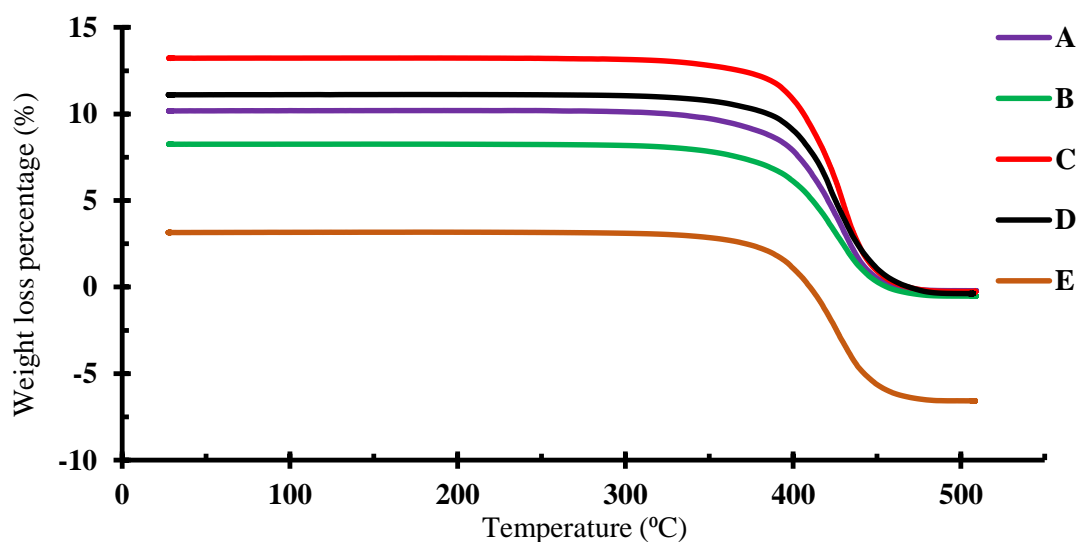


Figure 3. TGA curves for the samples

3.4. Effects on FTIR

The FTIR spectra depicting the functional groups of the five samples are shown in Figure 5. Four regions are identifiable with characteristics peaks in the IR spectrum. The four peculiar regions are distinguishable with characteristic peaks in the FTIR spectrum namely 4000 cm^{-1} to 2500 cm^{-1} , 2500 cm^{-1} to 2000 cm^{-1} , 2000 cm^{-1} to 1500 cm^{-1} , and 1500 cm^{-1} to 400 cm^{-1} are present in the curves. These peaks could be assigned to (C-H) symmetrical, asymmetrical stretching of the saturated carbon-carbon bond, C=O group of triglycerides, and stretching vibrations of the (C-O) esters group. However, the FTIR spectrum in the second region represented by 2500 cm^{-1} to 2000 cm^{-1} is absent in the curves. This is in agreement with the outcome

of similar research as reported in the literature [39, 40]. The five samples have common significant and recognizable peaks at 723 cm^{-1} , 1165 cm^{-1} , 1747 cm^{-1} , 2855 cm^{-1} , and 2924 cm^{-1} indicating the existence of similar chemical groups in the compositions and similar fingerprints [41-43]. However, the parent samples A and B have peculiar peaks at 1226 cm^{-1} , 1363 cm^{-1} , and 1378 cm^{-1} that were found to either disappear or be minimized in the hybridized samples C, D, and E spectrum. The band 1165 cm^{-1} shows the manifestation of methyl esters close to carbonyl groups. The vibration band noticed at 723 cm^{-1} accounts for $\nu(\text{C-H})$ and $\nu(-\text{CH}_2)_n$ functionals. The type of frequencies, functional group, and absorption intensity of the wave numbers noticed in the spectrum are presented in Table 4.

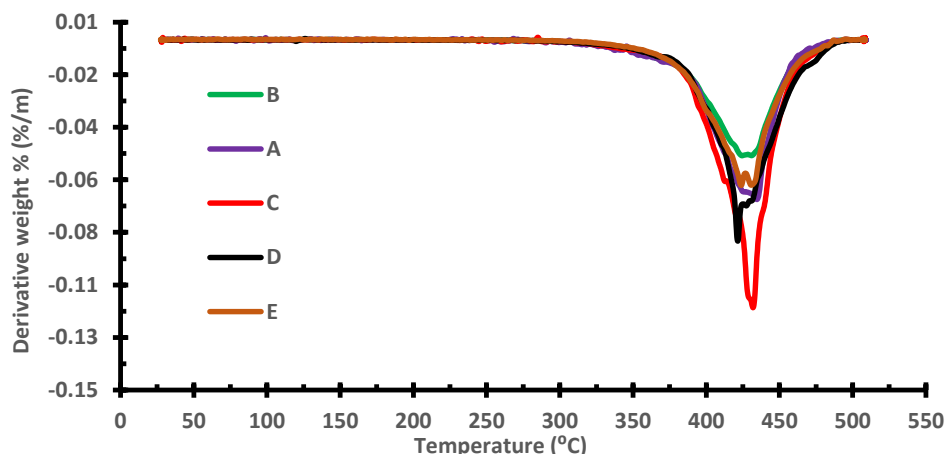


Figure 4. DTG curves for the samples

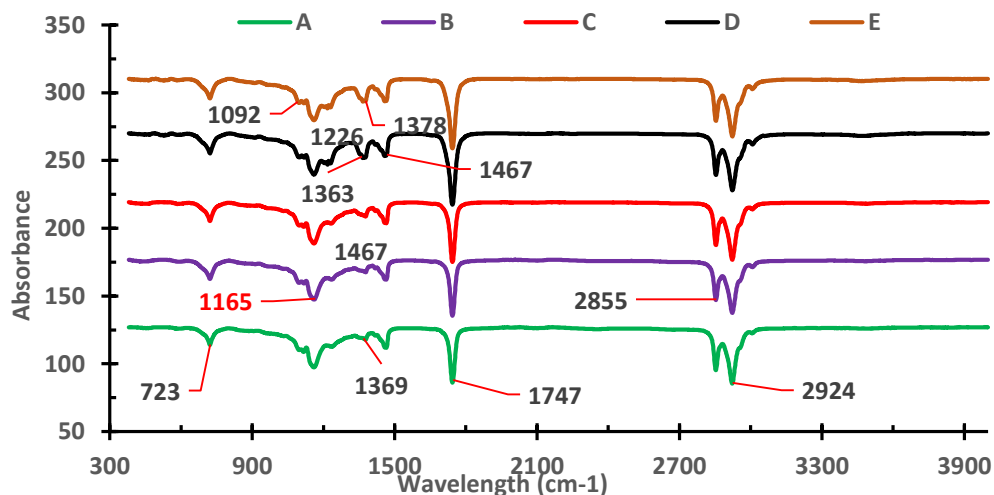


Figure 5. FTIR spectra of the samples

Table 4. Description of the peaks of the spectrum of the samples

Wave number (cm^{-1})	Types of vibration	Functional group	Absorption intensity	Ref
2924	Asymmetrical stretching	C-H of alkanes	Middling	[44]
2855	Asymmetrical stretching	C-H of methylene	Strong	[44]
1747	Stretching	C=O ester band	Strong	[45]
1378	Bending in plane	-C-H(CH_3)	Weak	[46]
1363	Bending	CH_2	Weak	[47]
1165	Stretching, Bending	-C-O, $-\text{CH}_2-$	Strong	[46]
723	Bending	$=\text{C-H}$ and $-(\text{CH}_2)_n$	Weak	[48]

4. Results in Comparison with previous findings

Availability, ease of conversion to biodiesel, and the desire to find an affordable feedstock for biofuel production have triggered interest of researchers in WCO. Among the properties investigated are density, viscosity, saponification value, acid value, fatty acid composition, and iodine value. Table 5 showed outcomes of some of the investigations as published by various authors. When compared with the outcome of this research as shown in Table 3, it can be shown that the properties of WCO are largely dependent on factors such as source of the oil, degree of usage, frying temperature, food used to fry, and hybridization [27, 49].

The Muppaneni et al.[53] , Almazrouei et al.[54], Ullah et al.[52], and Çaylı and Küsefoğlu [55] reported that WCO witnessed one stage thermal degradation. The TGA thermographs showed that thermal decomposition commenced at between 350 °C and 400 °C and were completely decomposed at temperature between 450 °C and 500 °C. This agrees with the outcome of this research. The shapes of the TGA curves were similar to the one shown in Figure 3. The authors attributed the slow thermal degradation of WCO to the high viscosity and molecular tension produced by bulky triglyceride molecule in the oil samples.

The outcome of the DTG characterization as reported by researchers showed that WCO witnessed derivative weight lost at between 350 °C and 500 °C with the peak weight loss of 38.76 % at 414 °C [55]. The thermal and spectroscopic properties of WCO are affected by source of the neat oil, degree of usage, frequency of usage, food items the oil was used to fry.

The outcome of the FTIR characterization by Ullah et al. showed peak vibrations at 2920.30 cm^{-1} , 2851.9 cm^{-1} , and 1743.1 cm^{-1} which are assigned to (C-H) symmetrical, asymmetrical stretching of the saturated carbon-carbon bond, and C=O group of triglycerides respectively. A small band at 1656.69 cm^{-1} resulting from cis C=C bond. The Bands at 1463.79 cm^{-1} resulting from the bending vibrations of CH_2 and CH_3 aliphatic groups were also noticed. Other bands noticed at 1157.19 cm^{-1} and 1116.87 cm^{-1} could be attributed to the stretching vibrations of the (C-O) esters group. These and other similar peaks exhibited by the samples at 2924 cm^{-1} , 2855 cm^{-1} , 1747 cm^{-1} , 1467 cm^{-1} , 1363 cm^{-1} , 1167 cm^{-1} , and 723 cm^{-1} as shown in Figure 5 and described in Table 5. However, to the best of authors knowledge, the effects of hybridization of WCO on TGA, DTG, and FTIR have not been reported.

5. Conclusion

The outcome of the effects of the hybridization of feedstock on the physicochemical properties, thermal characterization, and infrared spectroscopy has been

presented. Hybridization is one of the novel ways of improving the quality of feedstocks. Hybridization of feedstock creates an entirely new feedstock from the existing feedstock with better properties and behavior regarding biodiesel generation. A hybridized feedstock is expected to combine the properties and peculiarities of the parent feedstocks by mixing the parent feedstocks in each ratio. In this research, two samples of WPO were mixed in different ratios and a total of five samples were analyzed by property determination and characterization by TGA/DTG and FTIR. The results of the parent samples were compared with that of the hybridized samples. From the outcome of this research, it is possible to conclude as follows:

1. Apart from the effects of oil source, degree of usage, the food the oil was used to fry, contamination, the frying frequency, the frying temperature, etc on the properties, thermal and spectroscopic properties of WCO, hybridization has a major influence on the physicochemical properties and the characterization behaviour of WCO.
2. Hybridization has no significant effect on the acid value, cetane index, and HHV of the feedstock. However, the density, kinematic viscosity, and saponification value was found to reduce with hybridization while the iodine value of the hybridized feedstock was found to be higher than the iodine value of the individual parent feedstock.
3. TGA and DTG of feedstock are affected by the hybridization of feedstock. The rate of thermal decomposition increases with the mixing of feedstocks, though all the samples witnessed single-stage thermal degradation. The TGA and DTG of both the parent and the hybridized samples occurred within the same temperature range.
4. The FTIR of the parent WPO samples were slightly different from the FTIR of the hybridized samples. Though the five samples A, B, C, D, and E presented similar peaks, the parent samples A and B showed peculiar peaks at 1226 cm^{-1} , 1363 cm^{-1} , and 1378 cm^{-1} which were not noticeable in the spectrum of the hybridized samples.
5. Hybridization of feedstock provides an easy, cheap, and novel way of improving the properties, thermal decomposition, and infrared spectroscopy of feedstocks thereby improving their conversion efficiency to biodiesel.

Going forward, more investigations are needed in in-situ hybridization particularly in mixing more than two different feedstocks at different mixing ratio of feedstocks, more property determination, and characterization techniques. The effects of hybridization of feedstocks on the conversion efficiency, biodiesel fingerprints, combustion, performance and emission characteristics of biodiesel needs to be quantitatively ascertained.

Table 5. Some properties of WCO mined from literature.

Properties	Unit	[49]	[49]	[50]	[51]	[52]
Density	Kg/m^3	904.3	913.4	870	910 – 924	901.3
Kinematic viscosity@ 40 °C	mm^2/s	44.25	38.41	5.03	36.4 – 42	44.956
Saponification value	mgKOH/g	NA	NA	NA	188.2 – 207	177.97
Acid value	mgKOH/g	0.66	1.13	0.29	1.32 – 3.6	4.03
Iodine number	cg/g	81.7	54.2	NA	83 – 141.5	NA

Acknowledgment

The authors are grateful to the;

1. Green Energy Solutions, Discipline of Mechanical Engineering, University of KwaZulu-Natal, Durban for their support.
2. Disciplines of Chemical Engineering and Chemistry, University of KwaZulu-Natal, Durban for permission to use their equipment.

References

- [1] G. Smith. (2019) IEA predicts global oil demand will level off around 2030. Available on <https://www.worldoil.com/news/2019/11/13/iea-predicts-global-oil-demand-will-level-off-around-2030>. *World Oil*.
- [2] S. Thiyagarajan *et al.*, "Effect of manifold injection of methanol/n-pentanol in safflower biodiesel fuelled CI engine," *Fuel*, vol. 261, pp. 116378, 2020, <https://doi.org/10.1016/j.fuel.2019.116378>.
- [3] B. Dhinesh and M. Annamalai, "A study on performance, combustion and emission behaviour of diesel engine powered by novel nano nerium oleander biofuel," *Journal of cleaner production*, vol. 196, pp. 74-83, 2018, <https://doi.org/10.1016/j.jclepro.2018.06.002>.
- [4] D. Balasubramanian, S. R. S. Arumugam, L. Subramani, I. J. Chellakumar, L. J. Stephen, and A. Mani, "A numerical study on the effect of various combustion bowl parameters on the performance, combustion, and emission behavior on a single cylinder diesel engine," *Environmental Science and Pollution Research*, vol. 25, no. 3, pp. 2273-2284, 2018, <https://doi.org/10.1007/s11356-017-0565-2>.
- [5] N. Ahmad *et al.*, "Biodiesel production intensification through microbubble mediated esterification," *Fuel*, vol. 253, pp. 25-31, 2019, <https://doi.org/10.1016/j.fuel.2019.04.173>.
- [6] D. Caldara, M. Cavallo, and M. Iacoviello, "Oil price elasticities and oil price fluctuations," *Journal of Monetary Economics*, vol. 103, pp. 1-20, 2019, <https://doi.org/10.1016/j.jmoneco.2018.08.004>.
- [7] B. Ashok and K. Nanthagopal, "Eco friendly biofuels for CI engine applications," in *Advances in Eco-Fuels for a Sustainable Environment*: Elsevier, 2019, pp. 407-440. <https://doi.org/10.1016/B978-0-08-102728-8.00015-2>
- [8] H. Mahdisoozani *et al.*, "Performance enhancement of internal combustion engines through vibration control: state of the art and challenges," *Applied Sciences*, vol. 9, no. 3, pp. 406, 2019.
- [9] P. Verma *et al.*, "An Overview of the Influence of Biodiesel, Alcohols, and Various Oxygenated Additives on the Particulate Matter Emissions from Diesel Engines," *Energies*, vol. 12, no. 10, pp. 1987, 2019, <https://doi.org/10.3390/en12101987>.
- [10] A. V. Kolhe, R. Shelke, and S. Khandare, "Performance and Combustion Characteristics of a DI Diesel Engine Fueled with Jatropha Methyl Esters and its Blends," *Jordan Journal of Mechanical & Industrial Engineering*, vol. 8, no. 1, 2014.
- [11] R. Ali, S. H. Raheemah, and N. N. Al-Mayyahi, "Numerical Analysis of Combustion Characteristics and Emission of Dual and Tri-Fuel Diesel Engine under Two Engine Speeds," *Jordan Journal of Mechanical & Industrial Engineering*, vol. 14, no. 2, 2020.
- [12] A. Patel, K. Sartaj, P. A. Pruthi, V. Pruthi, and L. Matsakas, "Utilization of Clarified Butter Sediment Waste as a Feedstock for Cost-Effective Production of Biodiesel," *Foods*, vol. 8, no. 7, pp. 234, 2019, <https://doi.org/10.3390/foods8070234>.
- [13] G. Tüccar and K. Aydın, "Evaluation of methyl ester of microalgae oil as fuel in a diesel engine," *Fuel*, vol. 112, pp. 203-207, 2013.
- [14] M. Canakci and H. Sanli, "Biodiesel production from various feedstocks and their effects on the fuel properties," *Journal of industrial microbiology & biotechnology*, vol. 35, no. 5, pp. 431-441, 2008.
- [15] K. R. Jegannathan, C. Eng-Seng, and P. Ravindra, "Economic assessment of biodiesel production: Comparison of alkali and biocatalyst processes," *Renewable and Sustainable Energy Reviews*, vol. 15, no. 1, pp. 745-751, 2011.
- [16] L. P. Oliveira *et al.*, "Biofuel production from Pachira aquatic Aubl and Magonia pubescens A St-Hil: Physical-chemical properties of neat vegetable oils, methyl-esters and bio-oils (hydrocarbons)," *Industrial crops and products*, vol. 127, pp. 158-163, 2019, <https://doi.org/10.1016/j.indcrop.2018.10.061>.
- [17] K. A. Zahan and M. Kano, "Biodiesel production from palm oil, its by-products, and mill effluent: A review," *Energies*, vol. 11, no. 8, pp. 2132, 2018.
- [18] S. Lee, D. Posarac, and N. Ellis, "Process simulation and economic analysis of biodiesel production processes using fresh and waste vegetable oil and supercritical methanol," *Chemical Engineering Research and Design*, vol. 89, no. 12, pp. 2626-2642, 2011.
- [19] S. Sadaf *et al.*, "Biodiesel production from waste cooking oil: an efficient technique to convert waste into biodiesel," *Sustainable cities and society*, vol. 41, pp. 220-226, 2018, <https://doi.org/10.1016/j.scs.2018.05.037>.
- [20] S. B. Živković *et al.*, "Technological, technical, economic, environmental, social, human health risk, toxicological and policy considerations of biodiesel production and use," *Renewable and Sustainable Energy Reviews*, vol. 79, pp. 222-247, 2017, <https://doi.org/10.1016/j.rser.2017.05.048>.
- [21] S. K. Sharma, D. Shukla, K. Khatri, and N. Rajput, "Performance evaluation of diesel engine using biodiesel fuel derived from waste cooking refined soyabean oil," *International Journal of Mechanical and Production Engineering Research and Development (IJMPERD)*, vol. 7, no. 5, pp. 103-110, 2017.
- [22] D. Balasubramanian, S. Kamaraj, and R. Krishnamoorthy, "Synthesis of Biodiesel from Waste Cooking Oil by Alkali Doped Calcinated Waste Egg Shell Powder Catalyst and Optimization of Process Parameters to Improve Biodiesel Conversion," SAE Technical Paper, 0148-7191, 2020.
- [23] M. Shahbandeh, "Vegetable oils: global consumption by oil type 2013/14 to 2019/2020. Available on <https://www.statista.com/statistics/263937/vegetable-oils-global-consumption/>." Accessed on 13 July 2020
- [24] W. N. A. W. Azahar *et al.*, "The potential of waste cooking oil as bio-asphalt for alternative binder—an overview," *Jurnal Teknologi*, vol. 78, no. 4, 2016.
- [25] O. Awogbemi, E. I. Onuh, and F. L. Inambao, "Comparative study of properties and fatty acid composition of some neat vegetable oils and waste cooking oils," *International Journal of Low-Carbon Technologies*, vol. 14, no. 3, pp. 417-425, 2019, <https://doi.org/10.1093/ijlct/ctz038>.
- [26] O. Awogbemi, E. I. Onuh, and C. A. Komolafe, "Thermal Degradation and Spectroscopic study of Neat Palm Oil, Waste Palm Oil, and Waste Palm Oil Methyl Ester," in *IOP Conference Series: Earth and Environmental Science*, 2019, vol. 331, no. 1: IOP Publishing, pp. 012032 <https://doi.org/10.1088/1755-1315/331/1/012032>.
- [27] A. C. Eloka-Eboka and F. L. Inambao, "Hybridization of feedstocks—A new approach in biodiesel development: A case of Moringa and Jatropha seed oils," *Energy Sources, Part A: Recovery, Utilization, and Environmental Effects*, vol. 38,

- no. 11, pp. 1495-1502, 2016
<https://doi.org/10.1080/15567036.2014.934413>.
- [28] A. Eloka-Eboka and F. Inambao, "Blending feedstock—Fresh approach in biodiesel development: Moringa and Jatropha seed oils," in *Twenty-Second Domestic Use of Energy*, 2014: IEEE, pp. 1-8 <https://doi.org/10.1109/DUE.2014.6827771>.
- [29] K. Krisnangkura, "A simple method for estimation of cetane index of vegetable oil methyl esters," *Journal of the American Oil Chemists' Society*, vol. 63, no. 4, pp. 552-553, 1986.
- [30] D. Ayhan, "Biodiesel a realistic fuel alternative for diesel engines," , 2008. London: Springer-Verlag. <https://doi.org/10.1007/978-1-84628-995-8>
- [31] M. K. Rahiman and S. Santhoshkumar, "Comparative studies of oxygenated fuel synthesis with diesel from the measurements of density, speed of sound and refractive index," *Journal of Thermal Analysis and Calorimetry*, vol. 136, no. 1, pp. 295-304, 2019, <https://doi.org/10.1007/s10973-018-7828-0>.
- [32] G. Çaylı and S. Küsefoğlu, "Increased yields in biodiesel production from used cooking oils by a two step process: Comparison with one step process by using TGA," *Fuel Processing Technology*, vol. 89, no. 2, pp. 118-122, 2008.
- [33] F. D. Gunstone, *Vegetable oils in food technology*. Wiley Online Library, 2002.
- [34] B. Fife, *The palm oil miracle*. Piccadilly Books, Ltd., 2007.
- [35] B. Yang, "Feature proof natural vitamin e: Activities and sources," *Lipid Technology*, 2003.
- [36] H. Li, S. Niu, C. Lu, and Y. Wang, "Comprehensive investigation of the thermal degradation characteristics of biodiesel and its feedstock oil through TGA–FTIR," *Energy & Fuels*, vol. 29, no. 8, pp. 5145-5153, 2015.
- [37] S. Niu, Y. Zhou, H. Yu, C. Lu, and K. Han, "Investigation on thermal degradation properties of oleic acid and its methyl and ethyl esters through TG-FTIR," *Energy Conversion and Management*, vol. 149, pp. 495-504, 2017, <https://doi.org/10.1016/j.enconman.2017.07.053>.
- [38] H. Li, S.-I. Niu, C.-m. Lu, and S.-q. Cheng, "Comparative evaluation of thermal degradation for biodiesels derived from various feedstocks through transesterification," *Energy Conversion and Management*, vol. 98, pp. 81-88, 2015, <https://doi.org/10.1016/j.enconman.2015.03.097>.
- [39] D. Michael. "How to Read IR Spectrums." Sciencing, 2017 <https://sciencing.com/read-ir-spectrums-6809192.html>.
- [40] J. McMurry, *Organic chemistry*. Belmont, CA: Thomson Brooks/Cole, 2008.
- [41] P. Nautiyal, K. Subramanian, and M. Dastidar, "Experimental investigation on performance and emission characteristics of a compression ignition engine fueled with biodiesel from waste tallow," *Clean Technologies and Environmental Policy*, vol. 19, no. 6, pp. 1667-1677, 2017, <https://doi.org/10.1007/s10098-017-1355-8>.
- [42] Y. Isah, A. Yousif, K. Feroz, Y. Suzana, A. Ibraheem, and A. Soh, "Comprehensive Characterization of Napier Grass as Feedstock for Thermochemical Conversion" *Energies.com/journal/energies*, vol. 8, pp. 3403-3417, 2015.
- [43] D. Sebayang, E. Agustian, and A. Praptijanto, "Transesterification of biodiesel from waste cooking oil using ultrasonic technique," 2010.
- [44] Silverstein R.M, Bassler G.C, and Morrill T.C, *Spectrometric Identification of Organic Compounds*, 5th edition ed. New York, United States, Wiley, 2014.
- [45] M. Y. Talpur *et al.*, "Application of multivariate chemometric techniques for simultaneous determination of five parameters of cottonseed oil by single bounce attenuated total reflectance Fourier transform infrared spectroscopy," *Talanta*, vol. 129, pp. 473-480, 2014, <https://doi.org/10.1016/j.talanta.2014.04.002>.
- [46] S. Y. Lim, M. S. Abdul Mutalib, H. Khaza'ai, and S. K. Chang, "Detection of fresh palm oil adulteration with recycled cooking oil using fatty acid composition and FTIR spectral analysis," *International Journal of Food Properties*, vol. 21, no. 1, pp. 2428-2451, 2018, <https://doi.org/10.1080/10942912.2018.1522332>.
- [47] M. Elkady, A. Zaatout, and O. Balbaa, "Production of biodiesel from waste vegetable oil via KM micromixer," *Journal of Chemistry*, 2015.
- [48] A. Rohman, Y. B. Che Man, P. Hashim, and A. Ismail, "FTIR spectroscopy combined with chemometrics for analysis of lard adulteration in some vegetable oils espectroscopia FTIR combinada con quimiometría para el análisis de adulteración con grasa de cerdo de aceites vegetales," *Cyta-Journal of Food*, vol. 9, no. 2, pp. 96-101, 2011.
- [49] O. Awogbemi, F. Inambao, and E. I. Onuh, "Effect of usage on the fatty acid composition and properties of neat palm oil, waste palm oil, and waste palm oil methyl ester," *International Journal of Engineering and Technology*, vol. 9, no. 1, pp. 110-117, 2020.
- [50] A. B. Chhetri, K. C. Watts, and M. R. Islam, "Waste cooking oil as an alternate feedstock for biodiesel production," *Energies*, vol. 1, no. 1, pp. 3-18, 2008, <https://doi.org/10.3390/en1010003>.
- [51] M. A. Raqeeb and R. Bhargavi, "Biodiesel production from waste cooking oil," *Journal of Chemical and Pharmaceutical Research*, vol. 7, no. 12, pp. 670-681, 2015.
- [52] Z. Ullah, M. A. Bustam, and Z. Man, "Characterization of waste palm cooking oil for biodiesel production," *International Journal of Chemical Engineering and Applications*, vol. 5, no. 2, pp. 134, 2014.
- [53] T. Muppaneni, H. K. Reddy, and S. Deng, "Supercritical synthesis of ethyl esters via transesterification from waste cooking oil using a co-solvent," *Journal of Environmental Protection*, vol. 6, no. 09, pp. 986, 2015, <https://doi.org/10.4236/jep.2015.69087>.
- [54] M. Almazrouei, S. Elagroudy, and I. Janajreh, "Transesterification of waste cooking oil: Quality assessment via thermogravimetric analysis," *Energy Procedia*, vol. 158, pp. 2070-2076, 2019, <https://doi.org/10.1016/j.egypro.2019.01.478>.
- [55] G. Çaylı and S. Küsefoğlu, "Increased yields in biodiesel production from used cooking oils by a two step process: Comparison with one step process by using TGA," *Fuel Processing Technology*, vol. 89, pp. 118-122, 2008, <https://doi.org/10.1016/j.fuproc.2007.06.020>.

Design and Analysis of Permanent Mould for Small Internal Combustion Engine Piston

Olurotimi Akintunde Dahunsi^a, Olatunji Oladimeji Ojo^{b,*}, Ikeoluwa Ogedengbe^a,
Omeiza Bayode Maliki^a

^aMechanical Engineering Department, Federal University of Technology, P. M. B. 704, Akure, Ondo State, Nigeria

^bIndustrial and Production Engineering Department, Federal University of Technology, P. M. B. 704, Akure, Ondo State, Nigeria

Received June 5 2020

Accepted November 7 2020

Abstract

The lack of electrical power supply in African homes has led to a quantum proliferation and usage of portable backup power alternatives like generators. The ceaseless running of generators makes most homes to overshoot the recommended service life (approximately 150 hours) and maximum continuous runtime (4 - 6 hours) of generators in the earliest possible time. Burnout of piston and its eventual impairment consequently ensue, and this gives room for endless replacements of piston and incessant piston wastes. To manage piston waste, and to create a sustainable piston market, the outlook of reproducing piston from its wastes is engineered. As a result, this work examines the conceptual permanent mould design, thermal analysis and fabrication of the designed mould, and casting of 950 Watts generator's piston. The mechanical and microstructural properties of the as-cast pistons were correlated with the properties of LM13. Defect-free pistons were produced while the re-melting process slightly altered the composition of the as-cast alloy as compared to that of LM13.

© 2020 Jordan Journal of Mechanical and Industrial Engineering. All rights reserved

Keywords: Permanent Mould, Mould Design, Piston, Casting, Mechanical properties; Aluminum alloy;

1. Introduction

The performance of pistons is critical to the overall output of internal combustion (I.C.) engines. Therefore, pistons must possess good strength and heat resistance properties [1]. The continuous operation of pistons beyond the recommended service life impairs their thermal bearing capacity and degrades their wear resistance capabilities. This situation is prevalent in the under-developed nations where electricity generation by state or public companies is poor, thereby, causing the citizens to run personal generating units for long time. The accumulation of extracted pistons from these units produces a disturbing pile of scrap pistons and creates a good opportunity for recycling.

Pistons receive an impulse from expanding gas and transmits the established energy to the crankshaft via the connecting rod. Pistons run at high speeds and work under high temperature, pressure, and fatigue stresses [2]. A piston's work environment is also corrosive which predisposes it to wear. The heat generated during the reciprocating action of the piston in the combustion chamber is dispersed through the piston to the cylinder walls [3]. Consequently, the continuous reciprocating motion of the piston generates severe stresses on the piston crown, sidewall, and the piston's ring. Therefore, there is a need for the piston construction and material to guarantee good strength, toughness, corrosion resistance, resistance to

abrasive wear, and less fracture susceptibility [4]. The piston must also be light while presenting a good ratio of tensile strength to mass density [5]. Rao et al. [6] reported that the introduction of Al-1Ti-3B and P (as grain refiners), and Sr (as modifier) to the hyper-eutectic Al-15Si-4Cu alloy promotes the formation of CuAl₂ particles (at the interdendritic regions) and this attribute improves the wear resistance of the cast alloy. The studies of Reghu et al. [7] revealed that the application of thermal barrier coating on the Al-Si piston alloy enhances combustion (within the combustion chamber of diesel engines), and improves performance and piston life.

The most commonly used materials for piston production are cast iron, cast aluminum, forged aluminum, cast steel, and forged steel. The wide usage of Al-Si alloys as piston materials has been attributed to their desirable characteristics such as good thermal conductivity, high strength over weight ratio, high strength at elevated temperatures, excellent castability, and improved wear resistance [8]. The pistons for high-speed engines are primarily made of aluminum alloys which contain about 11–13% silicon and approximately 1% each of copper, nickel, and magnesium. As a result, typical pistons of automobiles and generators are cast from near eutectic Al-Si alloys or LM13 Al alloys [9] [10]. This class of aluminum alloy exhibits complex multi-phase microstructures which usually comprise of primary and eutectic Si, Al, and several intermetallic particles [11]. Chemical composition and microstructural features, such as eutectic Si particles,

* Corresponding author e-mail: ojuoladimeji90@yahoo.com.

intermetallic compounds, and morphologies of dendritic α -Al (or secondary dendritic arm spacing) are factors that influence the mechanical properties of Al-Si cast alloys. However, casting technology remains the commonest means of improving the mechanical properties of these (aluminum-silicon) alloys [12].

Zhang et al. [13] compared the high pressure die casting and permanent mold casting of the Al-Si-Cu-Ni-Mg alloy. It was revealed that the cast from the high-pressure die casting process produced a higher tensile strength after thermal exposure. El-Labban et al. [14] employed a squeeze casting procedure to produce cast Al-Si piston alloy reinforced with Ni and nano-Al₂O₃ particles. The addition of Ni and nano-Al₂O₃ to the constituent of the alloy improved the resultant ultimate tensile strength of the cast piston. Ni particles were affirmed to be responsible for the improved ductility. Characterization undertaken by Zhang et al. [15] showed a fractographic appearance of automotive piston material (heavily alloyed Al-Si alloy) after tensile rupture. Cleavage or brittle fracture being reported as the failure mode of the piston under tension loading condition. Fracture of Si particle within the piston matrix was observed to have promoted the formation of cleavage facets and several secondary cracks. Meanwhile, the studies of Divya and Gopal [16] revealed that Al-Si pistons produced low deformation and equivalent strain values as compared to aluminum pistons.

Recent studies show an increasing interest in the reproduction of Al-Si pistons from scraps [17] [18]. Defected pistons and undesirable results have been attributed to the casting processes such as sand casting. There is a need to investigate the self-support casting process which can achieve reproducibility of pistons without the need for the preparation of mould at each casting time. This work presents a permanent piston mould design with a non-destructive core for 950 Watts generators and examines the thermal analysis of the designed mould. The development of the designed mould and casting of pistons were carried out to evaluate the effectiveness of the designed mould.

2. Methods

2.1. Permanent Mould Design

Fig. 1 shows the normal dimensions of a typical 950W generator. The mould material, requisite allowances, in-gate system design (dimensions), and morphology of riser are identified as the most central factors in the piston mould design. Equally, the hollow profile of the interior section or core of the piston requires careful consideration and design.

Based on manufacturers' specifications, pistons are made from Al-Si alloys and the liquidus temperature or the melting point of Al-Si alloys is usually about 530-660 °C. Thus, the appropriate melting and pouring temperature for the Al-Si alloy cast is adjudged to be greater than its liquidus temperature to ensure homogeneous melting, non-slurry molten metal, and cold shut defect-free cast. A pouring temperature range of 700 - 750 °C is chosen because this is the optimized temperature for Al-Si cast [19] and above this temperature, the vaporization of alloying constituents has a chance of occurring.

The choice of material for the casting process is vital because the chosen mould material is expected to withstand the high molten temperature of Al-Si alloy (700-750 °C). Materials with melting temperatures twice that of pure aluminum were considered to be suitable for the casting process. Mild steel was selected as the mould material (having a melting range of 1350°C-1530°C). The thermal/temperature simulation of the mould is investigated in Section 2.2. Based on the availability of the required thermomechanical properties of AISI 1065 carbon steel (with a melting point of 1460°C), the AISI 1065 carbon steel was employed for the mould simulation in this paper. The melting points of these steel alloys (AISI 1065 and mild steel) are relatively similar.

2.1.1. Mould Geometry (Piston Cavity)

The mould geometry is designed to take the form shown in Fig. 1 which is without the ring grooves because the grooves are expected to be machined afterward, to produce the standard piston dimensions. However, other allowances are built into the standard piston specification to avoid the production of undersized piston cast. The requisite allowances needed for the mould design include shrinkage, machining, and draft allowances. The allowances employed based on Narayanan [20] are given in Table 1.

Machining allowance (M_a) for non-ferrous metals with dimensions up to 203.2 mm is given as 2.29 mm. The diameter (D) and length (H) of the piston to be produced are 45 and 50 mm respectively. Likewise, to facilitate easy removal of the solid core from the cast piston, draft allowance (D_a) is incorporated into the core length of the piston. The diameter of the piston core is 40.0 mm and its depth is 47.0 mm. The draft angle for metal with a height between 25.4 - 50.8 mm is 1°; thus, this angle (D_a) is employed for the piston core.

The molten metal or cast is expected to undergo the following contractions or shrinkages: liquid shrinkage (a contraction of the liquid metal before solidification), liquid-to-solid/solidification shrinkage (shrinkage that occurs as crystals begin to form in the molten cast), and solid shrinkage (the final contraction that emerges as the solid metal casting cools to ambient temperature). For the permanent mould design, liquid shrinkage is considered to be negligible due to its minimal effect on volumetric cast while solidification (liquid-to-solid) and solid shrinkages are adjudged to be extremely important and must thus be considered in the casting design. Metals have different percentages of solidification and solid shrinkages. As a result, the shrinkage percentage (S_p) of non-ferrous alloys is adopted as the shrinkage allowance (S_a) for the Al-Si alloy (piston). According to Narayanan [20], the shrinkage allowance (S_a) in percentage for Al-Si alloy is provided as 1.29%. Thus, the shrinkage allowances (S_a) for the piston's diameter (D) and length (H) are estimated using Eq. 1 and Eq. 2 respectively. The estimated diameter and length allowances are 0.37 and 0.68 mm respectively.

$$S_{a-W} = \frac{1.29}{100}(D + M_a) \quad (1)$$

$$S_{a-L} = \frac{1.29}{100}(H + M_a) \quad (2)$$

Where S_{a-W} and S_{a-L} are the designations for shrinkage allowances for the diameter and length of the piston. Also, the designed mould diameter (D_m) and mould length (H_m)

for the piston are estimated via Eq. 3 and Eq. 4 respectively. The computed mould diameter and length are 48.0 and 53.0 mm respectively.

$$D_M = D + M_a + S_{a-w} \tag{3}$$

$$H_M = H + M_a + S_{a-L} \tag{4}$$

The mould is designed to be of two symmetrical halves (split mould) with one half fixed and the other movable to facilitate easy removal of the cast piston. Representations of the designed split-half (mould) are shown in Fig. 2. Machining of a block of mild steel is employed for the fabrication of the mould. The thickness of the mould is continuous/kept constant throughout the mould's geometry

to aid even heat suction or sink. Likewise, the mould is designed to be supported by other features such as mould base, clamping bolts, lock nuts, and turn-handle to aid easy assembly and disassembly of the two halves of the mould.

Table 1. Allowances built into the piston mould design

Allowance	Value
Machining allowance (M_a)	2.29 mm
Draft allowance (D_a)	1°
Shrinkage allowance for diameter (S_{a-w})	0.37 mm
Shrinkage allowance for length (S_{a-L})	0.68 mm

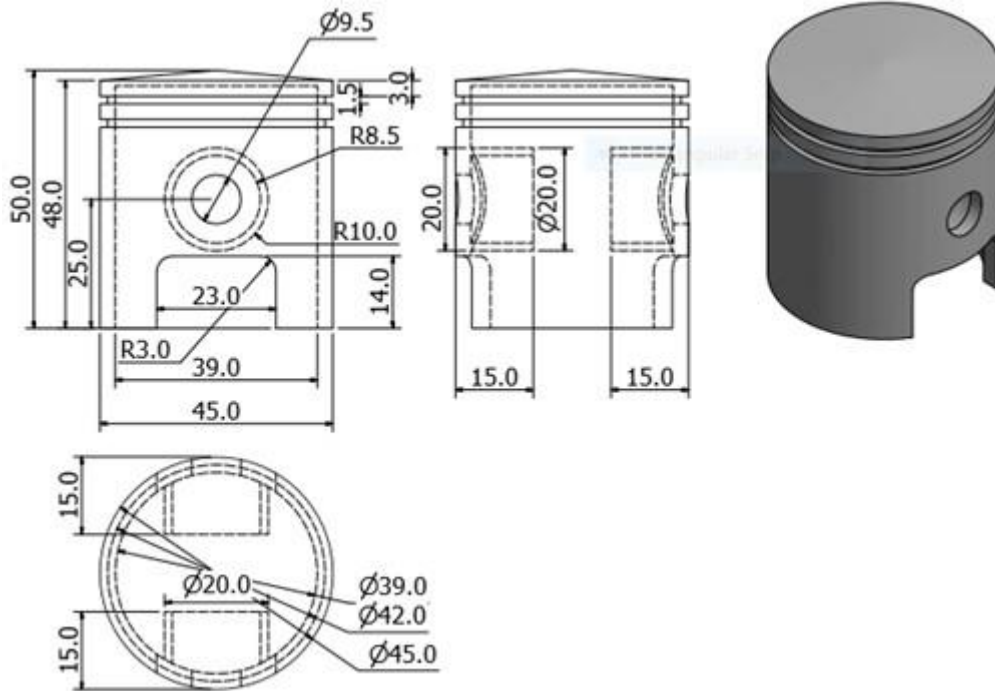


Figure 1. Standard dimensions (mm) of a 950 W electric power generator piston

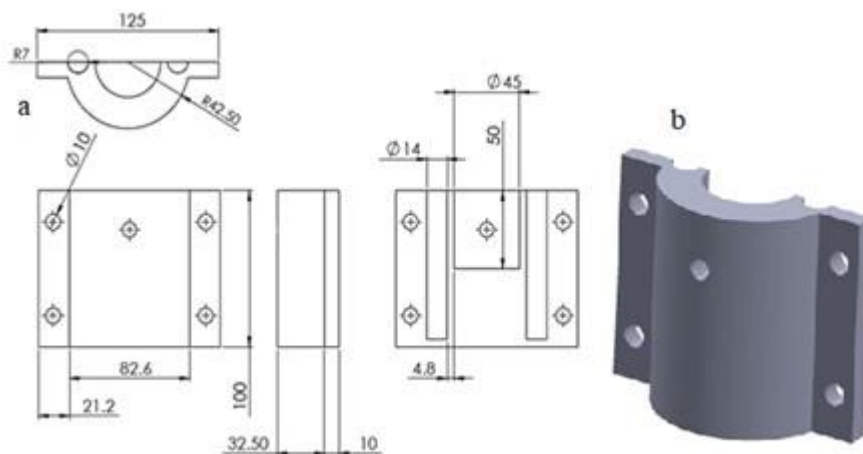


Figure 2. Mould half (split mould) (a) projection views; (b) isometric drawing

2.1.2. In-gate system design

The main purpose of the gating system is to direct the flow of the molten metal into the mould cavity. The gating system for the piston mould comprises of the following components: pouring basin; sprue; runner; and in-gate.

The pouring basin is otherwise known as the funnel-top and it is the point of entry where molten metal is first received in a designed mould before the entry of the molten metal into the sprue. The sprue is the tapered cylindrical section of the molten metal entry gate which controls the rate of the entry (of molten metal) into the mould (runner, in-gate, and cavity). The channel designed for the distribution of molten metal from the sprue to different regions in the casting is referred to as the runner. The runner also controls the velocity or flow rate of the molten metal into the mould. The point of metal entry into the actual casting or mould cavity is referred to as in-gate. Good quality of a cast or homogeneous mould filling has been adjudged to be dependent on a proper gating system design [21] and the gating system design needs to follow an iterative process [22]

The sequential steps employed in designing the gating system for the piston cast involve:

1. Estimation of optimum pouring time of casting,
2. Calculation of sprue choke area
3. Selection of gating ratio
4. Selection of the type of gating/location
5. Calculation of runner and in-gate sizes

The pouring time (t) is considered to be dependent on fluidity and dross-forming characteristics of the Al-Si alloy. The total weight of the casting or the casting geometry can as well influence the pouring time required for the piston casting. Based on this understanding, the pouring time is estimated from Eq. 5. Increasing casting speed or reduced pouring time has been adjudged to be an effective way to eliminate shrinkage porosity defect as revealed in the works of Jie et al. [23].

$$t = \frac{W_m}{M_{fr}} \quad (5)$$

Where t is the pouring time, W_m is the total weight of the casting or weight of the metal to be poured and M_{fr} is the metal flow rate of Al-Si alloy at 700-750°C. The sprue choke area of the ingate system is estimated by using Eq. 6 [24].

$$A = \frac{G}{c \cdot \rho \cdot t \cdot \sqrt{2gh}} = 29.59 \text{ mm}^2 \quad (6)$$

Where A is the sprue choke area (sprue exit area), G is the casting gross weight (cavity, piston, and runner) = 0.1738 Kg, c is the discharged coefficient which is 0.4 for thin-wall casting, ρ is the density of the Al-Si base alloy (2500 kg/m³), t is the pouring time (4.07 s), h is the metallostatic height from the ladle to the choke area (104 mm) and g is the acceleration due to gravity (9.81 m/s²). The in-gate area was estimated as 49.22 mm² via Eq. 7 while the in-gate diameter was approximately 8 mm. The transition between the sprue exit area and the in-gate (that is the runner) must be designed to reduce metal velocity. Thus, the runner of a 10 mm diameter was chosen for the design because the cross-section of the runner should be greater than that of the sprue exit area.

$$A_{\text{sprue-exit}} = \frac{A_{\text{sprue-inlet}} \sqrt{H_{\text{sprue-exit}}}}{\sqrt{H_{\text{sprue-inlet}}}} \quad (7)$$

Where $A_{\text{sprue-inlet}}$ is the sprue inlet cross-sectional area, $A_{\text{sprue-exit}}$ is the sprue exit cross-sectional area, $H_{\text{sprue-inlet}}$ is the distance between the ladle and sprue top and $H_{\text{sprue-exit}}$ is the distance between ladle and sprue exit. A side gating type/location was chosen for this design due to the mould type, casting wall thickness, and weight of metal required to enter the mould.

2.1.3. Riser design

A riser is needed to accommodate the liquid shrinkage and to supply feed metal to compensate for the solidification shrinkage during the casting process. The volume of the riser should be greater than that of the in-gate to ensure that casting solidifies before the riser [25]. According to Chvorinov's Rule, the mathematical relationship between the solidification time for a simple casting, the volume, and surface area of the casting is provided as shown in Eq. 8 [25] [26].

$$T_{TS} = C_m \left(\frac{V}{A}\right)^n \quad (8)$$

Where T_{TS} is the total solidification time in min, V is the volume of the casting, A is the surface area of the casting, n is an exponent usually taken to be 2 in value, C_m is the mould constant which is dependent on the mould material, thermal properties of the cast metal and pouring temperature.

The mould constant (C_m) is determined from the piston's mould cavity. The T_{TS} is expected to be less than 1.5 minutes. The volume and the surface area of the piston are estimated according to Eq. 9 and Eq. 10 respectively. The mould constant is thus estimated by employing Eq. 8. This mould constant is also applicable to that of the riser. The volume and surface area of the riser (it is assumed to be cylindrical) are determined via Eq. 11 and Eq.12 respectively.

$$V_c = V_{mc} - V_{cc} + V_l + V_r \quad (9)$$

$$A_c = A_{mc} - A_{cc} + A_l + A_r \quad (10)$$

$$V_r = \frac{\pi d^2 h}{4} \quad (11)$$

$$A_r = \pi d h + \frac{2\pi d^2}{4} \quad (12)$$

Where V_c is the total cast volume, V_{mc} is the volume of the mould cavity, V_{cc} is the volume of the core, V_l is the volume of the sprue/in-gate, and V_r is the volume of the riser (in Eq. 9 and Eq. 10). Also, V_r is the volume of a cylindrical riser, A_r is the surface area of a cylindrical riser, d is the diameter of the riser, h is the height of the riser (see Eq. 11 and Eq.12). The height of the riser is twice the diameter of the riser ($h = 2d$). Therefore, the modulus of the riser is given as Eq. 13. The diameter of the riser is thus estimated as the product of the modulus of the riser and five (5) units. Based on the condition of freezing, the ratio of the inverse modulus of the casting to the inverse modulus of the riser should be greater than unity or $M_r : M_c > 1$ (where, M_c is the modulus of the casting). The $M_r : M_c$ is taken to be 1.2 ($M_r = 1.2M_c$) to satisfy the condition of freezing (freezing ratio) in this design. Thus, the diameter of the riser (d) is estimated as 10 mm using Eq. 13 when M_c is 1.6.

$$M_r = \frac{V_r}{A_r} = \frac{d(2d)}{4(2d)+2d} = \frac{d}{5} \quad (13)$$

The designed permanent mould with its support structures is shown in Fig. 3. The supports provided are integrated into the permanent mould to aid handling and

easy removal of cast piston via the turning handle after solidification.

2.2. Thermal simulation of the designed mould

Based on the designed mould in Section 2, the thermal gradient of the mould around the piston core is simulated. The modeled geometries of the mould and its core were drafted using 3D CAD Design Software (Solidworks) for analysis in COMSOL Multiphysics Software (simulation package). The meshing of geometries and boundary condition assignments were carried out before the post-processing (simulation) of the mould. The triangular tetrahedral element was selected as the element type for the halves of the mould and the piston core as indicated in Figs. 4 and 5 respectively.

The components were discretized and the numbers of elements of the movable mould half and piston core were 32050 and 8460 respectively. Since the mould is asymmetrical, the movable half of the mould is considered and simulated to save time. The employed mould material is AISI 1065 carbon steel (UNS G10650) which has a density of 7.85 g/cm³; the chemical composition and mechanical properties of the alloy are shown in Tables 2 and 3 respectively.

The reference temperature for the study was pre-set at 273.15 K while the entire body of the mould was insulated to ensure the visibility of temperature distribution across the bulk matrix of the mould and piston core upon subjection to high-temperature molten metal. The temperature of the molten metal for the casting was set as 800 oC. Basic governing laws of thermodynamics apply to the simulation process. The generalized governing differential equation for

heat conduction in the permanent mould can be represented as given in Eq. 14 [28-30]

$$K\nabla^2T + q_E - \rho C \frac{\delta T}{\delta t} = 0 \tag{14}$$

Where *K* is the thermal conductivity in the radial and axial direction of the mould, *q_E* is the heat conduction per unit volume, *ρ* is the density of the mould material, *C* is the heat capacity of the mould material, *T* is temperature and *t* is time.

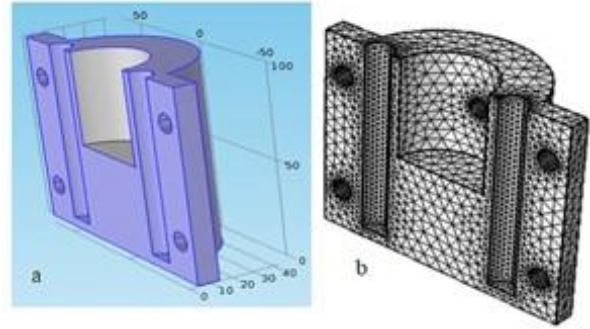


Figure 4. Cast piston permanent mould on (a) Movable half of mould; (b) discretized mould

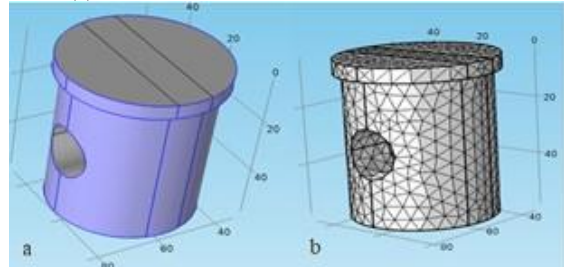
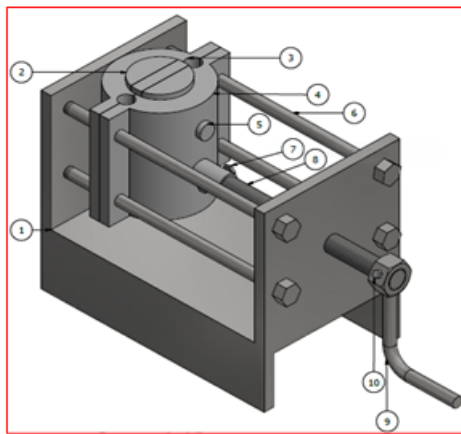
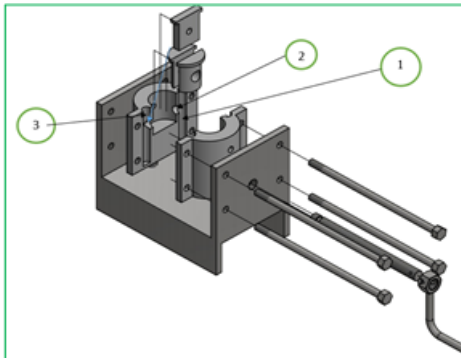


Figure 5. Geometry of the piston core (a) unmeshed core; (b) discretized/meshed core



Parts list		
Part number	Qty	Item
11	1	Lock nut
10	1	Lock bolt
9	1	Turning handle
8	1	Clamping bolt
7	2	Locating bolt
6	4	Guide bolt
5	1	Gudgeon pin
4	2	Side mould
3	2	Inlet hole for molten metal
2	3	Core components
1	1	Mould base



Part list		
Part number	Qty	Item
3	1	runner
2	1	Ingate
1	1	riser

Figure 3. An assembled model of the permanent mould

Table 2. Chemical composition of AISI 1065 steel [27]

Element	Fe	Mn	C	S	P
Content	98.31 - 98.8	0.60 - 0.90	0.60 - 0.70	0.05	0.04

Table 3. Mechanical properties of AISI 1065 steel [27]

Tensile strength (MPa)	Yield strength (MPa)	Elongation	Hardness (Brinell)
635	490	10%	187

3. Results and discussion

3.1. Thermal analysis of mould and core

Heat flows or temperature distributions in the mould and the piston core are examined at various times or durations as indicated in Figs. 6, 7, and 8. The results show that heat transfer increases with time from the mould cavity to the external surface of the mould due to the inherent thermal/temperature disparity (between the core and the surface of the mould). A progressive heat transfer from the mould cavity/core ensues in the mould to attain thermal equilibrium. This occurrence is expected to facilitate the cooling process during the casting process.

Figs. 6 and 7 describe the thermal response of the mould when molten material is introduced into it. The assessment of the volume and surface temperature distributions across the mould shows a relatively similar pattern. As a result, the surface temperature distribution was used in the description of results in this study. The progress and pattern of the heat flow or temperature distribution from inside the mould are studied. The surface temperature distribution shows that the choice of the mould material (steel) permits satisfactory thermal dissipation as the external surface temperature of the mould rises from room temperature to about 640 K after the post-pouring time of 60 s. This observation corroborates the higher thermal conductivity of the AISI 1065 mould material (49.8 W/mK) [27] as compared to that of a sand mould. The highest temperature appears at the mould interior/cavity at the beginning of the casting process and it progressively rises towards the mould's exterior/external surface via a conductive heat transfer mode. Although there is a big range of temperature distribution between the interior and external surfaces of the mould at the beginning of casting, the temperature gap closes down as the post-pouring time increases to establish thermal equilibrium. The rate of conductive heat transfer in the mould is influenced by the temperature difference between the interior part and the external surface of the mould.

The thermal transfer distances across the mould at different post-pouring times are revealed in the contour thermal plots (sectional views) of the mould provided in Fig.7. Fig. 7 shows that thermal dissipation through the sharp edges (corners) of the mould is not as pronounced as the body of the mould without geometrical changes as the post-pouring time increases. The width of the yellow coloration (590 - 680 K) is narrower at the corner of the mould after the post-pouring time of 60 s. This occurrence may be likely attributed to geometrical variations which could bring about constriction of contour lines and an eventual narrow temperature range of 590 - 680 K in the

mould. The obtained result corroborates the findings of Rafique and Iqbal [31] as heat transfer patterns were reported to be strongly dependent upon the mould geometry and wall thickness.

On the other hand, the thermal dissipation in the core of the mould is revealed in Fig. 8. This shows that the core acted as a form of the heat sink on receiving the molten metal of the Al-Si alloy. The bulk of the heat/temperature of the molten metal is transferred to the mould as the post-pouring time increases. Evidence of this occurrence is revealed on the external surface of the core as rapid cooling appears on the core as the post-pouring time increases. The lower surface area of the core as compared to that of the mould cavity may be responsible for the faster cooling of the piston's core due to a direct relationship exists between the rate of heat transfer and surface area.

3.2. Casting result

The designed mould was fabricated via various machining processes and the produced mould was employed for casting 950 Watts pistons. The Al-Si alloy scraps were melted in an open-hearth furnace set at a temperature of 720 °C. The molten alloy was stirred to ensure a homogeneous mixture and degassing of the melt was carried out by using the powder of CCl₄. The melt was poured into the mould after preheating the mould to a temperature of about 200 °C.

Twelve metal pours were carried out and four of them had misruns (incompletely filled mould cavity), which could have been caused by the backpressure effect of the mould cavity. However, the as-cast pistons had a slightly rough surface appearance owing to the machining-induced roughness within the mould cavity. Samples of the as-cast pistons showing the attached risers and in-gate profiles are shown in Fig. 9. These attachments (riser and in-gates) were knocked off via the use of a hammer to commence the fettling process on the as-cast piston. The machining of the as-cast pistons to standard sizes and the cutting of oil grooves and pin diameter were carried out on the lathe and drilling machines respectively. The machining process was carried out at high spindle speeds and low feed rates to improve the surface appearance of the as-cast piston. This combination of machining parameters has been reported by Gharaibeh et al. [32] to promote a better surface finish. No palpable solidification-induced defect was found on the surfaces of the machined samples as smooth surface appearances were obtained. Samples of the machined pistons are provided in Fig. 10.

The microstructure of the as-cast piston was prepared according to metallurgical standards, etched with Keller's reagent, and viewed under an optical microscope. The microstructure of the as-cast piston shows no visible proof of micro- and macro-pores as revealed in Fig. 11. The designed in-gate system of the permanent mould could be adjudged to have accommodated adequate venting and consequently produced defect-free as-cast pistons. However, the magnifications of the notable areas on the microstructure (see Fig. 11) show evidence of dendritic solidification as dendrites are formed within the fine grains of the alloy. The adequate thermal dissipation attribute of the mould facilitates a rapid cooling cycle which reduces the

size of dendrites and dendritic arm spacing in the solidified as-cast pistons. The high solidification/cooling rate of the Al melt has been reported to aid the reduction of dendritic arm spacing (SDAS), the modification of eutectic Si, and the refinement of solidification-induced intermetallic phases [33]. These are desirable attributes that influence the mechanical properties of as-cast Al alloy. Thus, it can be concluded that the permanent mould was able to satisfactorily produce as-cast pistons. The suitability of the produced pistons for the harsh service conditions was not covered in the scope of this work but the elemental compositions of the as-cast piston showed a very close comparison with that of LM13 as revealed in Table 4.

Based on LM Chart 2017, LM13 is the major ASTM classification of aluminum alloy used for internal combustion engines' pistons. The little variation in the composition of the as-cast alloy with LM13 (see Table 4) may be because of the re-melting/recycling process or the influence of the as-manufactured compositional variation of the individual scrap piston. Thus, the introduction of little percentage weight of the deficient alloying elements (such as Mn, Ni, Zn, and Ti) into the re-melted Al-Si piston scrap is recommended to bring the composition of the as-cast

piston into par with that of LM13. Besides, Table 5 shows the appraisal of the mechanical properties of the as-cast pistons and the LM13. The average tensile strength and hardness of the as-cast piston are 15% and 9% lesser than those of the LM13 respectively. The slight deficit in the weight percentages (wt%) of Mn, Ni, Zn, and Ti in the as-cast piston (see Table 4) could be responsible for the observed results (tensile strength and hardness) in Table 5. Shehadeh and Jalham [34] revealed that the addition of Mn (< 0.6 wt%) to Al alloy increases the tensile properties and hardness of the as-cast Al alloy. Thus, the addition of about 0.29 wt% Mn with other elements (such as Ni, and Ti) to the as-cast piston alloy is adjudged to be capable of improving the tensile and hardness values of the as-cast piston. On the other hand, the as-cast sample exhibited significant improvement in elongation under monotonic axial loading as compared to that of LM13. This occurrence may be attributed to the reduced dendrite sizes in the structure of the as-cast samples owing to the significant thermal dissipation away from the cast into the mould after a few seconds of pouring. Smaller dendrites are notable for producing higher ductility in metals.

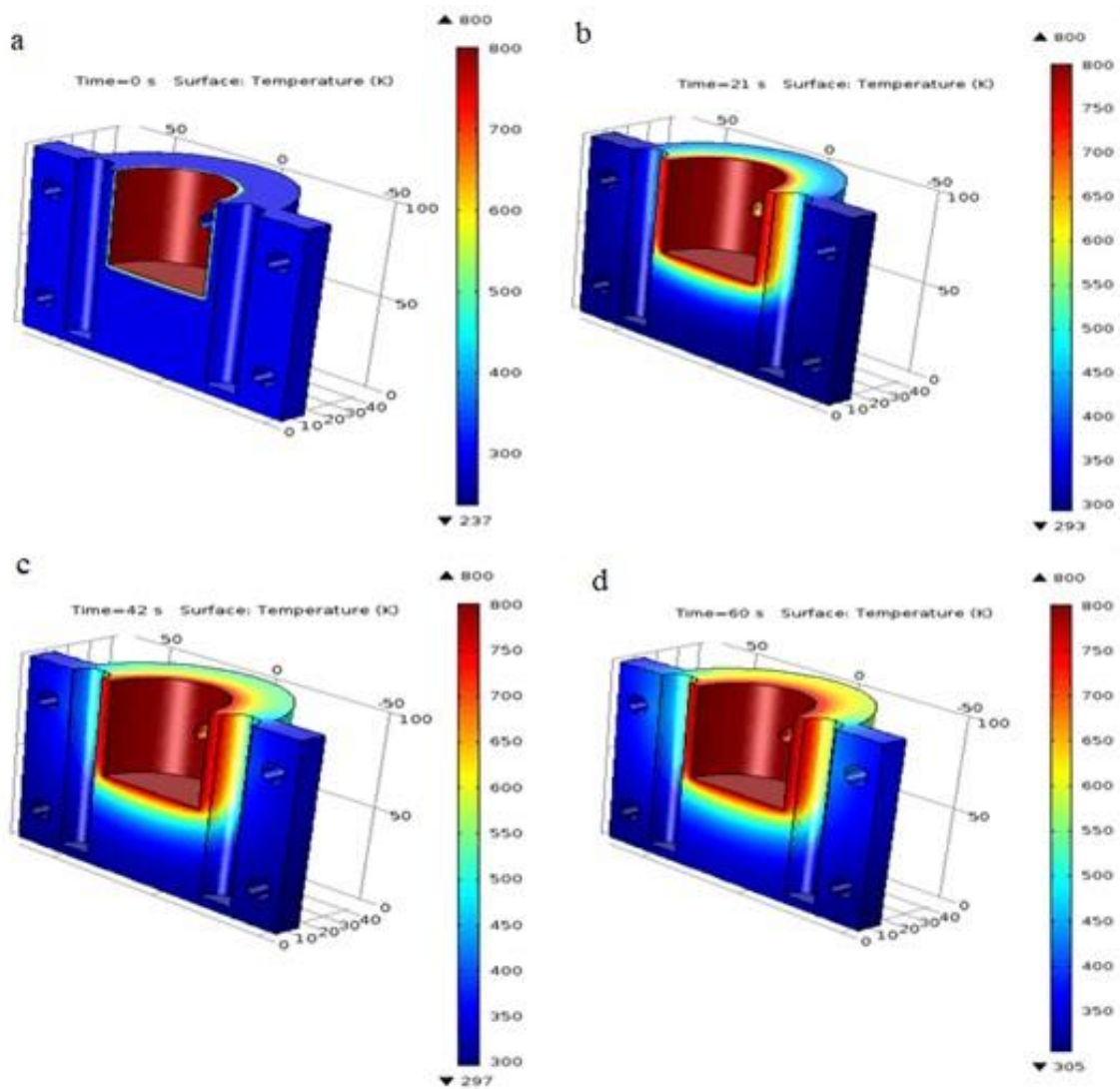


Figure 6. Surface temperature distribution in the movable mould at different times (a) 0 s time; (b) 21 s time; (c) 42 s time and (d) 60 s time

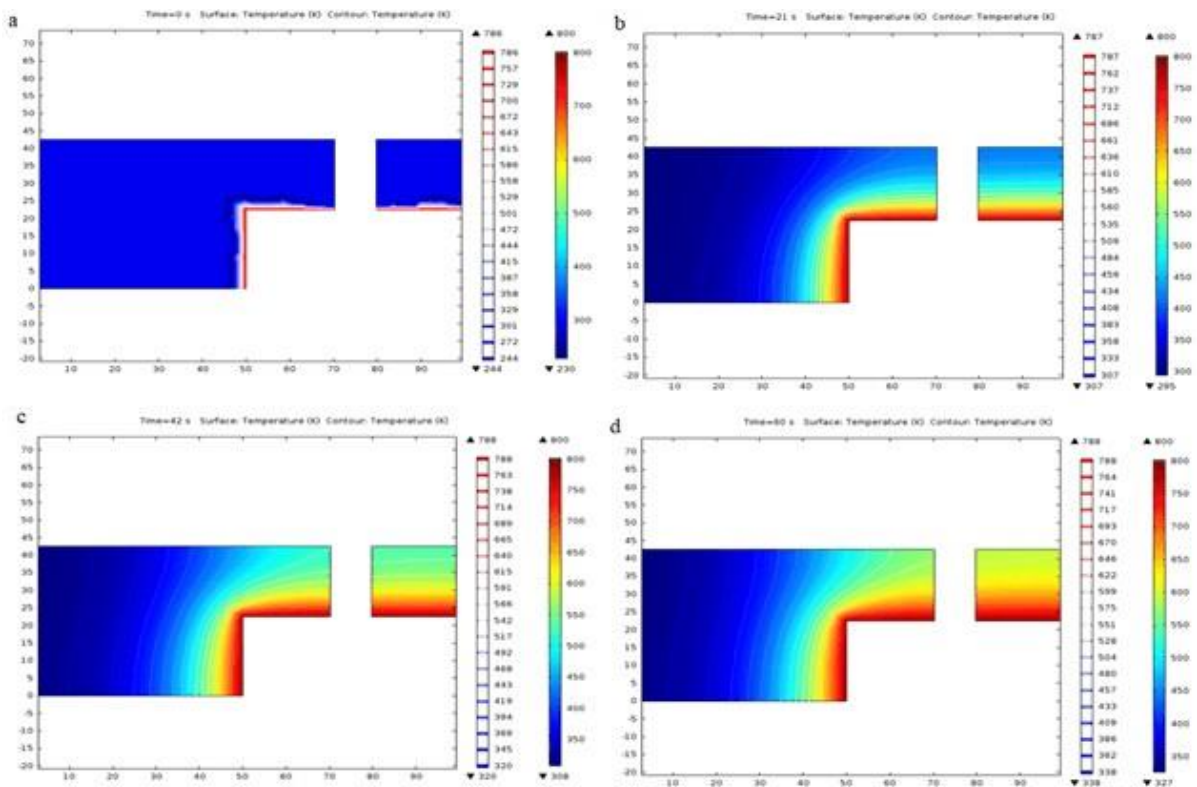


Figure 7. Thermal plot through the central section of the mould at different times (a) 0 s time; (b) 21 s time, (c) 42 s time, and (d) 60s time

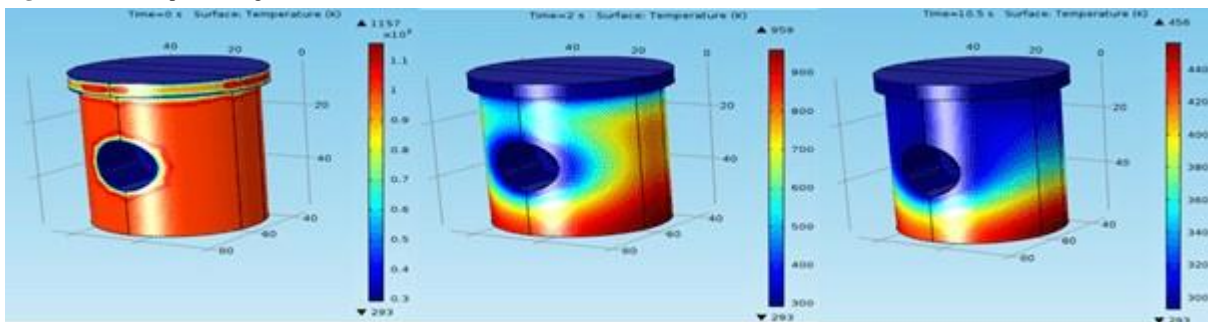


Figure 8. Surface temperature distribution around the piston core at different times (a) 0 s time; (b) 2 s time and (c) 10.5 s time



Figure 9. Unmachined cast pistons



Figure 10. Machined cast pistons

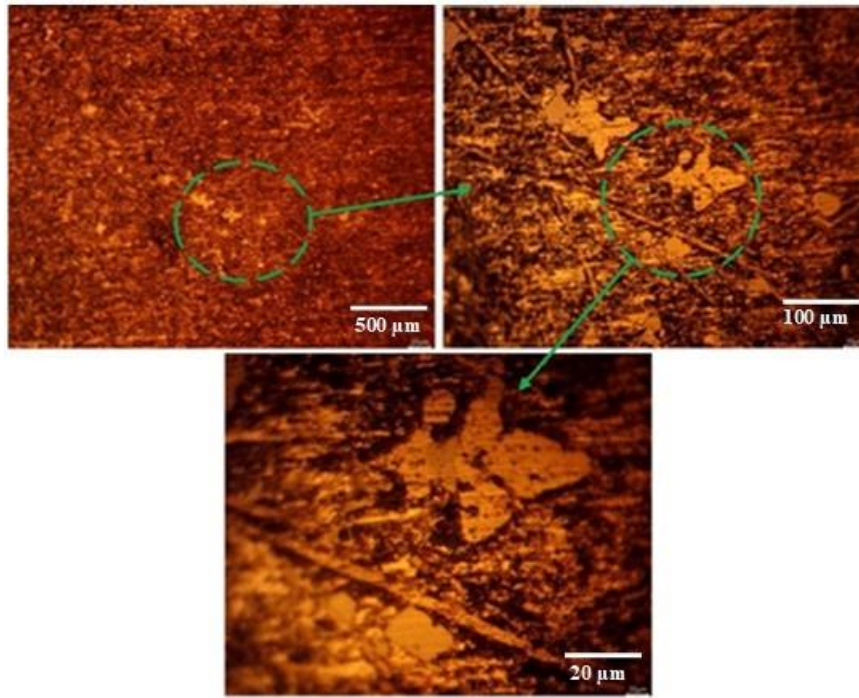


Figure 11. Microstructure of the as-cast piston

Table 4. Chemical compositions of as-cast piston and LM13 (wt%)

Elements	Cu	Mg	Si	Fe	Mn	Ni	Zn	Pb	Sn	Ti	Al	Sr	Cr
As-cast 1	1.94	2.20	14.35	2.28	0.22	0.86	0.22	0.03	0.10	0.05	77.62	0.02	0.02
As-cast 2	1.77	1.93	13.49	2.45	0.21	0.86	0.23	0.05	0.08	0.04	78.75	0.01	0.06
As-cast 3	1.52	2.22	13.06	1.49	0.17	0.85	0.22	0.02	0.05	0.04	80.26	0.01	0.01
LM13	1.40	1.50	13.00	1.00	0.50	1.50	0.50	0.50	0.10	0.20	79.80	-	-
Recom.			***		Add	Add	Add		***	Add	***		

Note: "Recom." means recommendation; "Add" means elemental addition; "****" implies relatively close wt%

Table 5. Comparative mechanical properties of the as-cast sample and LM13 alloy

Mechanical Properties	Values of the LM13 Alloy [35]	Values of the AS-Cast Piston Alloy
Tensile Strength (MPa)	200	170
Elongation %	0.5	1.417
Hardness (VHN)	130	118

4. Conclusions

The detailed design of a permanent mould for casting 950 Watts pistons was carefully carried out and the thermal analysis of the mould was investigated by using COMSOL Multiphysics Software. The development of the mould was carried out and the casting of 950 Watts pistons from the Al-Si piston scraps was successfully carried out. The success of this research work has opened up a window for the recycling of aluminum scraps as a means of managing piston scraps, and an avenue for wealth creation. The major findings of this work are as highlighted below:

1. The temperature simulation results show that the use of steel mould allows satisfactory thermal dissipation during the casting process.
2. The appearance of the as-cast piston is slightly rough due to the machining-induced roughness on the mould

cavity. However, no inherent matrix defect is found in the microstructure of the as-cast piston at a pouring temperature of 720°C.

3. The microstructure of the as-cast piston predominantly consists of solidification-induced dendrites and fine grain structures. The re-melting of the Al-Si piston scraps slightly alters the composition of the as-cast alloy when compared with that of LM13
4. The average tensile strength and hardness of the as-cast piston are 15 and 9% lesser than the properties of the LM13 respectively due to the slight composition variation between the as-cast and the LM13 alloys.

Further studies on the improvement of the properties of the as-cast piston (from piston scraps) via elemental additions are part of the authors' future research plans.

Conflict of Interests

The authors declare that there is no conflict of interest regarding the publication of this work.

References

- [1] A. Ahmed, M.S. Wahab, A.A. Raus, K. Kamarudin, Q. Bakhsh, D. Ali, "Mechanical Properties, Material and Design of the Automobile Piston: An Ample Review". *Indian Journal of Science and Technology*, Vol. 9, No. 36, 2016, 1-7
- [2] S. Lombardo, I. Peter, M. Rosso, "Gravity Casting of Variable Composition Al Alloys: Innovation and New Potentialities". *Materials Today: Proceedings*, Vol. 10, 2019, 271–276
- [3] H. Pandey, A. Chandrakar, "Computer-Aided Modeling and Simulation of IC Engine Speculative Piston". *International Journal of Innovations in Engineering and Technology*, Vol. 4, 2014, 30-36.
- [4] R. Subbarao, S. V. Gupta, "Thermal and structural analyses of an internal combustion engine piston with suitable different superalloys". *Materials Today: Proceedings*, Vol. 22, 2020, 2950–2956
- [5] A.W. Orłowicz, M. Tupaj, M. Mróz, A. Trytek, "Combustion Engine Cylinder Liners Made of Al-Si Alloys". *Archives of Foundry Engineering*, Vol. 15, 2015, 71-74.
- [6] P.V. C. S. Rao, A. S. Devi, K.G. B. Kumar, "Influence of Melt Treatments on Dry Sliding Wear Behavior of Hypereutectic Al-15Si-4Cu Cast Alloys". *Jordan Journal of Mechanical and Industrial Engineering*, Vol. 6 (1), 2012, 55-61
- [7] V.R. Reghu, N. Mathew, P. Tilleti, S. V. P. Ramaswamy, "Thermal Barrier Coating Development on Automobile Piston Material (Al-Si alloy), Numerical Analysis and Validation". *Materials Today: Proceedings*, Vol. 22, Vol. 2020, 1274–1284
- [8] J. Kumar, D. Singh, N. S. Kalsi, S. Sharma, C. I. Pruncu, D. Y. Pimenov, K. V. Rao, W. Kapłonek, "Comparative study on the mechanical, tribological, morphological and structural properties of vortex casting processed, Al–SiC–Cr hybrid metal matrix composites for high strength wear-resistant applications: Fabrication and characterizations". *Journal of Materials Research Technology*, Vol. 9(6), 2020, 13607-13615
- [9] B.N. Yadav, D. Muchhala, A. Abhash, P. Singh, R. Kumar, D.P. Mondal, "Fabrication of ultra-light LM13 alloy hybrid foam reinforced by MWCNTs and SiC through stir casting technique". *Materials Letters*, Vol. 279, 2020, 128271
- [10] M. Goenka, C. Nihal, R. Ramanathan, P. Gupta, A. Parashar, J. Joel, "Automobile Parts Casting-Methods and Materials Used: A Review". *Materials Today: Proceedings*, Vol. 22, 2020, 2525–2531
- [11] M. Azadi, H. Bahmanabadi, F. Gruen, G. Winter, "Evaluation of tensile and low-cycle fatigue properties at elevated temperatures in piston aluminum-silicon alloys with and without nano-clay-particles and heat treatment". *Materials Science & Engineering A*, Vol. 788, 2020, 139497
- [12] G. Chirita, D. Soares, F.S. Silva, "Advantages of the centrifugal casting technique for the production of structural components with Al-Si alloys". *Materials and Design*, Vol. 29, 2008, 20-27.
- [13] J.-Y. Zhang, L.-J. Zuo, J. Feng, B. Ye, X.-Y. Kong, H.-Y. Jiang, W.-J. Ding, "Effect of thermal exposure on microstructure and mechanical properties of Al–Si–Cu–Ni–Mg alloy produced by different casting technologies". *Trans. Nonferrous Met. Soc. China*, Vol. 30, 2020, 1717–1730
- [14] H.F. El-Labban, M. Abdelaziz, E.R.I. Mahmoud, "Preparation and characterization of squeeze cast-Al–Si piston alloy reinforced by Ni and nano-Al₂O₃ particles". *Journal of King Saud University - Engineering Sciences*, Vol. 28, 2016, 230–239.
- [15] G. Zhang, J. Zhang, B. Li, W. Cai, "Characterization of tensile fracture in heavily alloyed Al–Si piston alloy". *Progress in Natural Science: Materials International*, Vol. 21, 2011, 380-385.
- [16] M.S. Divya, K.R. Gopal, "Design and Material Optimization of the Piston by using PRO E and ANSYS". *International Journal of Advanced Scientific Technologies in Engineering and Management Sciences*, Vol. 2, 2016, 14-20.
- [17] F.U. Ozioko, "Casting of Motorcycle Piston from Aluminium Piston Scrap using Metallic Mould". *Leonardo Electronic Journal of Practices and Technologies*, Vol. 21, 2012, 82-92.
- [18] S.O. Adeosun, E.I. Akpan, D. Abiodun, "Mould Temperature and Mechanical Properties of Cast Aluminum-Silicon Carbide Composite". *International Journal of Materials and Chemistry*, Vol. 3, 2013, 75-83.
- [19] M.B. Ndaliman, P.A. Pius, "Behavior of Aluminum Alloy Castings under Different Pouring Temperatures and Speeds". *Leonardo Electronic Journal of Practices and Technologies*, Vol. 11, 2007, 71-80.
- [20] R.G. Narayanan, *Metal casting Processes*, Indian Institute of Technology Gawahati [Internet] Available: <https://www.slideshare.net/anjanpatel1/metal-casting-processes-89647585> [Accessed on 10th August 2017].
- [21] B.H. Hu, K.K. Tong, X.P. Niu, I. Pinwill, "Design and optimization of runner and gating systems for the die casting of thin-walled magnesium telecommunication parts through numerical simulation". *Journal of Materials Processing Technology*, Vol. 105, 2000, 128-133.
- [22] S.H. Wu, J.Y.H. Fuh, K.S. Lee, "Semi-automated parametric design of gating systems for die-casting die". *Computers & Industrial Engineering*, Vol. 53, 2007, 222–232.
- [23] Z. Jie, Z. Dongqi, W. Pengwei, W. Gang, L. Feng, D. Penglong, "Numerical Simulation Research of Investment Casting for TiB₂/A356 Aluminum Base Composite". *Rare Metal Materials and Engineering*, Vol. 43, 2014, 0047-0051.
- [24] A.K.M.B. Rashid, *Design of Gating and Feeding Systems* [Internet]. Available: <http://foundrygate.com/upload/artigos/K3ePtMbZRtz4gRWO TfVVjj3gbKc7.pdf> [Accessed: 20th September 2017].
- [25] S. Santhi, B.R. Surya, S. Jairam, J. Jhansi, P.K.S. Subramanian, "Design of Gating and Riser System for Gate Bar Casting". *Indian Foundry Journal*, Vol 61, 2015, 19-23.
- [26] M.P. Groover, *Fundamentals of modern manufacturing materials, processes, and systems*. 3rd ed. John Wiley and Sons, Inc., 2007.
- [27] AZO Materials. *AISI 1065 Carbon Steel (UNS G10650)* [Internet] Available: <https://www.azom.com/article.aspx?ArticleID=6575> [Accessed: 16th October, 2017].
- [28] S.K. Sharma, P.K. Saini, N.K. Samria, "Experimental Thermal Analysis of Diesel Engine Piston and Cylinder Wall". *Journal of Engineering*, 2015, 1-10.
- [29] H. Wang, G. Djambazov, K.A. Pericleous, R.A. Harding, M. Wickins, "Modelling the dynamics of the tilt-casting process and the effect of the mould design on the casting quality". *Computers & Fluids*, Vol. 42, 2011, 92–101.
- [30] S.M.H. Mirbagheri, M. Shrinparvar, A. Chirazi, "Modeling of metalo-static pressure on the metal–mould interface thermal resistance in the casting process". *Materials and Design*. Vol. 28, 2007, 2106–2112.
- [31] M.M.A. Rafique, J. Iqbal, "Modeling and simulation of heat transfer phenomena during investment casting". *International Journal of Heat and Mass Transfer*, Vol. 52, 2009, 2132–2139.
- [32] N. Gharaibeh, M. AlAjlouni, A. Al-Rousan, "Olive Mill Wastewater as Cutting Fluids: Effect on Surface Roughness of Aluminum". *Jordan Journal of Mechanical and Industrial Engineering*, Vol. 12(3), 2018, 161 – 166
- [33] R. Chen, Q. Xu, H. Guo, Z. Xia, Q. Wu, B. Liu, "Correlation of solidification microstructure refining scale, Mg

- composition and heat treatment conditions with mechanical properties in Al-7Si-Mg cast aluminum alloys". *Materials Science and Engineering: A*, Vol. 685, 2017, 391-402
- [34] L. M. Shehadeh, I. S. Jalham, "The Effect of Adding Different Percentages of Manganese (Mn) and Copper (Cu) on the Mechanical Behavior of Aluminum". *Jordan Journal of Mechanical and Industrial Engineering*, Vol. 10 (1), 2016, 19-26
- [35] G.B. Mallikarjuna, K.V.S. Rao, R.H. Jayaprakash, "Preparation and Property Evaluation of Aluminium-Silica Composites by Casting Route". *International Journal of Mechanical engineering and Robotics*, Vol. 1, 2012, 118 – 124.

Adaptive Disturbance Estimation and Compensation for Delta Robots

Iyad Hashlamon

Mechanical Engineering Department, Palestine Polytechnic University, Hebron, Palestine

Received March 14 2020

Accepted November 22 2020

Abstract

This paper introduces an adaptive disturbance estimation and compensation approach for delta parallel robots using three methods. The first method is based on the adaptive Kalman filter (AKF), the second method uses the Low pass filtered robot dynamic model (LFDM) while the third method is acceleration measurement based (AMB) method which utilizes the measured moving platform acceleration directly into the robot dynamical model. The considered disturbance is joint friction, uncertainty and unmodeled dynamics, their effects are represented as lumped disturbance torque vector. The estimation performance is evaluated using the mean square error (MSE) as a performance measure. To control the robot, the nonlinear robot model is linearized using feedback linearization through the estimated disturbance which is adaptively scaled using an adaptive tuning gain to overcome the limitations of the transient response of the estimated disturbance. The tuning is governed by a simple developed sliding surface depending on the error between the desired and actual joint angles. The tuned disturbance is added directly to the classical proportional-derivative (PD) controller output control signal for disturbance compensation and trajectory tracking. Based on the results, a comparison among the three methods is studied. The comparison shows that the AKF method is the most accurate that tracks the desired trajectory in the presence of disturbance and noise. The other methods are not recommended.

© 2020 Jordan Journal of Mechanical and Industrial Engineering. All rights reserved

Keywords: Delta robot, adaptive Kalman filter, disturbance estimation, adaptive control;

1. Introduction

Parallel manipulator usage has been increased dramatically in industrial applications and attracted the academicians to conduct researches on design and control of these robots. Comparing this type of robots with serial robots, they have advantages in terms of light weight, high accuracy and repeatability, high stiffness, easy inverse kinematics computing, force distribution and short cycle times. Therefore, this type of robots is used in many applications that require high speed and acceleration, repeated work and accuracy such as: pick and place [1, 2], intelligent sorting systems [2, 3], 3D printing [4], food manufacturing systems [5], hybrid robot interaction [6] and many others [7, 8]. However, compared with serial robots, the computation of parallel robots forward kinematics is complicated and the dynamic model is challenging which complicates the implementation of some control algorithms such as inverse dynamic control and classical Proportional- integral derivative (PID) controllers [9]. More precisely, the dynamical model of the three degrees of freedom DoF Delta robot is composed of three dynamic nonlinear equations with three restriction equations.

Several classical control approaches were applied to match the desired performance and trajectory tracking [10-14]. The computed torque controllers require the full robot dynamic model. The unmodeled dynamics, joint friction, disturbances and model uncertainty deteriorate the

controller performance [15]. PD and PID controllers are used to control delta robots [16]. The design principle neglects the coupling effects, thus the response is affected by the disturbance due to the structure of the robot and requires improving the tracking errors for robust and smooth response [17]. Joint friction has significant importance in terms of steady state error, limit cycles and poor dynamic response [18, 19]. Although friction has been represented by mathematical models [20-23], it is environment and load dependent. This increased the challenge to develop control approaches for joint friction compensation [24-28]. The structure of the Delta robot increases the difficulty to have an adaptive and a robust response. This paper will consider the unmodeled nonlinear coupled dynamics, model uncertainty and joint friction as lumped disturbance torque vector to be estimated and compensated.

Disturbance observers were used for disturbance estimation and compensation for robotic manipulators [29, 30]. These observers require knowledge of how to tune the observer gain. The active disturbance rejection control (ADRC) with linear disturbance observation and linear feedback control techniques are used for trajectory tracking tasks in parallel robots [9]. The estimation in the ADRC depends on the extended state observer [31]. This observer is regularly of high gain and requires a tuning process that avoids undesired high gain effects, such as peaking [32], instabilities or noisy estimations [33]. To overcome this limitation, an adaptive observer is used with a varying gain to form an adaptive active disturbance

* Corresponding author e-mail: iyad@ppu.edu.

rejection for robust trajectory tracking [34]. Many of the adaptive controllers of manipulators with dynamic uncertainty are Lyapunov -based [35, 36]. Lyapunov-based controllers focus more on stability and less on performance and require parameter tuning which is difficult. Recent nonlinear PD with sliding mode control was reported in [37]. However, sliding mode controller's major problem is chattering. The research on adaptive control of delta robot is still ongoing [38] to restrain model uncertainties problems. For a detailed comparison refer to [39].

This paper introduces an online adaptive disturbance estimation and compensation using three methods and compares among them. The first estimation method uses the adaptive Kalman filter AKF [40, 41] to estimate this disturbance. The structure of the AKF is recursive and considers the noise due to uncertainty and measurement noise and projects their effect on the filter gain. This gain is tuned adaptively depending on the estimation error. This filter is adaptive, i.e. it is unnecessary to know the statistics of the noise since it has two tuned updating rules for the noise covariance according to the estimation performance. The second method adopts the filtered dynamic model approach. The dynamic model of the robot contains the joint angular acceleration which is unmeasured or hard to be measured directly. This challenge is solved by filtering the dynamic model of the robot. The result of this method is a filtered version of the disturbance. This method is called low-pass filtered dynamic model LFDm. The third method is acceleration measurement based method AMB. This method assumes the availability of a three axes-accelerometer attached to the moving platform of the robot to measure its acceleration, then this measured acceleration is utilized in the robot model to estimate the disturbance.

The estimated disturbance will have transient response and overshoot. This will reduce the tracking performance of the controller. Therefore, to overcome this transient response, namely the overshoot, the estimated disturbance is adaptively tuned. A simple adaptive tuning gain surface is developed depending on the error between the actual and desired joint angles. This gain scales the estimated disturbance adaptively. In the steady state, the tuning gain effectiveness is decreased dramatically i.e. has a value of one or close to one. The tuned disturbance is added to the control signal of the classical PD controller to study the tracking trajectory performance. The proposed control approach shows that the adaptive disturbance estimation using AKF along with the PD controller result in smooth tracking of the desired trajectory.

The rest of the paper is organized as follows: Section 2 introduces the mathematical modeling of robot model, the problem statement is in section 3. Section 4 shows the disturbance estimation methods, Section 5 shows the control approach and Section 6 discusses the results. The paper is concluded in Section 7.

2. Mathematical modeling of the 3-DoF Delta robot

The Delta robot considered here is a 3- DoF robot which consists of three closed-loop kinematic chains, each chain represents parallelogram to ensure the constant orientation between the fixed platform and the moving platform in the task space as in Figure 1. The delta robot is equipped with three identical actuators fixed on the fixed platform which has the Newtonian frame O . The radius of the fixed platform is f . The moving platform has radius r

with a frame E parallel to O . The parameters of the robot are listed in Table 1.

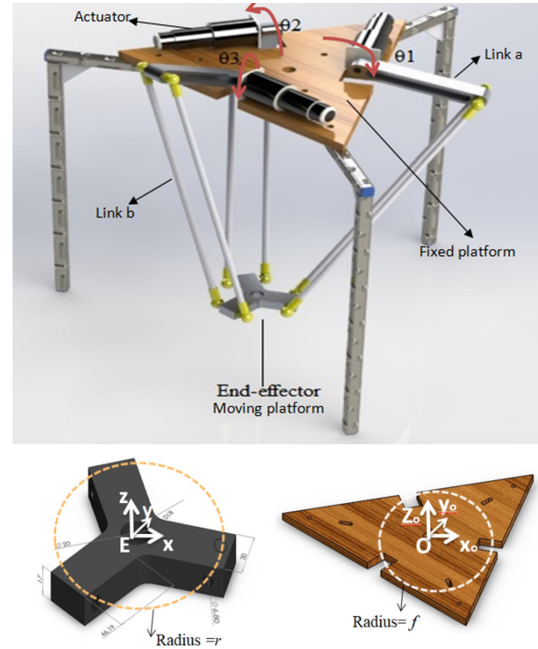


Figure 1. Delta robot

Table 1. Robot parameters

Description	Sym bol	Unit
Length of link a	L_a	m
Length of link b	L_b	m
Radius of the fixed platform	f	m
Radius of the moving platform	r	m
Mass of link a	m_a	Kg
Mass of link b	m_b	Kg
Mass of the moving platform	m_p	Kg
Gravity acceleration	g	9.8 m/s^2
Elbow mass	m_e	Kg
Actuator inertia	I_m	Kg.m ²
Gear ratio constant	k_G	-

The Delta robot dynamic model is described by a set of differential equations as

$$M(\theta)\ddot{\theta} + C(\theta, \dot{\theta})\dot{\theta} + G(\theta) + \tau_F = \tau, \quad (1)$$

where $\theta = [\theta_1 \ \theta_2 \ \theta_3]^T \in \mathbb{R}^3$ is the set of actuated joint vector. θ is measured using joint encoders attached to the joint actuators. $M \in \mathbb{R}^{3 \times 3}$ is the positive definite inertia matrix, $C(\theta, \dot{\theta})\dot{\theta} \in \mathbb{R}^3$ vector represents the Coriolis and centrifugal torques, $G(\theta) \in \mathbb{R}^3$ contains the gravitational terms acting on the robot. $\tau_F \in \mathbb{R}^3$ is the joint frictional vector and $\tau \in \mathbb{R}^3$ is the generalized joint control vector. Also, the above terms include the moving

plate position $\mathbf{p} \equiv [p_x \ p_y \ p_z]^T$ in \mathbb{R}^3 , the position vector starts from the origin of the frame O to the origin of the frame E . Then, the matrices M, C and G are given as follow [42]

$$M = (m_p + m_b) J^T J + \left(k_G^2 \mathbf{I}_m + L_a^2 \left(\frac{m_a}{3} + m_e + \frac{2}{3} m_b \right) \right) I_3$$

$$, C = J^T (m_p + m_b) \dot{J},$$

where I_q is the identity matrix of size q , J and \dot{J} are the Jacobian and its time derivative respectively.

$$G(\theta) = \begin{bmatrix} -J^T (m_p + m_b) \begin{bmatrix} 0 \\ 0 \\ -g \end{bmatrix} - \gamma mg \begin{bmatrix} \cos \theta_1 \\ \cos \theta_2 \\ \cos \theta_3 \end{bmatrix} \\ 0 \\ 0 \end{bmatrix},$$

where $m = m_a + m_e + \frac{2}{3} m_b$ and $\gamma = \frac{\frac{1}{3} m_a + m_e + \frac{2}{3} m_b}{m} L_a$

Link a_1 in chain one is rotated an angle of zero around the z_o axis in frame O , link a_2 in chain two is rotated an angle of 120° and link a_3 in chain three is rotated an angle of 240° . The Jacobian J is found by finding a closed loop position vector for each of the three chains and mapping the joint space variables to the Cartesian space variables. Since the length of link b is constant, this leads to three constraint equations.

3. Problem statement

In the ideal case where there is no external disturbance, the joint friction and the dynamic model are known, feedback linearization with PD controller will achieve the desired transient and steady state response for a manipulator by using simple linear pole placement techniques [39]. Unfortunately, in real systems disturbances and unmodeled dynamics exist. Further, the system parameters are not often precisely known. This paper considers the disturbance source from the uncertainty in the dynamic model inertia matrix $M(\theta)$, $C(\theta, \dot{\theta})$, $G(\theta)$ and τ_F . That means, it is assumed that

the inertia matrix $M(\theta)$ consists of two matrices; the constant diagonal matrix that represents the inertia of the robot upper links with the motor inertia \mathbf{I} and the uncertainty in the inertia matrix $\tilde{M}(\theta)$, i.e.

$M(\theta) = \mathbf{I} + \tilde{M}(\theta)$. In addition, call the terms with uncertainty part as lumped nonlinear disturbance ζ , then Eq (1) can be rewritten as

$$\mathbf{I} \ddot{\theta} + \zeta = \tau, \quad (2)$$

where ζ is given by

$$\zeta = C(\theta, \dot{\theta}) \dot{\theta} + G(\theta) + \tau_F + \tilde{M}(\theta) \ddot{\theta}, \quad (3)$$

and must be estimated and used in the control law for disturbance compensation.

Equation (2) can be written in state space form by choosing the actuated motors angular displacements and velocities as states:

$$\mathbf{x} \equiv [x_1 \ \cdots \ x_6]^T = [\theta_1 \ \theta_2 \ \theta_3 \ \dot{\theta}_1 \ \dot{\theta}_2 \ \dot{\theta}_3]^T$$

$$\dot{\mathbf{x}} = \underbrace{\begin{bmatrix} \mathbf{0}_{3 \times 3} & I_3 \\ \mathbf{0}_{3 \times 3} & \mathbf{0}_{3 \times 3} \end{bmatrix}}_A \mathbf{x} + \underbrace{\begin{bmatrix} \mathbf{0}_{3 \times 3} \\ \mathbf{I}^{-1} \end{bmatrix}}_B \mathbf{u} + \underbrace{\begin{bmatrix} \mathbf{0}_{3 \times 3} \\ -\mathbf{I}^{-1} \end{bmatrix}}_{F_d} \zeta, \quad (4)$$

where \mathbf{x} is the state vector, $\mathbf{0}_{q \times \beta}$ is zero matrix of size $q \times \beta$ and $\mathbf{u} = \tau$. The measurement vector can be represented as

$$y = \underbrace{\begin{bmatrix} I_3 & \mathbf{0}_{3 \times 3} \end{bmatrix}}_H \mathbf{x} \quad (5)$$

4. Disturbance estimation

It is possible to estimate the lumped disturbance vector using several methods: AKF, LFD and AMB methods. The estimation depends on the knowledge of the applied control torque at the joint. The model in Eq (2) is rewritten in other representations suitable for each estimation method.

AKF method

The AKF is an adaptive observer for linear systems, it is used to estimate the disturbance by augmenting the disturbance with the states as an extended state, accordingly, Eq (4) is rewritten in the form

$$\begin{bmatrix} \dot{\mathbf{x}} \\ \dot{\zeta} \end{bmatrix} = \begin{bmatrix} A & F_d \\ \mathbf{0}_{3 \times 6} & \mathbf{0}_{3 \times 3} \end{bmatrix} \begin{bmatrix} \mathbf{x} \\ \zeta \end{bmatrix} + \begin{bmatrix} B \\ \mathbf{0}_{3 \times 3} \end{bmatrix} \mathbf{u}, \quad (6)$$

The measurement vector consists of the active joint angles that are measured using joint encoders attached to the joint actuators. In addition to that, differentiating the angular position numerically using backward Euler formula gives valuable information. Hence $\dot{\theta}$ is considered as pseudo measured. Discretizing Eq (6) using backward Euler formula yields

$$\begin{bmatrix} \mathbf{x}(k) \\ \zeta(k) \end{bmatrix} = A_d \begin{bmatrix} \mathbf{x}(k-1) \\ \zeta(k-1) \end{bmatrix} + B_d u(k) + v(k-1), \quad (7)$$

$$z = H_{new} \begin{bmatrix} \mathbf{x}(k) \\ \zeta(k) \end{bmatrix} + v(k)$$

where

$$A_d = \begin{bmatrix} I_3 & T I_3 & \mathbf{0}_{3 \times 3} \\ \mathbf{0}_{3 \times 3} & I_3 & -T \mathbf{I}^{-1} I_3 \\ \mathbf{0}_{3 \times 3} & \mathbf{0}_{3 \times 3} & I_3 \end{bmatrix}, B_d = \begin{bmatrix} \mathbf{0}_{3 \times 3} \\ T \mathbf{I}^{-1} \\ \mathbf{0}_{3 \times 3} \end{bmatrix}, \quad (8)$$

$H_{new} = [I_6 \ \mathbf{0}_{6 \times 3}]$ is the output matrix, T is the sampling time and k is the time index. $v \in \mathbb{R}^9$ and $v \in \mathbb{R}^6$ are the zero mean Gaussian process and measurement noises with covariance matrices Q and R respectively, i.e. $v \sim N(0, Q)$ and $v \sim N(0, R)$. The covariance matrices Q and R are unknown and have an important effect on Kalman filter estimates. If the given value of Q is much smaller than the true value, then the result is biased estimated states $\hat{\mathbf{x}}$ and $\hat{\zeta}$. On the other hand, if the given value of Q is much larger than the true value, then the estimated states $\hat{\mathbf{x}}$ and $\hat{\zeta}$ will oscillate around the true value. The advantage of the AKF [40] is that it does not need the values of the noise covariance

matrices, just initial values of them are required. Then by its recursive structure, it updates the covariance matrices based on the innovation e between the predicted states and the measured vector. This error is used to update and correct the predicted states through Kalman gain which takes into the consideration the uncertainty in the model through the covariance matrices. The output of this filter are the estimated states $\hat{\mathbf{x}}$ and $\hat{\zeta}$. The following assumptions are considered:

- **Assumption 1:** The process and measurement noises are assumed to be independent and mutually uncorrelated.
- **Assumption 2:** The inputs are considered to be piecewise constant over the sampling time interval T .

The AKF requires positive constants N_R and N_Q , initial values of matrices R_0 and Q_0 , and an initial value of the estimation error covariance matrix P_0 . The AKF algorithm is shown between Eqs (9) and (23) respectively.

Initial values $\bar{\omega}_0, \bar{e}_0, \hat{x}_0, P_0, N_R, N_Q, Q_0 > 0, R_0 > 0$

$$\begin{bmatrix} \hat{\mathbf{x}}^-(k) \\ \hat{\zeta}^-(k) \end{bmatrix} = A_d \begin{bmatrix} \hat{\mathbf{x}}^-(k-1) \\ \hat{\zeta}^-(k-1) \end{bmatrix} + B_d u(k), \quad (9)$$

$$P^-(k) = A_d P(k-1) A_d^T + Q(k-1), \quad (10)$$

$$e(k) = z(k) - H_{new} \begin{bmatrix} \hat{\mathbf{x}}^-(k) \\ \hat{\zeta}^-(k) \end{bmatrix}, \quad (11)$$

$$\alpha_1 = \frac{N_R - 1}{N_R}, \alpha_2 = \frac{N_Q - 1}{N_Q}, \quad (12)$$

$$\bar{e}(k) = \alpha_1 \bar{e}(k-1) + \frac{1}{N_R} e(k), \quad (13)$$

$$\Delta R(k) = \frac{1}{N_R - 1} (e(k) - \bar{e}(k)) (e(k) - \bar{e}(k))^T - \frac{1}{N_R} (H_{new} P^- H_{new}^T)_{(k)} \quad (14)$$

$$R(k) = \alpha_1 R(k-1) + \Delta R(k), \quad (15)$$

$$K(k) = P^-(k) H_{new}^T (H_{new} P^-(k) H_{new}^T + R(k))^{-1}, \quad (16)$$

$$\begin{bmatrix} \hat{\mathbf{x}}(k) \\ \hat{\zeta}(k) \end{bmatrix} = \begin{bmatrix} \hat{\mathbf{x}}^-(k) \\ \hat{\zeta}^-(k) \end{bmatrix} + K(k) e(k), \quad (17)$$

$$P(k) = (I - K(k) H_{new}) P^-(k), \quad (18)$$

$$\hat{\omega}(k) = \begin{bmatrix} \hat{\mathbf{x}}(k) \\ \hat{\zeta}(k) \end{bmatrix} - \begin{bmatrix} \hat{\mathbf{x}}^-(k) \\ \hat{\zeta}^-(k) \end{bmatrix}, \quad (19)$$

$$\bar{\omega}(k) = \alpha_2 \bar{\omega}(k-1) + \frac{1}{N_Q} \hat{\omega}(k), \quad (20)$$

$$\Delta Q(k) = \frac{1}{N_Q} (P(k) - A_d P(k) A_d^T) + \frac{1}{N_Q - 1} (\hat{\omega}(k) - \bar{\omega}(k)) (\hat{\omega}(k) - \bar{\omega}(k))^T, \quad (21)$$

$$Q(k) = \alpha_2 Q(k-1) + \Delta Q(k), \quad (22)$$

$$Q(k-1) = \text{diag}(Q(k)), \quad (23)$$

$$R(k-1) = \text{diag}(R(k))$$

where $(\cdot)^-$ and (\cdot) stand for the prior and posterior estimates, respectively. K is the Kalman gain. $z \in \mathbb{R}^6$ is the measurement vector and $\hat{\omega}$ is the state error.

Implementation note: for a noisy system, it is much better to give more weight to the previous known values $(R(k-1), Q(k-1))$ than the current noisy reading, and this is achieved by selecting big N_R and/or N_Q . In the same context, small N_R and/or N_Q give more weight to the current reading $(\Delta R_k, \Delta Q_k)$ for less noisy readings.

Low pass filtered dynamic model method LFDMM

The robot model in Eq (2) can be rewritten as

$$\zeta = \tau - \mathbf{I}\ddot{\theta}, \quad (24)$$

The right hand-side of Eq (24) can be computed if the angular acceleration $\ddot{\theta}$ is known. However, in most cases this acceleration is unmeasured. The filtered dynamic model [26, 43, 44] avoids the explicit calculation of this acceleration by filtering both sides of Eq (24) using a proper stable filter. For this 3-DoF robot, three first order filters with three constants σ_i for $i=1,2,3$ are used. The transfer function of each filter $\mathbb{Z}_i(s)$ and the corresponding impulse response $z_i(t)$ are written as

$$\mathbb{Z}_i(s) = \sigma_i \frac{1}{s + \sigma_i}, \quad (25)$$

and

$$z_i(t) = \ell^{-1}(\mathbb{Z}_i(s)) = \sigma_i e^{-\sigma_i t}, \quad (26)$$

respectively, where $\ell^{-1}(\cdot)$ is the Laplace inverse transform and s refers to Laplace transform. Then the impulse response for the 3-DoF robot is

$$\mathbf{z}(t) = \begin{bmatrix} \sigma_1 e^{-\sigma_1 t} & 0 & 0 \\ 0 & \sigma_2 e^{-\sigma_2 t} & 0 \\ 0 & 0 & \sigma_3 e^{-\sigma_3 t} \end{bmatrix}. \quad (27)$$

Since the multiplication in the frequency domain is equivalent to the convolution in time domain, then the filtered version of Eq (24) is

$$\int_0^t \mathbf{z}(t-\tau) \zeta d\tau = \int_0^t \mathbf{z}(t-\tau) \tau d\tau - \int_0^t \mathbf{z}(t-\tau) \mathbf{I}\ddot{\theta} d\tau \quad (28)$$

Remembering that \mathbf{I} is constant matrix, then $\dot{\mathbf{I}} = 0$. Further at time $t = 0$, the initial condition $\dot{\theta}(0) = 0$ and the impulse response is the diagonal matrix

$\mathbf{z}(0) = \boldsymbol{\sigma} = \text{diag}(\sigma_1, \sigma_2, \sigma_3)$. Having that, the term $\int_0^t \mathbf{z}(t-\tau) \mathbf{I} \ddot{\boldsymbol{\theta}} d\tau$ will be

$$\int_0^t \mathbf{z}(t-\tau) \mathbf{I} \ddot{\boldsymbol{\theta}} d\tau = \boldsymbol{\sigma} \mathbf{I} \dot{\boldsymbol{\theta}} - \int_0^t \dot{\mathbf{z}}(t-\tau) \mathbf{I} \dot{\boldsymbol{\theta}} d\tau \quad (29)$$

where $\dot{\mathbf{z}}$ is the derivative of the filter response

$$\dot{\mathbf{z}}(t) = -\text{diag}(\sigma_1^2 e^{-\sigma_1 t}, \sigma_2^2 e^{-\sigma_2 t}, \sigma_3^2 e^{-\sigma_3 t}), \quad (30)$$

or in Laplace domain

$$\ell\{\dot{z}_i(t)\} = \ell\{-\sigma_i^2 e^{-\sigma_i t}\} = -\sigma_i^2 \frac{1}{s + \sigma_i}.$$

Using the above equations, the filtered model is

$$\int_0^t \mathbf{z}(t-\tau) \zeta d\tau = -\boldsymbol{\sigma} \mathbf{I} \dot{\boldsymbol{\theta}} + \int_0^t \mathbf{z}(t-\tau) (\boldsymbol{\tau}) d\tau + \int_0^t \dot{\mathbf{z}}(t-\tau) \mathbf{I} \dot{\boldsymbol{\theta}} d\tau \quad (31)$$

The left hand side of Eq (31) is the resulted filtered version of the disturbance using the filter in Eq (25). The right hand side is filtered using either Eq (25) or Eq (30). The cut-off frequency of the first order filter depends on the highest basic frequency in the measurements. It is user defined.

Acceleration measurement-based estimation method AMB

This method considers the existence of a three axes-accelerometer at the moving platform. Thus, the acceleration vector $\mathbf{a} \equiv \ddot{\mathbf{p}} = \dot{\mathbf{v}}$ is considered being measured and can be expressed as

$$\mathbf{a} = \mathbf{J} \ddot{\boldsymbol{\theta}} + \dot{\mathbf{J}} \dot{\boldsymbol{\theta}}. \quad (32)$$

Then the robot model in Eq (2) along with Eq (32) lead to estimate the disturbance as

$$\boldsymbol{\zeta} = \boldsymbol{\tau} - \mathbf{J}^{-1} (\mathbf{a} - \dot{\mathbf{J}} \dot{\boldsymbol{\theta}}). \quad (33)$$

This method depends directly on the measured angular velocity.

5. Control approach

The controller has two parts. The first part of the presented control architecture is a stabilizing and robust tracking mechanism using a PD controller that is designed to track the reference trajectory. The second part is the adaptive disturbance compensation.

PD controller

In the ideal case, consider that the estimated lumped disturbance vector $\hat{\boldsymbol{\zeta}}$ converged to the true value of $\boldsymbol{\zeta}$, i.e. $\boldsymbol{\zeta} - \hat{\boldsymbol{\zeta}} \rightarrow 0$. Then for the model Eq (2), after some mathematical manipulation, the error dynamics is given as

$$\ddot{\mathbf{e}} + k_d \dot{\mathbf{e}} + k_p \mathbf{e} = 0 \quad (34)$$

Where $\mathbf{e} = \boldsymbol{\theta} - \boldsymbol{\theta}_d$, $\boldsymbol{\theta}_d$ is the desired trajectory, k_p and k_d are the positive gains of the PD controller which can be determined using pole placement techniques.

Adaptive disturbance compensation

The estimated disturbance is used to achieve the feedback linearization adaptively so that linear controllers are applied. The estimated disturbance is added directly to the PD controller output. However, in the transient

response, the estimated disturbance $\hat{\boldsymbol{\zeta}}$ suffers from the overshoot which affects the robot response adversely. Therefore, a tuning gain $\boldsymbol{\lambda} = \text{diag}(\lambda_1, \lambda_2, \lambda_3)$ is introduced to scale $\hat{\boldsymbol{\zeta}}$ adaptively. The gain range is $\lambda \in (0, 1]$.

Define the maximum value of the error \mathbf{e} as $\mathbf{e}_m \equiv [\mathbf{e}_{m_1} \ \mathbf{e}_{m_2} \ \mathbf{e}_{m_3}]^T$ and the positive constant $k_t \equiv [k_{t_1} \ k_{t_2} \ k_{t_3}]^T$. Both \mathbf{e}_m and k_t are user defined. For simplicity, only the scalar case is considered. It is desired that the gain λ scales $\hat{\boldsymbol{\zeta}}$ in the transient response when it has the overshoot. While at the steady state, the value of λ is one or close to one. The design of λ is based on \mathbf{e} , when the error \mathbf{e} is big, then majority of the effort is given to the PD controller; this is accomplished by decreasing the gain λ . On the other hand, when the error \mathbf{e} decreases, λ increases to its maximum value of unity. As shown in Figure 2, when the error $\mathbf{e} \rightarrow \mathbf{e}_m$ specially at the initial run of the estimator, λ value will be k_t i.e. $\lambda = k_t$. Once the error converges, λ value will be close to one, i.e. $\lambda \approx 1$, hence the same estimated disturbance $\hat{\boldsymbol{\zeta}}$ is added to the PD controller output. The mathematical representation of the tuning gain for the three joints is given by

$$\boldsymbol{\lambda} = \begin{bmatrix} \frac{1 - k_{t_1} |\mathbf{e}_1| + 1}{\mathbf{e}_{m_1}} & 0 & 0 \\ 0 & \frac{1 - k_{t_2} |\mathbf{e}_2| + 1}{\mathbf{e}_{m_2}} & 0 \\ 0 & 0 & \frac{1 - k_{t_3} |\mathbf{e}_3| + 1}{\mathbf{e}_{m_3}} \end{bmatrix} \quad (35)$$

and the corresponding tuned disturbance is $\boldsymbol{\lambda} \hat{\boldsymbol{\zeta}}$. The overall control approach is shown in Figure 3.

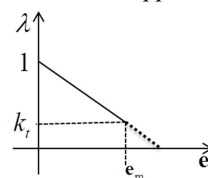


Figure 2. Disturbance tuning gain

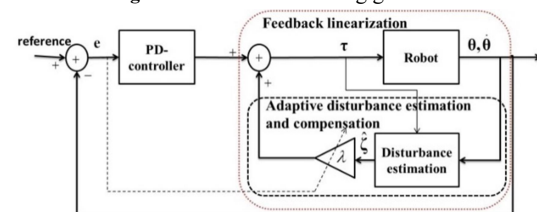


Figure 3. Adaptive feedback linearization and control of delta robot

6. Experimental Simulation Results

To evaluate the estimation and tracking performance, the true joint friction is required. However, since it is difficult to measure the friction, MATLAB environment is

used as an experimental platform to carry out simulations on the robot model. The experiments are carried on 3-DoF delta robot model as shown in Figure 1. The values of the delta robot parameters are given in Table 2, for more details on the robot model refer to [45]. To be more realistic, Gaussian noise was added to both the measured acceleration and the pseudo measured angular velocity. This noise was generated using MATLAB Simulink Gaussian noise generator with zero mean and variance 0.001. The sampling time of this simulation $T=0.001s$. The original nonlinear model of the robot is used throughout the simulation.

The true joint friction is generated using the nonlinear model [23].

$$\tau_F = \gamma_1 (\tanh(\gamma_2 \dot{\theta}) - \tanh(\gamma_3 \dot{\theta})) + \gamma_4 \tanh(\gamma_5 \dot{\theta}) + \gamma_6 \dot{\theta} \quad (36)$$

where $\gamma_i, i=1, \dots, 6$ are positive constants and the static coefficient of friction can be approximated by $\gamma_1 + \gamma_4$. The stribek effect is represented by $(\tanh(\gamma_2 \dot{\theta}) - \tanh(\gamma_3 \dot{\theta}))$, $\gamma_4 \tanh(\gamma_5 \dot{\theta})$ and $\gamma_6 \dot{\theta}$ represent the coulomb friction and the viscous dissipation respectively. Each of the active joints has the same adopted friction model. The values of the parameters $\gamma_i, i=1, \dots, 6$ are listed in Table 3

Table 2. The values of the Delta robot parameters

Parameter	Value
f	0.1 m
r	0.055 m
L_a	0.18 m
L_b	0.435 m
Mass of moving platform	0.196 kg
Mass of elbow	0.024 kg
Mass of link b	0.055 kg
Mass of link a	0.190 kg
Motor inertia	81.6×10^{-3} ;
Motor gear ratio constant	0.01

Before the estimation takes place, a traditional PD controller is used with the transfer function

$$PD(s) = k_p + k_d N \frac{s}{s + N}, \quad (37)$$

here $k_p = 25I_3$, $k_d = I_3$ and $N=100$, these values were selected to obtain the best possible trajectory tracking response without disturbance compensation as depicted in

Figure 4 which shows the error between the desired and the actual trajectories.

Table 3. Friction model parameters for each joint

Friction model constants	Joint 1	Joint 2	Joint 3
γ_1	0.7	0.6	5
γ_2	10	10	10
γ_3	10	10	10
γ_4	0.6	0.5	0.4
γ_5	50	100	10
γ_6	0.9	0.9	0.9

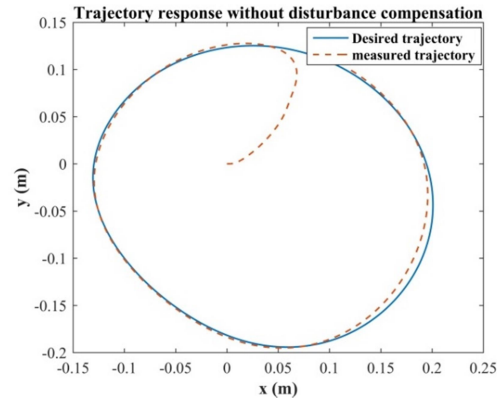


Figure 4. Trajectory response without disturbance compensation.

6.1. Disturbance Estimation Performance

The estimation is carried out simultaneously for all the active joints using the three methods. The AKF is recursive-based estimation and requires initializations which are listed in Table 4. The error initial values were set to zero. The state covariance errors were set to 100 since the error between the estimated value and the true value is large at the beginning. The values of N_R and N_Q are set to be equal which is not necessary for all systems, they can have different values. The LFDm requires the filter constant σ which is selected to be 5 for all joints. Low values of the filter cut off frequency will deteriorate the dynamics of the estimated disturbance.

In order to evaluate the estimation performance, the estimated results at this section were obtained without disturbance compensation. For the simulation purposes, the acceleration of the moving platform is computed using Eq (32).

Table 4. AKF parameters and initializations

Parameter	Value	Parameter	Value
$R(0)$	$0.1I_6$	$\bar{e}(0)$	$\mathbf{0}_{6 \times 1}$
$Q(0)$	$0.001I_9$		10^6
$P(0)$	$100I_9$	N_Q	10^6
$\hat{x}(0)$	$\mathbf{0}_{6 \times 1}$	$\mathbf{u}(0)$	$\mathbf{0}_{3 \times 1}$
$\hat{\zeta}(0)$	$\mathbf{0}_{3 \times 1}$	$\bar{\omega}(0)$	$\mathbf{0}_{9 \times 1}$

The estimated disturbance vector $\hat{\zeta}$ at the three active joints using the three methods is depicted in Figure 5. The estimated disturbance using the AMB method has very high overshoot, and it converges to the true value faster than the LFDm. On the other hand, the AKF tracks the true value and has the best response among the three methods in terms of overshoot, convergence speed and tracking. Further, the AKF considers the noise either in the

process or in the measurement through the matrices Q and R and reflects them on the filter gain. At the same time, it tunes the filter gain adaptively according to the estimation performance.

The AMB method suffers from very high overshoot. Further, it is very sensitive to the noise which may limit its use. As a performance measure, the mean square error (MSE) is used. The MSE is given by

$$MSE(j) = \frac{1}{n} \sum_{i=1}^n (\zeta(j) - \hat{\zeta}(j))^2, \quad (38)$$

where n is the number of measurements and $j=1,2,3$ is the active joint index. Table 5 shows the MSE of $\hat{\zeta}$ for the three joints. Accordingly, the AKF has the best MSE,

the AMB performance depends on the quality of the measurement.

In terms of implementation and requirements, the AMB does not require any constants or initializations, the LFDM requires the filter constant. On the other hand, the AKF requires several initializations which are easy to be initialized and then will be tuned adaptively according to the filter performance. In terms of noise considerations, only the AKF considers the noise through the process and measurement noise covariance matrices.

In terms of computational cost, the AKF has more cost than the other methods due to the algorithm structure. The LFDM has the lowest computational cost.

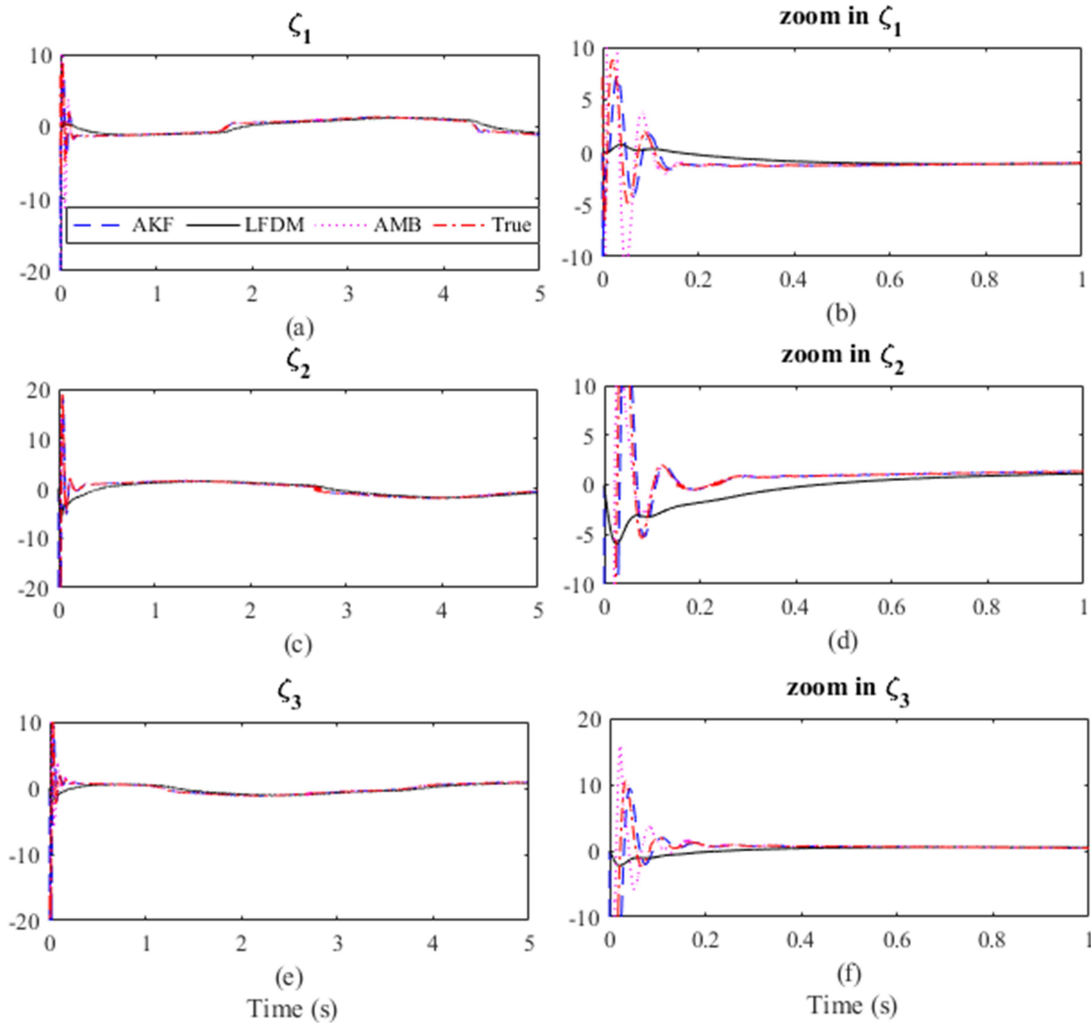


Figure 5. Estimated disturbance a) $\hat{\zeta}_1$, b) zoomed version of $\hat{\zeta}_1$, c) $\hat{\zeta}_2$, d) zoomed version of $\hat{\zeta}_2$, e) $\hat{\zeta}_3$ and f) zoomed version of $\hat{\zeta}_3$ using the three methods

Table 5. MSE of the estimated disturbance using the three methods

Joint	AKF	LFDM	AMB
Joint 1	0.0003	0.0004	0.0028
Joint 2	0.0028	0.0042	0.0042
Joint 3	0.0011	0.0034	0.0027

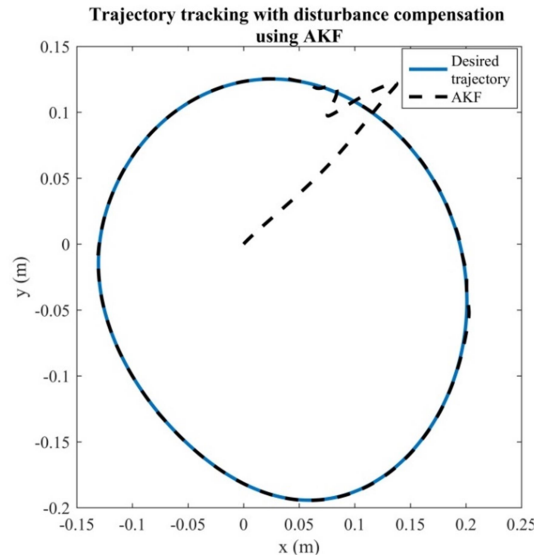
6.2. Disturbance compensation performance and discussion

The estimated disturbance $\hat{\zeta}$ is added directly to the control signal from the PD controller to form online disturbance estimation and compensation. Although the previous section shows the quality of the estimated disturbance, however, the transient estimation response affects the control law diversely. Therefore a tuning gain λ is added as in Figure 3. The response of disturbance compensation based on the AKF is depicted in Figure 6. The moving plate starts from its home position to track the desired trajectory with an overshoot. This response is expected according to the estimated disturbance discussed before. Also, it is expected that this method is much better than the other methods.

The gain λ values are plotted in Figure 7. $e_m = [1 \ 1 \ 1]^T$ and $k_r = [0.3 \ 0.3 \ 0.3]^T$ are considered. As clear the gain for $\hat{\zeta}_1$ starts with value of 0.87 in the period of the transient response of the estimated disturbance. This indicates that 87% of the estimated disturbance $\hat{\zeta}_1$ is passed to the control law. For $\hat{\zeta}_2$, it has more overshoot than $\hat{\zeta}_1$ using the same estimator AKF, this explains the reason of the value of the gain to be 0.38. Then the gain converges to be close to one i.e. the same estimated disturbance is used with the control law.

The LFDM method has steady state error under the same running conditions as shown in Figure 8. The tuned gain depicted in Figure 9 starts from a value of 0.35. This confirms the observation in Figure 5. As shown in Figure 5, the LFDM deteriorates the dynamics of the signal, this is confirmed in Figure 9 as the gain converges to one with less oscillations compared with AKF.

Lastly, the AMB method is not recommended according to Figure 10 and Figure 11.

**Figure 6.** Trajectory tracking with disturbance compensation using AKF

7. Conclusion

The main contribution of this paper is to implement an adaptive estimation-control approach to satisfy a predefined performance with tuning few parameters. The Disturbance deteriorates the tracking performance of the delta robot. This paper studied three methods of disturbance estimation by considering the lumped disturbance vector. The AKF method is the most accurate and has a fast convergence. This method is adaptive by the nature of the AKF and supports the adaptive trajectory tracking. The required initializations are randomly selected, and the filter updates the results adaptively. This AKF method is applicable to robots in general and not only to delta robot. The other methods cause tracking errors and are not recommended. Further, to overcome the initial estimation dynamics challenge on the control system and to enhance the control flexibility, an adaptive controller is used with the disturbance to form the adaptive disturbance compensation. As a result, the PD controller can perform well to get the desired performance. The proposed controller gives better results in terms of steady-state error.

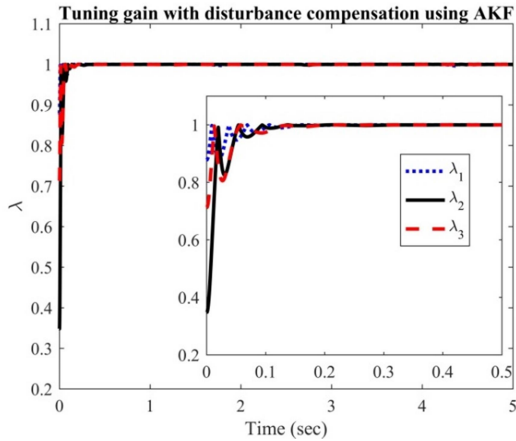


Figure 7. The tuning gain with disturbance compensation using AKF

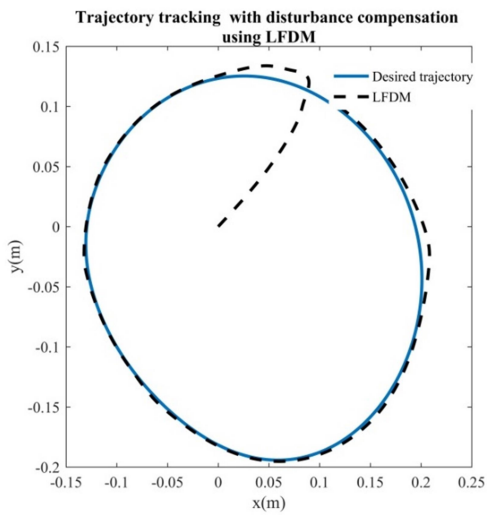


Figure 8. Trajectory tracking with disturbance compensation using LFD

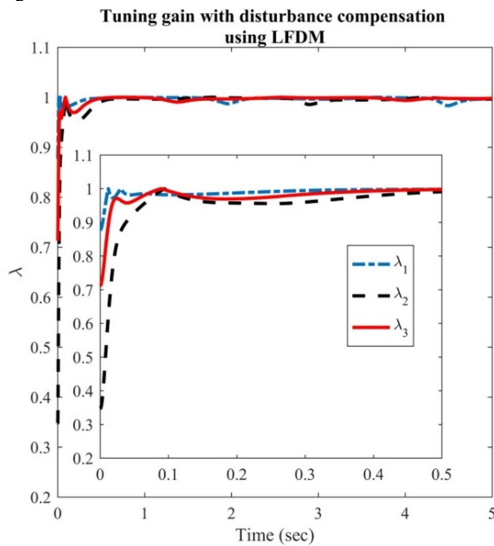


Figure 9. The tuning gain with disturbance compensation using LFD

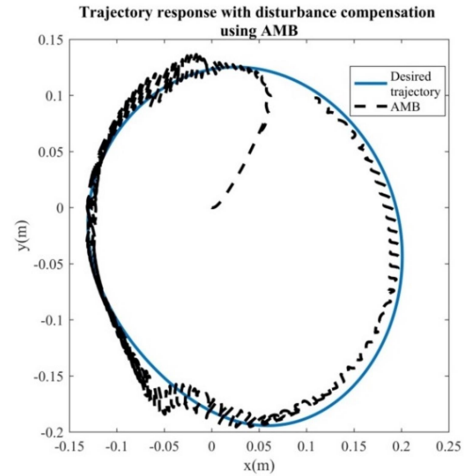


Figure 10. Trajectory response with disturbance compensation using AMB

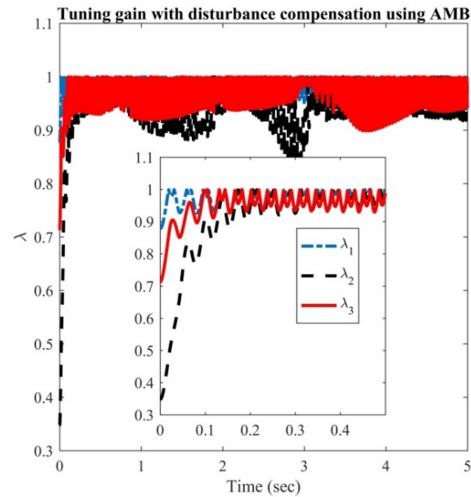


Figure 11. The tuning gain with disturbance compensation using AMB

References

- [1] V. Nabat, M. de la O Rodriguez, O. Company, S. Krut, and F. Pierrot. "Par4: very high speed parallel robot for pick-and-place". IEEE/RSJ International Conference on intelligent robots and systems, 2005.
- [2] T. Huang, J. Mei, Z. Li, X. Zhao, and D. G. Chetwynd, "A method for estimating servomotor parameters of a parallel robot for rapid pick-and-place operations". Journal of Mechanical Design, Vol. 127, No. 4, 2005, pp. 596-601.
- [3] S. Wang, H. Lin, R. Gai, and Y. Sun. "An application of vision technology on intelligent sorting system by delta robot". IEEE 19th International Conference on e-Health Networking, Applications and Services (Healthcom), 2017.
- [4] J. Pattavanitch and S. Panyaru, "Development of a new linear delta robot for the fused deposition modelling process". Journal of Research and Applications in Mechanical Engineering, Vol. 5, No. 1, 2017, pp. 42-54.
- [5] Z. H. Khan, A. Khalid, and J. Iqbal, "Towards realizing robotic potential in future intelligent food manufacturing systems". Innovative food science & emerging technologies, Vol. 48, No. 2018, pp. 11-24.

- [6] X. Zhang, R. Zhang, L. Chen, and X. Zhang, "Natural Gesture Control of a Delta Robot Using Leap Motion". *Journal of Physics: Conference Series*, 2019.
- [7] D. Grajewski, F. Gorski, D. Rybarczyk, P. Owczarek, A. Milecki, and P. Bun, "Use of Delta Robot as an Active Touch Device in Immersive Case Scenarios". *Procedia Computer Science*, Vol. 104, No. 2017, pp. 485-492.
- [8] I. Bonev, "Delta parallel robot—the story of success," in *Newsletter*, available at <http://www.parallelmic.org>, ed, 2001.
- [9] M. Ramírez-Neria, H. Sira-Ramírez, A. Luviano-Juárez, and A. Rodríguez-Ángeles, "Active disturbance rejection control applied to a delta parallel robot in trajectory tracking tasks". *Asian Journal of Control*, Vol. 17, No. 2, 2015, pp. 636-647.
- [10] A. Zidan, D. Kaczor, S. Tappe, and T. Ortmaier, "Optimization of a P/PI Cascade Motion Controller for a 3-DOF Delta Robot," in *Tagungsband des 4. Kongresses Montage Handhabung Industrieroboter*, ed: Springer, 2019, pp. 217-226.
- [11] L. Angel, J. Sebastian, R. Saltaren, and R. Aracil. "RoboTennis system part II: Dynamics and control". *Proceedings of the 44th IEEE Conference on Decision and Control*, 2005.
- [12] J. Fabian, C. Monterrey, and R. Canahuire. "Trajectory tracking control of a 3 DOF delta robot: a PD and LQR comparison". *IEEE International Congress on Electronics, Electrical Engineering and Computing*, 2016.
- [13] A. Dumlu and K. Erenturk, "Trajectory tracking control for a 3-dof parallel manipulator using fractional-order $PI^{\lambda}D^{\mu}$ control". *IEEE Transactions on Industrial Electronics*, Vol. 61, No. 7, 2013, pp. 3417-3426.
- [14] Y.-L. Kuo and P.-Y. Huang, "Experimental and simulation studies of motion control of a Delta robot using a model-based approach". *International Journal of Advanced Robotic Systems*, Vol. 14, No. 6, 2017, pp. 1-14.
- [15] K. P. Jankowski and H. Van Brussel, "An approach to discrete inverse dynamics control of flexible-joint robots". *IEEE Transactions on Robotics and Automation*, Vol. 8, No. 5, 1992, pp. 651-658.
- [16] Y. Su, D. Sun, L. Ren, and J. K. Mills, "Integration of saturated PI synchronous control and PD feedback for control of parallel manipulators". *IEEE Transactions on Robotics*, Vol. 22, No. 1, 2006, pp. 202-207.
- [17] H.-H. Lin, Y.-H. Ta, and C.-S. Liu. "The implementation of smoothing robust control for a delta robot". *Second International Conference on Robot, Vision and Signal Processing*, 2013.
- [18] R. H. Hensen, M. Van de Molengraft, and M. Steinbuch, "Friction induced hunting limit cycles: A comparison between the LuGre and switch friction model". *Automatica*, Vol. 39, No. 12, 2003, pp. 2131-2137.
- [19] H. Olsson and K. J. Astrom, "Friction generated limit cycles". *IEEE Transactions on Control Systems Technology*, Vol. 9, No. 4, 2001, pp. 629-636.
- [20] B. Armstrong-Hélouvry, P. Dupont, and C. C. De Wit, "A survey of models, analysis tools and compensation methods for the control of machines with friction". *Automatica*, Vol. 30, No. 7, 1994, pp. 1083-1138.
- [21] R. H. A. Helsen, G. Z. Angelis, M. J. G. van de Molengraft, A. G. de Jager, and J. J. Kok, "Grey-box Modeling of Friction: An Experimental Case-study". *European Journal of Control*, Vol. 6, No. 3, 2000, pp. 258-267.
- [22] V. Lampaert, J. Swevers, and F. Al-Bender, "Modification of the Leuven integrated friction model structure". *IEEE Transactions on Automatic Control*, Vol. 47, No. 4, 2002, pp. 683-687.
- [23] C. Makkar, W. E. Dixon, W. G. Sawyer, and G. Hu. "A new continuously differentiable friction model for control systems design". *IEEE/ASME International Conference on Advanced Intelligent Mechatronics*, Monterey, CA, 2005.
- [24] G. Morel, K. Iagnemma, and S. Dubowsky, "The precise control of manipulators with high joint-friction using base force/torque sensing". *Automatica*, Vol. 36, No. 7, 2000, pp. 931-941.
- [25] B. Bona and M. Indri. "Friction Compensation in Robotics: an Overview". *IEEE European Control Conference on Decision and Control*, Seville, Spain, 2005.
- [26] I. Hashlamon and K. Erbatur, "Reduced Filtered Dynamic Model for Joint Friction Estimation of Walking Bipeds". *Jordan Journal of Mechanical & Industrial Engineering*, Vol. 11, No. 3, 2017,
- [27] I. Hashlamon and K. Erbatur, "Joint friction estimation for walking bipeds". *Robotica*, Vol. 34, No. 7, 2014, pp. 1610-1629.
- [28] I. F. Hashlamon, "Joint friction estimation and slip prediction of biped walking robots," PhD diss, Sabanci University, 2014.
- [29] A. Mohammadi, M. Tavakoli, H. J. Marquez, and F. Hashemzadeh, "Nonlinear disturbance observer design for robotic manipulators". *Control Engineering Practice*, Vol. 21, No. 3, 2013, pp. 253-267.
- [30] C. Wen-Hua, D. J. Ballance, P. J. Gawthrop, and J. O'Reilly, "A nonlinear disturbance observer for robotic manipulators". *IEEE Transactions on Industrial Electronics*, Vol. 47, No. 4, 2000, pp. 932-938.
- [31] A. Radke and Z. Gao. "A survey of state and disturbance observers for practitioners". *American Control Conference*, 2006.
- [32] H. Sussmann and P. Kokotovic, "The peaking phenomenon and the global stabilization of nonlinear systems". *IEEE Transactions on automatic control*, Vol. 36, No. 4, 1991, pp. 424-440.
- [33] A. A. Ball and H. K. Khalil. "High-gain observers in the presence of measurement noise: A nonlinear gain approach". *2008 47th IEEE Conference on Decision and Control*, 2008.
- [34] L. A. Castañeda, A. Luviano-Juárez, and I. Chairez, "Robust trajectory tracking of a delta robot through adaptive active disturbance rejection control". *IEEE Transactions on Control Systems Technology*, Vol. 23, No. 4, 2015, pp. 1387-1398.
- [35] H. Wang, "Adaptive Control of Robot Manipulators With Uncertain Kinematics and Dynamics". *IEEE Transactions on Automatic Control*, Vol. 62, No. 2, 2017, pp. 948-954.
- [36] B. Xiao and S. Yin, "Exponential tracking control of robotic manipulators with uncertain dynamics and kinematics". *IEEE Transactions on Industrial Informatics*, Vol. 15, No. 2, 2018, pp. 689-698.
- [37] C. E. Boudjedir, D. Boukhetala, and M. Bouri, "Nonlinear PD plus sliding mode control with application to a parallel delta robot". *Journal of Electrical Engineering*, Vol. 69, No. 5, 2018, pp. 329-336.
- [38] C. Lu, X. Miao, S. Wang, and C. Zhang. "Research on Adaptive Robust Control Algorithm for Delta Parallel Robots". *Transactions on Intelligent Welding Manufacturing*, Singapore, 2019.
- [39] R. Hayat, M. Leibold, and M. Buss, "Robust-Adaptive Controller Design for Robot Manipulators Using the H_{∞} Approach". *IEEE Access*, Vol. 6, No. 2018, pp. 51626-51639.
- [40] I. Hashlamon, "A New Adaptive Extended Kalman Filter for a Class of Nonlinear Systems". *Journal of Applied and Computational Mechanics*, Vol. 6, No. 1 2020, pp. 1-12.
- [41] I. Hashlamon and K. Erbatur, "An improved real-time adaptive Kalman filter with recursive noise covariance updating rules". *Turkish journal of electrical engineering & computer sciences*, Vol. 24, No. 2, 2016, pp. 524-540.
- [42] A. Olsson, "Modeling and control of a Delta-3 robot," Master Department of Automatic Control, Lund University, 2009.

- [43] P. Hsu, M. Bodson, S. Sastry, and B. Paden. "Adaptive identification and control for manipulators without using joint accelerations". Proceedings IEEE International Conference on Robotics and Automation, Raleigh, NC, USA, 1987.
- [44] M. Van Damme, P. Beyl, B. Vanderborght, V. Grosu, R. Van Ham, I. Vandemiepen, *et al.* "Estimating robot end-effector force from noisy actuator torque measurements". IEEE International Conference on Robotics and Automation (ICRA), Shanghai, 2011.
- [45] R. Lazzari, "Sensorless Haptic Force Feedback for Telemanipulation using two identical Delta Robots," Master, Automation Engineering, Padova university, 2017.

Design of a Screw Conveyor for Transporting and Cooling Plantain Flour in a Process Plant

Michael Kanisuru Adeyeri^{a*}, Sesan Peter Ayodeji^a, Emmanuel Olatunji Outomilola^a, Janet Omoyeni Bako^b

^aIndustrial and Production Engineering Department/Mechanical Engineering Department, School of Engineering and Engineering Technology, Federal University of Technology, P.M.B 704, Akure, Ondo State, Nigeria.

^bMechanical Engineering Department, School of Engineering, Kogi State Polytechnic, Lokoja, Nigeria.

Received April 20 2020

Accepted November 30 2020

Abstract

This paper discusses the design, simulation and functional performance evaluation of an inclined screw conveyor with integrated system for cooling while conveying pulverized pulps from pulverizing unit to packaging unit of a plant that processes unripe plantain into flour. Hygiene, ergonomics, conveyance distance and height, thermal and mechanical properties of the materials selected, ease of fabrication and production cost were carefully considered. Model for the equipment was developed using SolidWorks application software, which was followed by design analysis of its components. Simulation of the developed model was done using ANSYS, SolidWorks and Autodesk Inventor application software packages, in order to predict the performance of its components and to ascertain its functionality before fabrication. The simulation results showed that the design of the equipment is adequate and safe for fabrication. The equipment was then fabricated and assembled using appropriate manufacturing techniques. The total fabrication cost is put at One Thousand, Three Hundred and Thirty dollars (\$1,330) only. Its functional performance was evaluated; the throughput and thermal efficiencies obtained were 96.1% and 85.3% respectively. It can be said that the equipment has the capacity to serve its primary purpose as it was able to convey and cool the material poured into it from 82.2^oC to 29.2^oC.

© 2020 Jordan Journal of Mechanical and Industrial Engineering. All rights reserved

Keywords: Screw Conveyor Design, Plantain Flour Cooling, Simulation, Evaluation, Process Plant;

Nomenclature

\dot{m} Mass flow rate

Q_m Mass throughput

ρ_f Flour's bulk density,

w Width of conveyor

N Angular speed of conveyor

p Pitch of conveyor auger

f Feed rate

dH Change in internal (heat)energy

\dot{m}_a Mass flow rate of air

k Heat capacity of conveyor walls

A Surface area of conveyor walls

C_p Heat capacity of conveyor walls

T_a Ambient temperature

T_{ain} Inlet temperature of cooling air

T_{aout} Outlet temperature of cooling air

T_{fin} Inlet temperature of flour

T_{fout} Outlet temperature of the flour

S_p Screw pitch

D_{screw} Screw diameter

P_f Power required to overcome conveyor friction

P_{cm} Power required to transport the plantain flour

P_L Power required to lift the plantain flour

g Gravitational constant

L_{sc} Total length of the screw conveyor

F_b Hanger bearing factor

F_m Material factor

Q_e Equivalent capacity

η_{drive} Drive efficiency factor

1. Introduction

Material handling is a science involving the moving, packaging and storing of materials [1]. Material handling is very crucial to food processing, which can either be manual, mechanized or pneumatic. According to Evstratov *et al.* [2], materials' conveyance is usually achieved by a combination

* Corresponding author e-mail: mkadeyeri@futa.edu.ng.

of mechanical, inertial, pneumatic and gravity forces. Inclined simultaneous conveying and cooling of pulverized pulps in a plant that is meant for processing unripe plantain into flour require a material handling equipment that will be able to prevent air, dust and other foreign materials from interacting with the flour produced to avoid contamination and to ensure quality by making the equipment dust- and air-tight [3]. In view of this, Waje *et al.* [4], having established its advantages over other conveyors that are used as heat exchangers, the use of screw conveyor as heat exchanger is recommended whenever simultaneous conveying and cooling or heating are required during processing operations in addition to other factors. Because of its outstanding advantages over other conveyors, Kaplan and Celik [5, 6], Verchshagin *et al.* [7], Cucumo *et al.* [8] and Mustaffar *et al.* [9] also affirmed the use of screw conveyor as heat exchanger when faced with the challenge of simultaneous conveying and cooling or heating of materials during processing operations.

Screw conveyor is known to be cost-effective, easy to install, occupies less space, possesses excellent volumetric efficiency, requires low maintenance, gives good throughput control, provides environmentally clean solutions to process handling problems, and provides dust- and air-tight material handling [4, 10, 11]. It is interesting to know that belt, chain, bucket and pneumatic conveyors do not possess these aforementioned qualities to qualify them for use/consideration when pulverized materials are to be concurrently cooled and transported in an inclined position as in the case of a plant that processes unripe plantain into flour. Screw conveyor helps transport materials at controlled and steady rates, which makes it applicable for measuring materials' flow rates, which other conveyors (such as pneumatic, belt, chain and bucket conveyors) cannot do [2].

Screw conveyor can be designed to function as a dryer or heat exchanger by running hot or cold fluid through the jacket created around its trough. Screw conveyor is reported as one of the oldest, simplest, most efficient and economical methods of conveying materials from one location to another in processing operations [12]. Thus, screw conveyor is widely used in processing operations due to its inherent outstanding advantages over other conveyors [13]. Hence, a screw conveyor, with fully enclosed tubular type casing, was considered for this operation based on the recommendations of Waje *et al.* [6, 14] and because of its versatility and inherent ability to operate over a wide variety of speeds as well as angles of inclination up to vertical, which other conveyors cannot do [13, 15]. This will help the flour produced from the pulverizing unit retain its quality and moisture content since the screw conveyor is made dust- and air-tight to prevent interaction with the surrounding environment. It will also give room for controlled material flow/throughput into the packaging section of the plantain processing plant.

Plantain is from Musaceae plant family [3] and it is known to be cheap for the management of diabetes mellitus, a risk factor for COVID-19 [16, 17]. It is cultivated in humid tropical Africa, Asia, Latin America, Central and Southern America [18, 19]. It has also been reported that Nigeria is the largest producer of plantain in West Africa with huge percentage found in the Southern part of the country [20, 17]. Poor transportation and distribution facilities in the

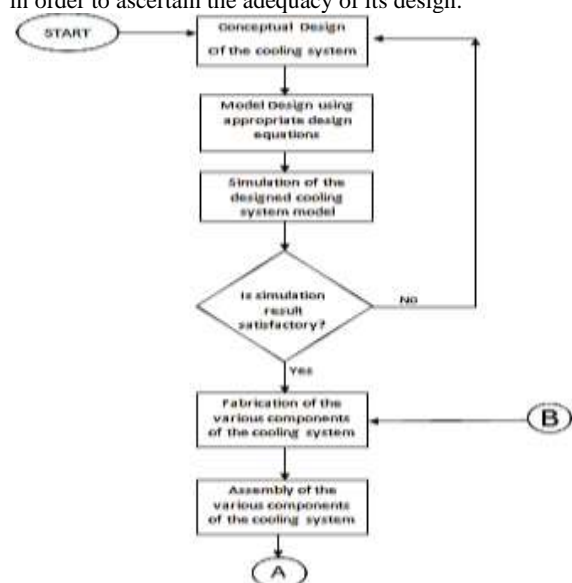
production areas, harvest at maturity close to fruit ripening, and poor storage conditions are factors likely to depreciate quality and provoke post-harvest losses of plantain. To minimize or eliminate these losses, to enhance and improve the value, plantain is usually processed into storable and value-added products [21, 17].

In a plantain processing plant, several materials are moved within the production floor, ranging from washed plantain pulps to dry pulverized plantain pulps. This research investigated the simultaneous transfer and cooling of flour from pulverizing unit to the packaging unit of a plant that processes unripe plantain into flour that is being developed in Mechanical Engineering Department of the Federal University of Technology, Akure, Ondo State, Nigeria. The packaging, however, must be done only after the plantain flour is cooled as stated by Olutomilola [3]. Cooling to storage temperature is necessary to prevent the flour produced from clumping after packaging due to temperature induced heating of its particles, which can adversely affect its quality, shelf life and esteem value. Cooling while conveying the flour, using enclosed screw conveyor, will bring reduction in production cost (in terms of processing time), improvement in hygiene, quality and esteem value of the product [22]. Hence, there exists a need to develop an adequate cooling system alongside the conveyance of plantain flour before packaging.

2. MATERIALS AND METHODS

2.1. Flowchart and Model Development for the Screw Conveyor

In actualizing the aim of this study, a flowchart, depicting the flow of activities involved in developing a screw conveyor for simultaneous conveyance and cooling of flour in a plantain processing plant, was developed as shown in Figure 1. Model for the screw conveyor was developed using solidworks computer aided design (CAD) application software (see Figures 2 to 5). Design calculation of all its component parts was done after they were identified. Before fabrication, a simulation study was also conducted on the model developed for the screw conveyor in order to ascertain the adequacy of its design.



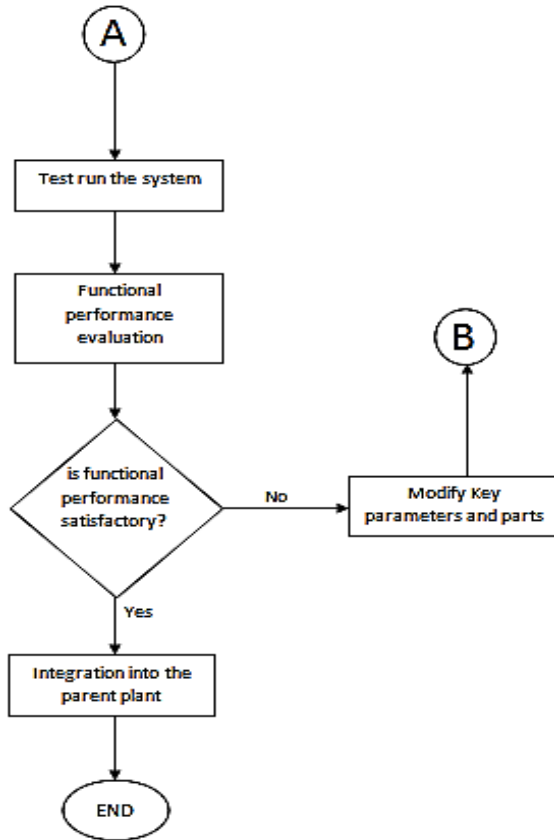


Figure 1. Process flow chart for the research methodology

2.2. Design Consideration

The materials and methods adopted in this research were appropriated in consideration of the following factors in order to produce an efficient and reliable equipment that will ensure techno-economic status of the intended users: availability of material, mechanical properties of the materials selected (such as rigidity, corrosion and wear resistance), hygiene, fabrication cost and overall weight of the machine.

2.3. Design Concept of the Screw Conveyor System

The screw conveyor, which is expected to convey 500 kg of plantain flour per hour, consists of a worm screw in a cylindrical housing with aluminum heat sink arranged around its periphery (Figures 2 to 4). Another tube (known as cooling chamber) houses the heat sink. The screw works by using the internal friction within the flour (bulk solid) to transfer forward motion to the flour in contact with the spiral and to the whole tube contents. With the inclination of the system, a dynamic equilibrium is set up with the spiral action moving some particles upward, the rate of volume transfer being proportional to the shaft's speed. When the screw moves, the hot flour from the hopper contacts the screw housing, through which heat is absorbed from it to the heat sink. The heat sink absorbs the heat and transfers it through convection currents to the cooling air medium. The blower (rating: 0.375 kW; 1400 rpm), which is attached close to the flour exit end of the conveyor, countercurrently blows cool atmospheric air into the cooling chamber against

the flour's direction of flow. Heat is removed from the heat-sink and released through an outlet that is attached to the cooling chamber near the conveyor's hopper. A speed reducing gear system helps to stepdown the motor's speed from 1400 rpm to the screw's speed (42 rpm). The motor (1hp) is connected to the reducing gear via shaft and pulley system, which are connected to the screw shaft through a belt drive system. The cooled flour pours out of the conveyor through a tubular outlet, near the motor. Figures 2 and 3 show the isometric and exploded views of the screw conveyor respectively. Its orthographic projection, showing the side, front and plan views in third angle projection, is presented in Figure 4. The sectional view of the screw conveyor was also generated through the mid-plane of the set up to facilitate access to the hidden components of the machine as shown in Figure 5. It is to be noted that: all the materials selected for the fabrication of the screw conveyor were sourced/obtained locally in/within Nigeria; all the components in contact with the flour (i.e. the screw, end plates, screw housing, hopper, flour inlet and outlet) were made of stainless steel in compliance with international food safety policies, while others were made of mild steel.

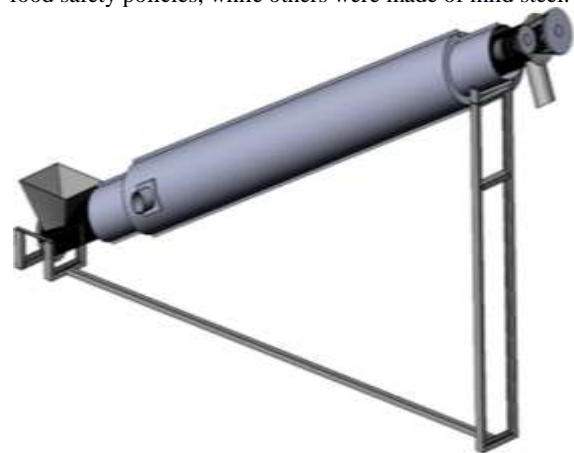


Figure 2. Isometric view of the screw conveyor

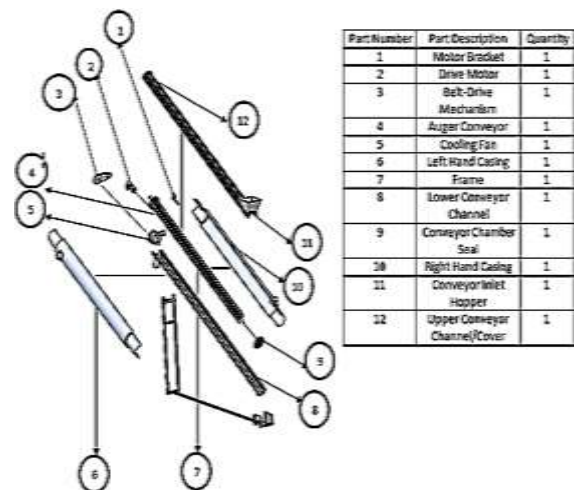


Figure 3. Exploded view of the screw conveyor



Figure 4. Orthographic view of the screw conveyor

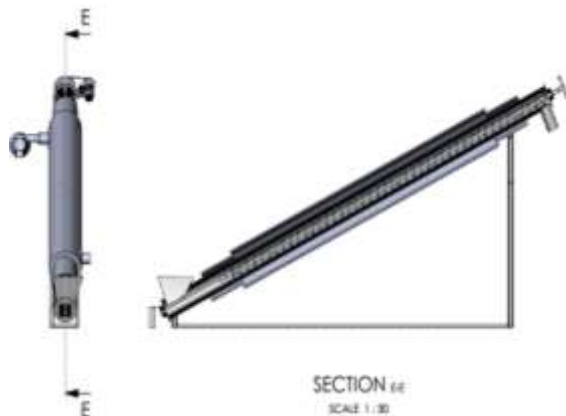


Figure 5. Sectional view of the screw conveyor

2.4. Design Calculation of the Screw Conveyor

2.4.1. Classification of the design model

Design calculation of the screw conveyor system began with classification of the design model, which involved the adoption of appropriate design method/approach to describe and evaluate problem domains under consideration. The design of the screw conveyor system has two major aspects, namely: material flow and material cooling. Material flow is primarily governed by the width (w) of the screw conveyor, rotational speed (N) of the conveyor shaft, pitch (p) of the screw and the flour feed rate (f). Modeling a dependence expression, with the mass flowrate (\dot{m}) of the flour as the dependent variable, gave rise to equation (1).

$$\dot{m} = \phi(w, N, p, f) \quad (1)$$

Material cooling is primarily determined by: mass flow rate of the cooling air (\dot{m}_a) circulated by the blower around the chamber, thermal conductivity (k) of the chamber material, surface area (A) and thickness (t) of the chamber, heat capacity (C_p) of the flour, ambient temperature (T_a), and rotational speed (N) of the screw shaft. Similarly, a dependence equation with the rate of heat removal (dH) as the dependent variable is given in equation (2).

$$dH = \phi(\dot{m}_a, k, A, t, C_p, T_a, N) \quad (2)$$

2.4.2. Frame of the screw conveyor system

The frame, which supports the screw conveyor assembly, must be rigid enough to withstand the weight of the whole assembly without buckling in order to prevent vibration or collapse of the equipment. The height of the frame is a function of the conveying height, which was obtained from the configuration and arrangement of the

machines in the process plant. In essence, it is necessary to determine the load that the frame can withstand without crippling or buckling. Mild steel angle bar having L-shaped cross-section (welded together at ends) was selected for the frame. There are different types of end connections used in holding frames together and the type of end connection used usually affects the performance of supporting frames. Hence, the frame members were welded together at the ends since fixed-type end connection was selected for the frame. The Euler's theory for crippling and buckling load ' W_{cr} ' under various end conditions is represented in equation (3) [23].

$$W_{cr} = \frac{[C \pi^2 E A]}{[L_{col}/k]^2} \quad (3)$$

$$k = \sqrt{\frac{I}{A}} \quad (4)$$

where: C is the constant representing the end conditions of the column or end fixity coefficient, which is 4 for welded and bolted joints; E is the modulus of elasticity for the column material; A is the cross-section area; L_{col} is the column's length (1500mm); k is the least radius of gyration of the cross section; and I is the polar moment of area.

Since the frame which supports the screw conveyor system is made from angle iron with L-shaped cross section, it is important to know that the value of the crippling load must be far greater than the total weight of the whole assembly supported by the frame. To achieve this, various dimensions of angle iron from manufacturers' specification were used until the desired crippling load was obtained [24]. A dimension that produced a crippling load far greater than the weight of the screw conveyor assembly was a 75 mm angle iron, whose dimensions are presented in Figure 6. The polar moment of area of the section is a factor that contributes to the strength of the column. This was obtained from equations (5) and (6) to be 635885.41 mm⁴. Since I_{YY} is equal to I_{XX} , the section will tend to buckle along Y-Y axis and X-X axis [24].

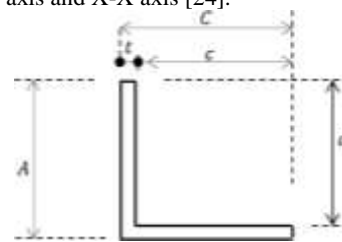


Figure 6. Cross section of the Frame

$$I_{XX} = \frac{1}{12}(AC^3 - ac^3) \quad (5)$$

$$I_{YY} = \frac{1}{12}(A^3C - ca^3) \quad (6)$$

Where: $A = 75$ mm; $C = 75$ mm; $a = 70$ mm; $t = 5$ mm; and $c = 70$ mm.

The area of the column A_c was obtained to be 725 mm² from equation (7). Hence, the least radius of gyration of the cross section (k) was obtained to be 877.08 mm using equation (4). According to Khurmi and Gupta [24], the young's modulus of elasticity for mild steel is 2.1×10^5 N/mm². Since the length of the column supporting the screw conveyor system is 1500mm, the buckling load on the column was obtained as 2.05 GN from equation (3). The angle of elevation of the system was obtained as 30° from equation (8) [25].

$$A_c = (a + C)t \tag{7}$$

$$\theta_{con} = \sin^{-1} \left[\frac{L_{col}}{L_{con}} \right] \tag{8}$$

Where: θ_{con} is the angle of elevation of the conveying medium; and L_{con} is the screw conveyor length, which is 3 m.

2.4.3. Determination of the screw conveyor's throughput and speed

The volumetric throughput (Q_v) and rotational speed of the screw conveyor (N_{sc}) were determined from equations (9) and (10) to be 2.495 m³/hr (or 88.111 ft³/hr) and 100rpm respectively [15, 12]. A trough loading and screw diameter of 30%A and 150 mm were respectively selected based on the material characteristics of plantain flour. Hence, the screw pitch was determined as 75 mm using equation (11).

$$Q_v = \frac{Q_m}{\rho_f} \tag{9}$$

$$N_{sc} = \frac{Q_v \times CF_0 \times CF_1 \times CF_2 \times CF_3}{C_{1rpm}} \tag{10}$$

$$S_p = 0.5 \times D_{screw} \tag{11}$$

Where: Q_m is the mass throughput, which is 500 kg/h; ρ_f is the flour's bulk density, which is 200 kg/m³ [26]; CF_0, CF_1, CF_2 and CF_3 are constants related to the conveyor configuration, which are 1.11, 2, 1 and 1 respectively; C_{1rpm} is the conveyor's capacity at 1 rpm, which is 2; S_p is the screw pitch and D_{screw} is the screw diameter.

2.4.4. Design of hopper for the screw conveyor

The function of the hopper in the conveying machine is to ensure that plantain flour enters the screw conveyor's trough at a consistent rate in order to prevent the whole flour from getting stuck at the entrance of the conveyor. Basically, conical and pyramidal shaped hoppers are common. The choice of selection depends on the nature of material to be conveyed and physical configuration of the machine. In practice, flour or powdery materials are suitable with pyramidal shaped hopper because it reduces material's flowrate into the conveyor by virtue of its sharp edge restrictions. Thus, a stainless steel square pyramidal shaped hopper was considered for the design. The volume of the hopper is a function of the total volume of plantain flour to be conveyed in the process plant, while its dimensions were obtained from the volume of plantain flour to be contained by it. The volume of the hopper was a section of a complete square pyramid cut away at some point along its vertical height as shown in Figures 7 and 8. Hence, the volume of the hopper was obtained as 90863000 mm³ using equation (13).

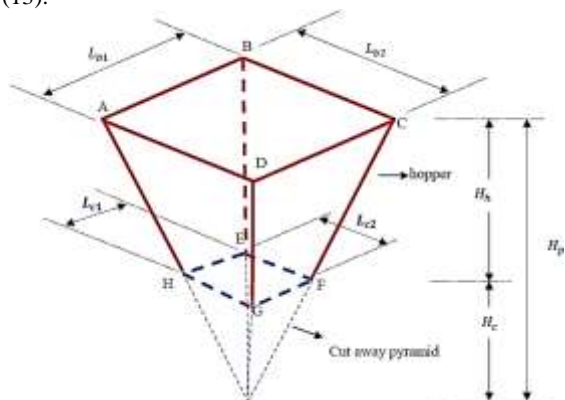


Figure 7. Schematic diagram of the hopper

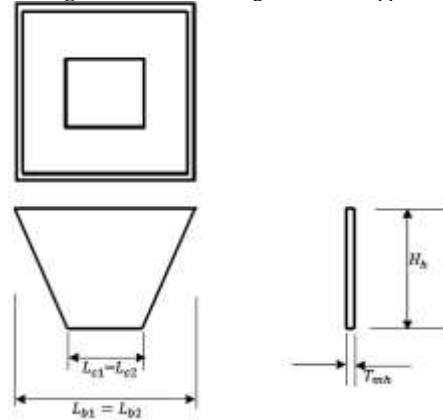


Figure 8. Orthographic projection of the hopper

According to Olowofeso *et al.* [25], the volume of a pyramid with square base is given as

$$V_{pd} = \frac{\text{area of base} \times \text{height of the pyramid}}{2} \tag{12}$$

$$V_{hp} = V_{wpd} - V_{capd} = \left\{ \frac{1}{2} \times L_{b1} \times L_{b2} \times H_p \right\} - \left\{ \frac{1}{2} \times L_{c1} \times L_{c2} \times H_c \right\} \tag{13}$$

Note that $L_{b1} = L_{b2}$ and $L_{c1} = L_{c2}$ for a square pyramid.

Moreover, the weight of the hopper was obtained as 102.11 N from equation (14).

$$W_{hopper} = \rho_{hm} \times V_{hm} \times g = \rho_{hm} \times (2H_h T_{mh} [L_{b1} + L_{c1}]) \times g \tag{14}$$

Where: V_{pd} is the volume of a pyramid; V_{hp} is the hopper's volume; V_{wpd} is the volume of the whole pyramid's; V_{capd} is the volume of cutaway pyramid; L_b is the length of the top shape of the hopper, which is 470 mm; L_c is the length of the base of the hopper, which is 240 mm; H_p is the vertical height of the pyramid, which is 940 mm; H_c is the vertical height of the cut away pyramid, which is 450 mm; H_h is the vertical height of the hopper, which is 490 mm; W_{hopper} is the weight of the hopper when empty; ρ_{hm} is the density of the material from which the hopper was made, which is 7480 kg/m³ [24]; V_{hm} is the Volume of the material from which the hopper was made; and T_{mh} is the thickness of the stainless steel sheet (2 mm).

2.4.5. Power requirement for the conveying and cooling system

The power required by the screw conveyor was computed using equations (15) to (19) [12, 3, 27]. Hence, 1 horsepower or 0.746 kW motor was selected to drive the screw conveyor and its components as recommended by CEMC [12] and Daniyan [28].

$$P_{ST} = P_f + P_{cm} + P_L \approx 0.023 \text{ kW} \tag{15}$$

$$P_f = \frac{g \times L_{sc} \times F_b \times N_{sc}}{30300} \approx 0.016 \text{ kW} \tag{16}$$

$$P_{cm} = \frac{g \times L_{sc} \times Q_e \times F_m}{30300} \approx 0.004 \text{ kW} \tag{17}$$

$$P_L = \frac{g \times Q_e \times h}{1000} \approx 0.003 \text{ kW} \tag{18}$$

The required motor power P_{motor} was calculated to be 0.031 kW using equation (19).

$$P_{motor} = \frac{P_{ST}}{\eta_{drive}} \tag{19}$$

$$\therefore R_{AH} + R_{BH} = -472N \quad (27)$$

Taking moment about R_{BH} gives

$$\sum MR_{BH} = 0; \quad \therefore R_{AH} = 974 N$$

From equation (27), R_{BH} was obtained as -1446 N. The maximum resultant bending moment M_b obtained from equation (24) is 1958 Nm, as shown in Figure 12. According to equation (20), CEMC [12], Khurmi and Gupta [24], a shaft diameter of 40 mm was selected for the drive and tail shafts of the screw conveyor.

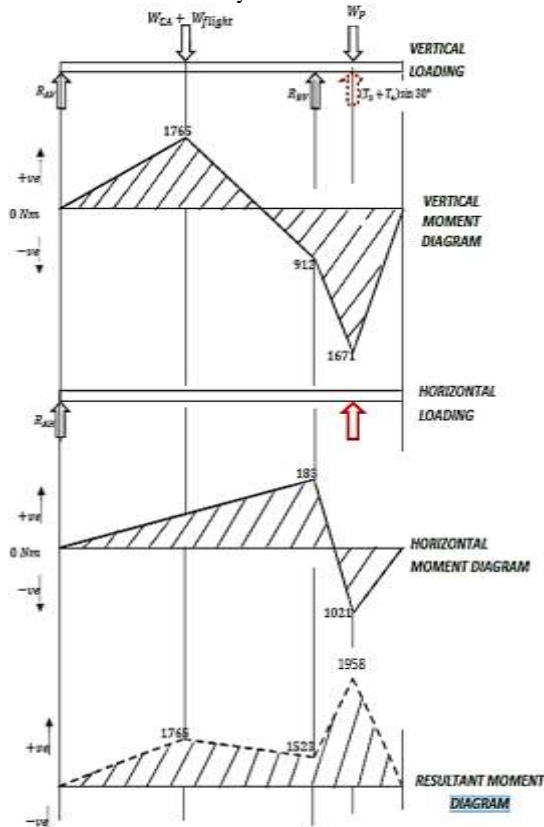


Figure 12. Bending moment diagram for the conveyor

2.4.7. Cooling system and screw housing

The function of cooling in the plantain flour processing plant is to ensure that the flour is maintained at a temperature that will prevent it from clumping and loss of nutritional qualities due to temperature induced reactions after packaging. There are several methods in existence for cooling food materials, but the choice of a method depends on the nature of substance to be cooled and the intended temperature difference that is to be achieved. In this study, since the material to be cooled is powdery in nature, it is then required that it must be enclosed while cooling it to prevent spillage or loss of the product. Furthermore, in order to reduce the processing time, the cooling process has been designed to be done alongside the conveying process. In view of this, the conveying length was carefully selected so that the cooling would have been achieved before the product exits the screw conveyor. The need to enclose the product in the screw housing during conveyance prompted the use of a double pipe type of heat removal process. A counter-flow arrangement was chosen because of its efficiency in terms of large temperature difference compared to parallel- and cross-flow arrangements [29, 30,

31]. Hence, Figure 13 shows a cross section of the cooling and conveying system assembly, from which the mass flow rate of air entering the system, heat removed from the flour, outlet temperature of air exiting the system and the overall heat transfer coefficient were determined.

From Figure 13, T_{ain} is the inlet temperature of cooling air (28°C); T_{aout} is the outlet temperature of cooling air; T_{fin} is the inlet temperature of flour (65°C); T_{fout} is the outlet temperature of the flour, which is desired to have a value closer to the value of the ambient temperature (27°C) [3]; L_{CM} is the length of the cooling Chamber, which is 3500mm; L_{PS} is the length of the flour conveying medium (3250mm); D_{PS} is the diameter of the flour conveying medium (156 mm); and D_{CM} is the diameter of the cooling chamber (320mm). Since the process plant is set to an output of 500 kg/hr, it can be stated that the mass flow rate (\dot{M}_f) of plantain flour in the plant is 0.139kg/s. Moreover, Figure 14 depicts the temperature exchange in a counter flow heat exchanging system.

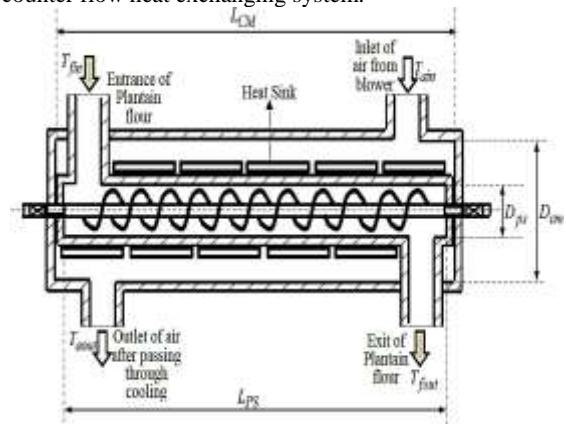


Figure 13. Schematic Diagram of the screw conveyor

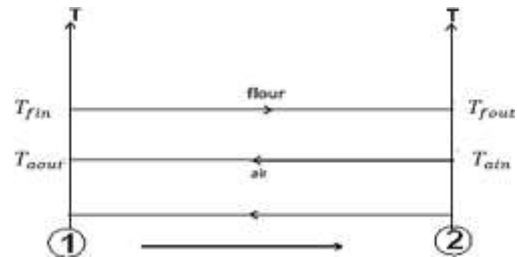


Figure 14. Cooling diagram of the conveyor set up

The heat removed from the flour (Q_f) was obtained from equation (28) as 8.895 kJ. The temperature of the air exiting the system (T_{aout}) was obtained from equation (29) as 40.67°C, while the mass flow rate of air (\dot{M}_{air}) entering the system was obtained from equation (31) as 0.699 kg/s by assuming that the heat lost by the flour is equal to the heat gained by the cooling air.

$$Q_f = \dot{M}_f C_{pf} (T_{fin} - T_{fout}) \quad (28)$$

$$Q_f = h_{air} A_{ch} \Delta T_a = h_{air} \times A_{ch} (T_{ain} - T_{aout}) \quad (29)$$

$$A_{ch} = \pi D_{CM} L_{CM} \quad (30)$$

$$\dot{M}_{air} = \frac{Q_f}{C_{air} (T_{ain} - T_{aout})} \quad (31)$$

Where: C_{pf} is the Specific heat capacity of plantain (*Agbagba Species*), which is 1.684 kJ/kg K [26]; h_{air} is the

convective heat transfer coefficient of air ($200 \text{ W/m}^2\text{K}$); A_{ch} is the surface area over which cooling air travels, which was obtained as 3.51 m^2 using equation (30); and C_{air} is the specific heat capacity of air at constant pressure (1.005 kJ/kg K).

3. 3. RESULTS AND DISCUSSION

3.1. Simulation of the Screw Conveyor System

The screw conveyor was simulated, using ANSYS, SolidWorks and Autodesk Inventor application software packages in order to predict the performance of its designed components and to ascertain its functionality in the process plant before fabrication [32, 33, 34].

3.1.1. Simulation of the screw conveyor's frame

The primary stresses induced in the frame are normal and axial stresses as shown in Figures 15 and 16. The maximum normal stress induced is 17.44 MPa , a value below the yield stress of mild steel which is about 250 MPa [24]. This leaves ample room for optimizing the design with enough factor of safety (FOS) to spare. Most of the points where this stress is induced are located around the base of the frame and this may be attributed to the interaction of reaction forces and the concentration of body forces. In the case of the axial stress shown in Figure 16, the maximum value is 0.036 MPa . This is obviously below the breaking limit, which tends to occur in long members of the frame assembly. This happens because the axial load is compressive in nature and the greater the length, the greater the chances of having compression occur due to buckling.

Another primary parameter that ascertains the viability of the design is the displacement as shown in Figure 17. The displacement is the geometric deformation of members in the frame assembly. This is an important consideration because of the space constraints imposed by the plant arrangement and operator safety. A maximum displacement of 3.649 mm is seen in Figure 17 and it occurs along the midpoint of the member at center, which also happens to be the longest. This agrees with the principles of structural mechanics where the maximum deflection is at the midpoint of the primary loaded member.

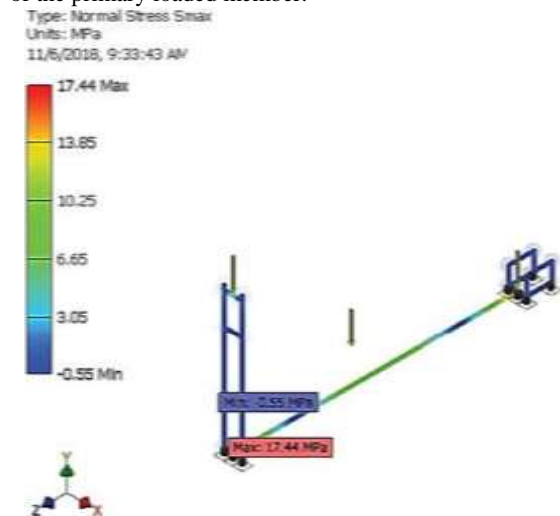


Figure 15. Normal Stress induced in the Frame.

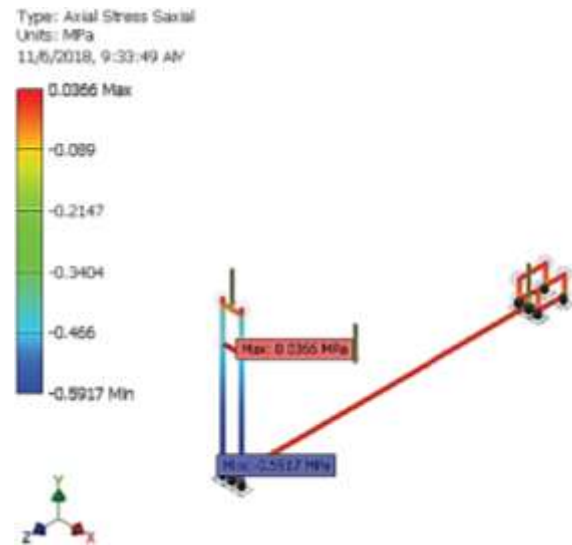


Figure 16. Axial Stress induced in the frame

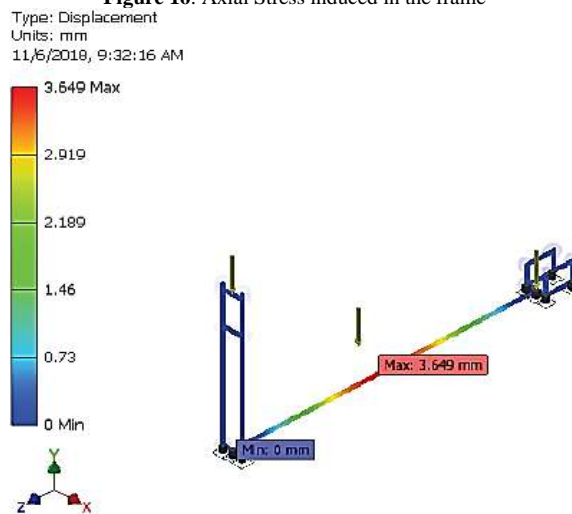


Figure 17. Displacement of frame members

3.1.2. Simulation of the screw conveyor's shaft

It is seen from Figure 18 that stresses are concentrated at the bearing surfaces of the two edges of the conveyor due to the high torsional forces induced at rotation. There is a similar situation at the root of the screw surface which can be attributed to centrifugal effect and reaction forces as they convey the flour along the conveyor's trough. From displacement diagram shown in Figure 19, the displacement is maximum at the very tips of the conveying screw surface. Two things can be said to be responsible for this condition; one is the reverse effect of centrifugal forces with the flour making maximum contact at the tips of the screw. This is as a result of the fact that the screw is partially immersed in the flour (fill ratio, $\lambda = 0.45$ or 45% of the outer edge of the surface). For this same reason, the displacement is minimum at the root of the screw shaft. Figure 20 shows the equivalent strain induced in the screw shaft. This is seen to be concentrated at the ends of the shaft, which may be, mostly, due to the bearing loads. Hence, Table 1 presents the maximum values of the stress, displacement and strain obtained from the simulation.

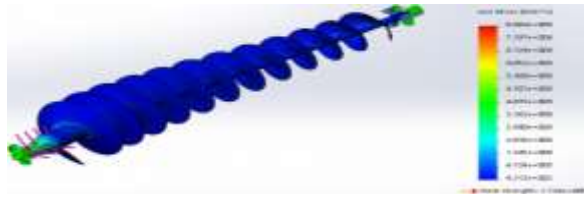


Figure 18. Von Mises stress induced in the shaft under applied loads

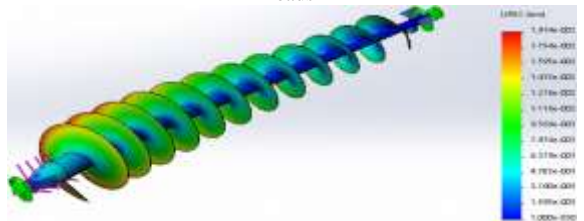


Figure 19. Displacement of the various nodes of the shaft under applied loads

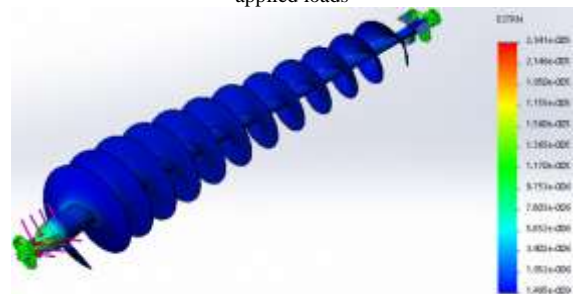


Figure 20. Equivalent Strain of the shaft under loads

Table 1. Comparison and validation of static stress values for screw shaft

Parameter	Maximum Simulated Value	Safety Limit	Remark
Von Mises Stress	8.069 MPa	172.4 MPa	Safe
Displacement	1.914×10^{-2} mm	Not Applicable	-
Equivalent Strain	2.341×10^{-5}	Not Applicable	Safe

3.1.3. Simulation of the screw conveyor system

Figures 21 to 23 show the results of the heat transferred across the two domains of the simplified model of the heat

exchanging system as executed in ANSYS. The boundary conditions were set at air mass flow rate of 0.139 kg/s at temperature of 65°C for the main inlet, and set at mass flow rate of 0.699 kg/s at 27°C at the small outlet of the top all at atmospheric air pressure of 101325 N/m².

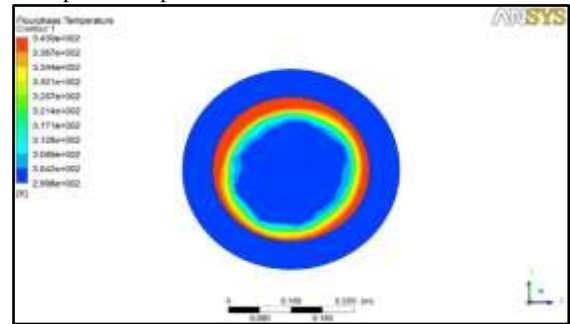


Figure 22. Temperature contour in the radial direction at air and flour inlets

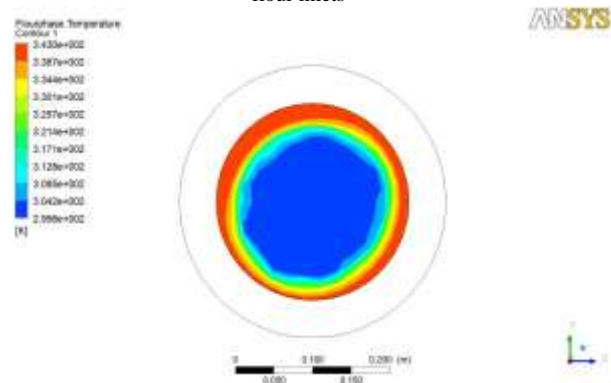


Figure 23. Contour showing flour outlet temperature distribution in the radial direction

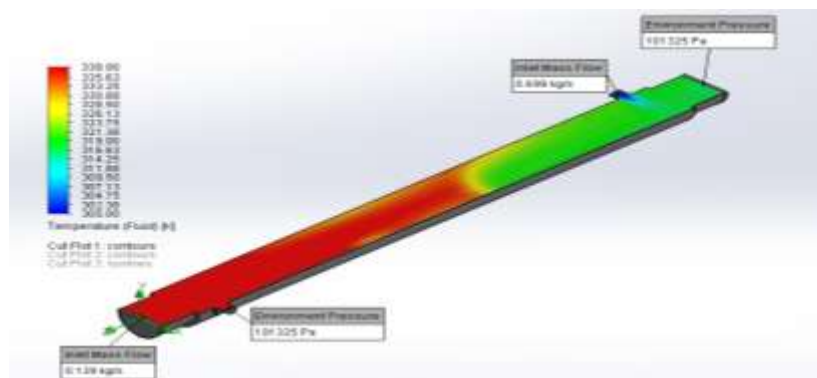


Figure 21. Computed temperatures from simulation

3.1.4. Functional test of the fabricated screw conveyor

The functional performance of the fabricated screw conveyor system was evaluated: to ensure that it serves its intended purpose when incorporated into the plantain

process plant, and to ensure that the values arrived at fall within the projected limits, as obtained from its design analysis. 4.5 kg of the food material to be cooled was then used for the test. The evaluation parameters imputed,

instruments used in achieving this purpose and the results obtained, with the conditions under which the test was done are as presented in Table 2. A significant cooling effect, a throughput of 2.4 kg/min or 144 kg/h, a travel time of 2.43 minutes and an efficiency (based on the ratio of the output to the input) of 96.1% were obtained. The outlet temperature of the cooled material as measured at the conveyor outlet was found to be 29.2°C (compared to 27°C obtained from the design analysis). It is believed that the outlet temperature of any food material under consideration can be influenced by influencing inlet temperature of the cooling air. It can be inferred that the lower the temperature of incoming cooling air, the lower would be the temperature of exiting cooled material. This can be expressed by equation (32), which is a linear relationship.

$$T_{ain} \propto T_{fout} \quad (32)$$

The heat removed from the food material (Q_{hrff}) was calculated to be 2.4 kW using equation (33) in conjunction with equations (34) and (35). In order to determine the efficiency of the machine, the analysis results were compared with the actual evaluation results. The cooling factor percentage was then obtained to be 64.48% from equation (36).

$$Q_{hrff} = \dot{m}C_{pf}\Delta T \quad (33)$$

$$\dot{m} = \frac{\text{Weight of flour}}{\text{Time of travel}} = 0.0276 \text{ Kg/s} \quad (34)$$

$$\Delta T = T_{fin} - T_{fout} = 53^\circ\text{C} \quad (35)$$

$$\text{Cooling Factor Percentage} = \frac{T_{fin} - T_{fout}}{T_{fin}} \times 100\% \quad (36)$$

According to Olanrewaju *et al.* [11], the throughput efficiency of the screw conveyor system was calculated using equation (36) as 96.1%, while its thermal efficiency was calculated as 85.3% using equation (37). Hence, it can be inferred (based on the results obtained from its simulation and functional performance) that the screw conveyor system is capable serving its intended primary functions, which are to convey and cool flour in a plant for processing unripe plantain into packaged flour.

$$\text{Throughput Efficiency} = \frac{\text{Output weight of cooled flour}}{\text{Input Weight of hot flour}} \times 100 \quad (36)$$

$$\eta_{thsc} = \frac{\text{measure temperature of cooled flour}}{\text{Cal. temp. air emerging from chamber}} \quad (37)$$

Where: \dot{m} is the mass flow rate of the flour; C_{pf} is the specific heat capacity of plantain flour (1.684 kJ/kgK); ΔT is the difference between the inlet and outlet temperatures of the flour; and η_{thsc} is the thermal efficiency of the screw conveyor system.

Table 2. Input parameters and their measurement

Parameter	Initial Value	Final Value
Ambient temperature	28.1 °C	28.1 °C
Outlet Air Velocity	8.2 m/s	8.2 m/s
Weight of Flour	4.5 Kg	4.33 Kg
Time of travel		163 sec
Inlet temperature of flour	82.2 °C	29.2 °C
Relative Humidity	68.1%	
Moisture content of flour		≤10%
Throughput		144 kg/h
Average Time of Travel of Flour Through the Screw.	-	2.33 min

4. Conclusions

The performance, reliability and service life of any equipment or machine depends, to a large extent, on the care taken in assembling, installing and preparing it for its intended use [12]. While other researchers considered the screw conveyor as a heat exchanger for horizontal applications, in this study, an inclined screw conveyor heat exchanger, that is capable of simultaneously conveying and cooling flour from the pulverizing unit to the packaging unit of a plant that processes unripe plantain into flour has been developed. This study has been able to establish the advantages and use of screw conveyor as a heat exchanger, over other conveyors, when faced with the challenge of inclined simultaneous conveying and cooling/heating of materials during processing. The development was achieved through the application of suitable design analysis principles and manufacturing techniques.

A throughput of 144 kg/h and an efficiency of 96.1% were respectively recorded during its preliminary test. It was observed that the throughput was low because there was no continuous supply of material while conducting the test. A throughput that is as high as the designed throughput can be obtained if material is continuously fed into the screw conveyor. Being an ongoing research, a comprehensive/detail performance evaluation of the conveyor is under consideration, during which it will be evaluated with different food materials in order to establish its capability of handling any pulverized farm produce. Some factors or parameters would also be varied during the evaluation, and their effect(s) would be investigated, documented and reported.

Moreover, it was observed that the material's inlet temperature was 82.2°C while its outlet temperature was 29.2°C. It can be inferred from this observation that the temperature of incoming cooling air is directly proportional to the temperature of outgoing flour or food material under consideration. The quantity of heat thus removed was observed to be 2.4 kW, while the total cost of fabricating the screw conveyor is put at One Thousand Three Hundred and Thirty dollar (\$1,330). The components of the costing include; bought out parts at \$617; cost of fabricated parts was estimated at \$340; and cost of labour plus other variables were computed at \$373. This research has been able to establish a basis for the expansion of economic potential associated with the processing of plantain and a

pioneering effort in developing more efficient systems for simultaneous conveying and cooling of plantain flour and other similar food materials. It is hoped that this research will be found effective for process theory development or industrial applications.

Future work on this study will be to look at the adaptability and reconfigurability of the design for other agrarian allied flour processing plant.

5. Acknowledgements

The support of TETFund Nigeria, under research grant Ref: VCPU/TETFund/155, is gratefully acknowledged. Advance Manufacturing and Applied Ergonomics Research Group (AMAERG) is also appreciated for its contribution in terms of critical evaluation of the work.

References

- [1] B.G. Gautam, S.P. Ashok, S.K. Vaishali, H.K. Vinayak, "Productivity Improvement in Automated Material Handling System of Liquor Manufacturing Plant." *International Journal of Engineering Research and Applications* 2013; 3 (2013), No 4, 2530-2537.
- [2] V.A. Evstratov, A.V. Rud, K.Y. Belousov, "Process Modelling Vertical Screw Transport of Bulk Material Flow". *International Conference on Industrial Engineering, Procedia Engineering* 129 (2015), 397 – 402.
- [3] E.O. Olutomilola, "Development of a Process Plant for Plantain Flour Production". A PhD Thesis in Mechanical Engineering Department, School of Engineering and Engineering Technology, Federal University of Technology, Akure, Ondo State, Nigeria, 2019.
- [4] S.S. Waje, B.N. Thorat, A.S. Mujimdar, "An Experimental Study of the Thermal Performance of a Screw Conveyor Dryer." *Drying Technology* 24 (2006), 293-301.
- [5] O. Kaplan, C. Celik, "Woodchip Drying in a Screw Conveyor Dryer". *Journal of Renewable and Sustainable Energy* 2012; 4, 063110.
- [6] O. Kaplan, C. Celik, "An Experimental Research on Woodchip Drying Using a Screw Conveyor Dryer" *Fuel, Elsevier Ltd*; 215 (2018), 468-473.
- [7] Verchshagin O., Yesseyeva G., Mukasheva T., Saduakassova G., Gassanov K., Kushnir V., Shkotova T. Methodology to Calculate Design Parameters of Screw Heat Exchanger for Vat Pasteurizer. *Journal of Engineering and Applied Sciences* 2016; 11(S1): 2955-2961.
- [8] Cucumo Thermodynamic Analysis of a Prototype Indirect Screw Drier for Aggregates and Recycled Mineral Aggregates. *International Journal of Heat and Technology* 2017; 35(S1): S427-S434.
- [9] Mustaffar, A. Phan, K. Boodhoo., "Hybrid Heat Pipe Screw Dryer: A Novel, Continuous and Highly Energy-Efficient Drying Technology". *Chemical Engineering & Processing: Process Intensification*, Vol 128 (2018), 199-215.
- [10] S.S. Waje, A.K. Patel, B.N. Thorat, A.S. Mujimdar, "Study of Residence Time Distribution in a Pilot-Scale Screw Conveyor Dryer." *Drying Technology*, Vol 25 (2007), 249-259.
- [11] T.O. Olanrewaju, I.M. Jeremiah, P.E. Onyeonula, "Design and Fabrication of a Screw Conveyor." *Agricultural Engineering International: CIGR Journal*, Vol 19 (2007) No. 3, 156-162.
- [12] CEMC. "Screw Conveyor Components and Design", Version 2.20. *Screw Conveyor Manual, Conveyor Engineering and Manufacturing Co.* 2012; 1-105. www.conveyoreng.com
- [13] G.J. Raymus, "Handling of Bulk Solids and Packaging of Solids and Liquids in Perry R.H., Green D.W., Maloney J.O. editors. *Perry's Chemical Engineers' Handbook*, 8th ed. McGraw-Hill Company, USA, 1997; 21-3 – 21-22.
- [14] S.S. Waje, B.N. Thorat, A.S. Mujimdar, "Screw conveyor dryer: Process and Equipment Design". *Drying Technology*, Vol. 24 (2007), 241–247.
- [15] A.W. Roberts, "Design Considerations and Performance Evaluation of Screw Conveyors". Centre for Bulk Solids and Particulate Technologies, the University of Newcastle, Australia 2013. <https://pdfs.semanticscholar.org/f26d/1c1dd211079ac5d2d7e7fc0cd6958865444f.pdf>
- [16] E.O. Olutomilola., S.P. Ayodeji., M. K. Adeyeri, "Finite Element Analysis of a Washing and Preheating Unit Designed for Plantain Flour Process Plant". *International Journal of Engineering Technologies*, 5 (2019) No 4, 117-127.
- [17] E.O. Olutomilola, S.P. Ayodeji, M. K. Adeyeri, "Design and Structural Analysis of a Particulating Machine for Plantain Flour Process Plant." *ARPN Journal of Engineering and Applied Sciences*, 15 (2020), No. 17, 1816-1824.
- [18] A.B. Ayanwale, A.O. Fatunbi., M. Ojo, "Innovation Opportunities in Plantain Production in Nigeria". *Forum for Agric. research* 2016; 1-44.
- [19] E.O. Olutomilola., A. Omoaka, "Theoretical Design of a Plantain Peeling Machine." *FUTA Journal of Engineering and Engineering Technology*, 12 (2018), No. 2: 229-237.
- [20] A.O. Akinsanmi, G Oboh, J.A. Akinyemi., A.A.S. Adefeghe, "Assessment of the National Anti-Nutritional and Anti-Oxidant capacity of unripe, ripe and over ripe Plantain (*Musa Paradisiaca*) Peels. *International Journal of Advanced Research*; Vol 3 (2015) No. 2, 63 – 72.
- [21] A.O. Solanke, A.O. Falade, "A Review of the Uses and Methods of processing Banana and Plantain (*Musa spp.*) into Storable Food Product." *Journal of Agricultural Research and Development, Faculty of Agriculture, University of Ilorin, Nigeria*, 9 (201), No. 2, 85-166.
- [22] S.P. Ayodeji, "Conceptual Design of a Process Plant for the Production of Plantain Flour". *Cogent Engineering Journal of Production and Manufacturing*, 3 (2016), 1-16.
- [23] H.B. Thomas. *Heat Transfer; Marks' Calculation for Machine Design*; McGraw Hill Company Inc.; 2005. DOI: 10.1036/0071466916 ISBN 0-07-146691-6
- [24] R.S. Khurmi, J.K. Gupta, 2009. *A Textbook of Machine Design*. 14th ed. India, New Delhi: Eurasia Publishing House (PVT.) Ltd.; 2009; 520-545, 608-612, 735-748, 763-770, 828-840, 965-967, 1088-1097.
- [25] O.E. Olowofeso, F.I. Alao, O. Olotu, S.T. Oni, D.O. Awoyemi, R.A. Ademiluyi, S.J. Kayode, O Olabode., T.T. Yussuf, T.O. Awodola, J.A. Dada, "Introductory Mathematics for Pre-Degree Science and University Diploma Science" The Federal University of Technology, Akure, Ondo State, 2006; 320-322.
- [26] D.B. Kiin-Kabari., V. Njoku. "The Particle Size and Thermal Properties of Flour from three Plantain (*Musa Paradisiaca*) Cultivars Grown in Nigeria". *Journal of Food Technology Research* 3(2016), No 1, 23-27.
- [27] Agriculture Canada. *Handling agricultural materials: Screw and Bucket Conveyors*, Digitized ed. Canadian Government Publishing Centre, Minister of Supply and Services, Ottawa, Canada 2012; Pp. 7-34.
- [28] I.A. Daniyan, A.O. Adeodu., O.M. Dada, "Design of a Material Handling Equipment: Belt Conveyor System for Crushed Limestone Using 3 roll Idlers". *Journal of Advancement in Engineering and Technology* 1(1), 2014, 1-7.
- [29] R.K. Rajput, *Heat and Mass Transfer*. Sixth Revised Edition. S. Chand and Company Pvt. Ltd., Ram Nagar, New Delhi, India, 2015; 574-666.
- [30] B.S. Malga, N. Kishan, V.V Reddy, K. Govardhan, "Finite Element Analysis of Fully Developed Free Convection Flow Heat and Mass Transfer of a MHD / Micropolar Fluid over a

- Vertical Channel". Jordan Journal of Mechanical and Industrial Engineering, Vol 8(2014), No 4, 219-232.
- [31] Alshare, W. Al-Kouz, S. Kiwan, A. Al-khalidi, M. Hader, "Computational modeling of gaseous flow and heat transfer in a wavy microchannel". Jordan Journal of Mechanical and Industrial Engineering, Vol 10 (2016) No 1, 75-83.
- [32] SolidWorks © 2016 X 64 software
- [33] ANSYS Fluent 14 Engineering software © ANSYS, Inc.
- [34] AutoDesk inventor software ©



الجامعة الهاشمية



المملكة الأردنية الهاشمية

المجلة الأردنية
للمهندسة الميكانيكية والصناعية

JJIMIE

مجلة علمية عالمية محكمة
تصدر بدعم من صندوق البحث العلمي

<http://jjmie.hu.edu.jo/>

ISSN 1995-6665

المجلة الأردنية للهندسة الميكانيكية والصناعية

المجلة الأردنية للهندسة الميكانيكية والصناعية: مجلة علمية عالمية محكمة تصدر عن الجامعة الهاشمية بالتعاون مع صندوق دعم البحث العلمي والابتكار - وزارة التعليم العالي والبحث العلمي في الأردن.

هيئة التحرير

رئيس التحرير

الأستاذ الدكتور محمد سامي الأشهب

مساعد رئيس التحرير

الدكتور احمد المقدادي

الدكتور مهند جريسات

الأعضاء

الأستاذ الدكتور طارق العزب

جامعة البلقاء التطبيقية

الاستاذ الدكتور محمد الوديان

جامعة العلوم والتكنولوجيا الاردنية

الاستاذ الدكتور جمال جابر

جامعة البلقاء التطبيقية

الاستاذ الدكتور محمد تيسير هياجنه

جامعة العلوم والتكنولوجيا الاردنية

الأستاذ الدكتور محمد الطاهات

الجامعة الاردنية

الاستاذ الدكتور علي جوارنه

الجامعة الهاشمية

فريق الدعم

المحرر اللغوي

الدكتور بكر محمد بني خير

تنفيذ وإخراج

م . علي أبو سليمة

ترسل البحوث إلى العنوان التالي

رئيس تحرير المجلة الأردنية للهندسة الميكانيكية والصناعية

الجامعة الهاشمية

كلية الهندسة

قسم الهندسة الميكانيكية

الزرقاء - الأردن

هاتف : 00962 5 3903333 فرعي 4147

Email: jjmie@hu.edu.jo

Website: www.jjmie.hu.edu.jo